NASA-CR-163431

NASA-CR-163431
19800021818

The Telecommunications and Data Acquisition Progress Report 42-58

May and June 1980

August 15, 1980

The Telecommunications and Data Acquisition Progress Report 42-58

May and June 1980

August 15, 1980

N80-30319#

Preface

This publication was formerly entitled *The Deep Space Network Progress Report*. Although the practice of reporting progress in the development and operations of the Deep Space Network continues, the report is expanded with this issue to include developments in Earth-based radio technology as applied to other research programs. These programs are:

(1) Geodynamics: For several years, the laboratory has been developing radio interferometry at microwave frequencies for application to geodetic measurements. This branch of telecommunications technology is now being applied to the study of geodynamics.

(2) Astrophysics: The deep space stations, individually and in pairs as an interferometer, have been used by radio astronomers for astrophysics research by direct observations of radio sources.

(3) An activity closely related to radio astronomy's use of the deep space stations is NASA's continuing program of radio search for extraterrestrial intelligence in the microwave region of the electromagnetic spectrum.

Each succeeding issue of this report will present material in some, but not all, of the following categories:

Radio Astronomy
Search for Extraterrestrial Intelligence
Radio Interferometry at Microwave Frequencies

    Geodetic Techniques Development
    Spacecraft Navigation
    Orbiting Very Long Baseline Interferometry

Deep Space Network

    Description
    Program Planning
    Planetary and Interplanetary Mission Support
    Advanced Systems
    Network and Facility Engineering and Implementation
    Operations
    Spacecraft Radio Science
    Planetary Radar
    Energy

In each issue, there will be a report on the current configuration of one of the seven DSN systems (Tracking, Telemetry, Command, Monitor and Control, Test Support, Radio Science, and Very Long Baseline Interferometry).

The work described in this report series is either performed or managed by the Telecommunications and Data Acquisition organization of JPL.

This Page Intentionally Left Blank

Contents

RADIO ASTRONOMY

RADIO INTERFEROMETRY AT MICROWAVE FREQUENCIES
GEODETIC TECHNIQUES DEVELOPMENT
ORION

SPACECRAFT NAVIGATION
Block I VLBI

THE DEEP SPACE NETWORK
DESCRIPTION OF THE DSN

PLANETARY AND INTERPLANETARY MISSION SUPPORT
Planetary Flight Projects

Interplanetary Flight Projects

ADVANCED SYSTEMS
Tracking and Ground-Based Navigation

Communications

Station Control and System Technology

Network Data Processing and Productivity

NETWORK AND FACILITY ENGINEERING AND IMPLEMENTATION
Network

Ground Communications

OPERATIONS
Deep Space Stations

SPACECRAFT RADIO SCIENCE

Accurate Radio Positions with the Tidbinbilla Interferometer

M. J. Batty, D. L. Jauncey, and P. T. Rayner
Division of Radiophysics, CSIRO, Sydney, Australia

S. Gulkis
Planetary Atmospheres Section

Originally published in the Proceedings of the Astronomical Society of Australia, *this article discusses the Tidbinbilla interferometer which is designed specifically to provide accurate radio position measurements of compact radio sources in the southern hemisphere with high sensitivity using the 26-m and 64-m antennas of the Deep Space Network at Tidbinbilla, near Canberra. The instrument also provides high-accuracy flux density measurements for compact radio sources.*

Radio position measurements with an error of $< 2''$ arc rms allow reliable optical identifications of compact radio sources to be made solely on the basis of radio-optical position coincidence. In this way neutral or red stellar objects, faint compact galaxies and faint QSOs can be reliably identified. Such identifications are of particular interest because they are rich in BL Lac objects, high-redshift QSOs, QSOs with unusual optical emission or absorption spectra and galaxies with active nuclei (Ref. 1).

The Tidbinbilla interferometer (Ref. 2) is designed specifically to provide accurate radio position measurements of compact radio sources in the southern hemisphere with high sensitivity. The interferometer uses the 26-m and 64-m antennas of the Deep Space Network at Tidbinbilla, near Canberra. The two antennas are separated by 200 m on a north-south baseline. By utilizing the existing antennas and the low-noise travelling-wave masers at 2.29 GHz, it has been possible to produce a high-sensitivity instrument with a minimum of capital expenditure. The north-south baseline ensures that a good range of u-v coverage is obtained, so that sources lying in the declination range $-80° \lesssim \delta \lesssim + 30°$ may be observed with nearly orthogonal projected baselines of $\gtrsim 1000 \, \lambda$.

For observations of catalogued sources an observing procedure similar to that developed for the RRE Malvern interferometer (Ref. 3) has been adopted. Short observations are made at widely separated hour angles, where each individual observation determines the source position in one dimension. Lobe ambiguities are absent for Parkes catalogue sources, since the positional errors are much less than one lobe spacing. The intersection of these 'cuts' then yields the source position. The sequence of sources is usually selected to be at roughly constant declination and hour angle so that the local antenna coordinates remain roughly constant for those sources.

Normal observations are accumulated for 5 min, yielding an rms noise of 0.9 mJy. In practice the source positional accuracy for weak sources is limited by background confusion rather than system noise. Figure 1 shows the amplitude distri-

bution for 70 high-galactic-latitude random fields; the distribution is sharply peaked around 6 mJy. For a 50 mJy source this corresponds to an rms phase error of $(6 \times 180)/(50\pi\sqrt{2}) = 5°$, or a positional error of $\sim 2''$ arc.

In order to calibrate the instrumental phase and also to determine an accurate baseline, a number of sources with accurate ($< 1''$ arc) radio and optical positions have been observed over a wide range of hour angles. As the two antennas are of differing mounts, the baseline equation has additional terms over that normally employed for identical antennas. At all times the phase drift has been observed to be much less than $2° \text{ h}^{-1}$ and easily followed by observing a calibration source once per hour. Figure 2 shows the observed phase error distribution from observations of a selection of small-diameter sources from the Parkes ±4° catalogue (Ref. 4) for which accurate positions have been measured with the RRE Malvern interferometer (Ref. 5). These show an rms phase error of $3°.5$, corresponding to a position error of $\sim 1''.5$ arc. Figure 3 shows a comparison between the Tidbinbilla and Malvern positions: the larger scatter in right ascension results from the two cuts being separated by only 3-1/2 h of hour angle, so that the two cuts were only 30° apart on the sky.

By combining the observations from a number of observing sessions it has been possible to refine the baseline parameters to give an rms phase error of $< 4°$ over the available sky at elevations $> 20°$. This corresponds to a positional accuracy in one dimension of typically $2''$ arc. The measured confusion error discussed above shows that an rms positional uncertainty not exceeding $3''$ arc should be achievable for compact sources stronger than 50 mJy at high galactic latitude.

The instrument also provides high-accuracy flux density measurements for compact radio sources. Figure 4 shows a comparison between the measured Tidbinbilla flux densities and interpolated flux densities based on the Parkes 2.7 GHz measurements and measurements at Arecibo at 318 MHz (Ref. 6). Once again the sources were selected to be compact with normal spectra, to exclude likely variables, and chosen from the Parkes ±4° catalogue. Dividing the observed scatter equally between the two sets of measurements leads to an intensity proportional error of 1.8%.

Programmes are underway to provide accurate radio positions for southern radio sources. Preliminary results are given in Figure 5, where the radio-optical differences for 11 compact sources selected from the sixth part (declination zone -30° to -35°) of the Parkes 2.7 GHz catalogue (Ref. 7) are shown.

Once again the expected right ascension error is larger than the declination error because of the small separation in hour angle of the two cuts. Among the resulting identifications is an X-ray object (PKS 2155-304) which we find to be a radio variable 14th-magnitude BL Lac object: the radio and optical positions differ by less than $1''$ arc in both coordinates.

Acknowledgment

References

1. Jauncey, D. L., Wright, A. E., Peterson, B. A., and Condon, J. J., *Astrophys J. (Lett.)*, 223, L1 (1978).

2. Batty, M. J., Jauncey, D. L., Gulkis, S., and Yerbury, M. J., *Proc. Astron. Soc. Aust.*, 3, 115 (1977).

3. Adgie, R. L., Crowther, J. H., and Gent, H., *Mon. Not. R. Astron. Soc.*, 159, 233 (1972).

4. Wall, J. V., Shimmins, A. J., and Merkelijn, J. K., *Aust. J. Phys. Astrophys. Suppl.* No. 19 (1971).

5. McEwan, N. J., Browne, I. W. A., and Crowther, J. H., *Mon. Not. R. Astron. Soc.*, 80, 1 (1975).

6. Condon, J. J., and Jauncey, D. L., *Astron. J.*, 79, 437 (1974).

7. Shimmins, A. J., and Bolton, J. G., *Aust. J. Phys. Astrophys. Suppl.* No. 32 (1974).
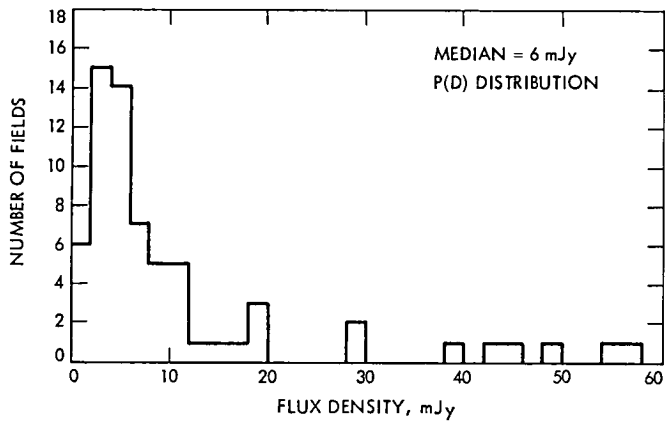
Fig. 1. The amplitude distribution, P(d), for 70 high-galactic-latitude random fields
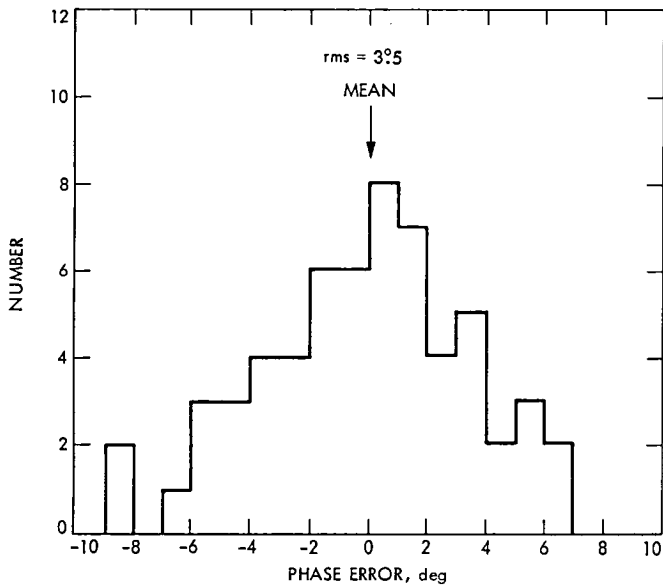
Fig. 2. The observed phase error distribution (TBB-RRE) for 30 small-diameter sources from the Parkes ±4° catalogue
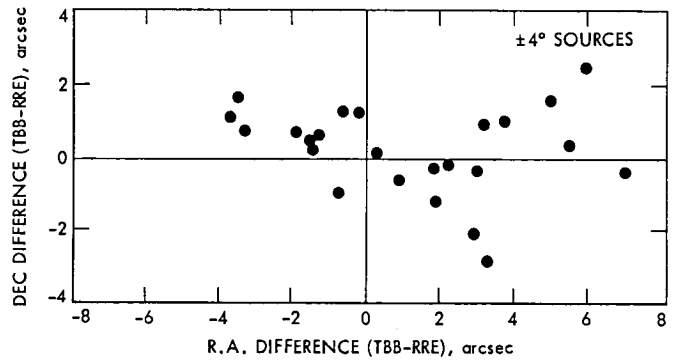
Fig. 3. A comparison between the Tidbinbilla and RRE Malvern position measurements for the ±4° sources
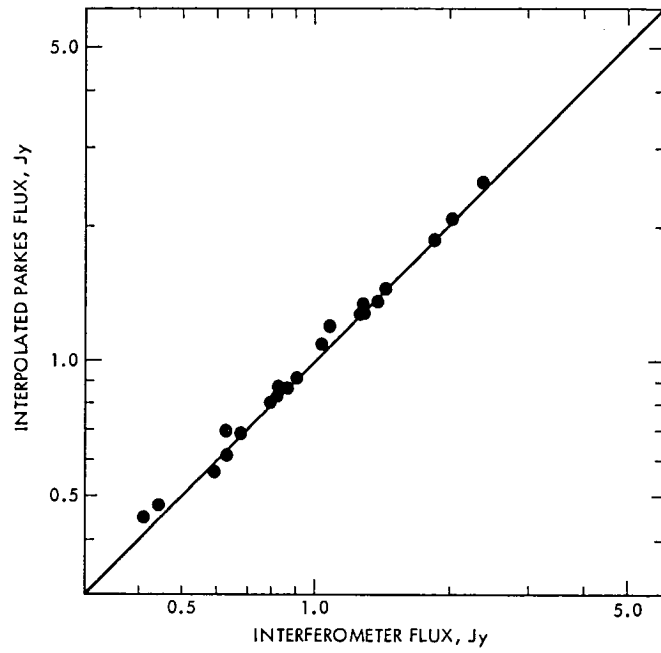
Fig. 4. Flux density comparison between the Tidbinbilla and Parkes measurements for 21 normal-spectrum compact sources from the ±4° catalogue
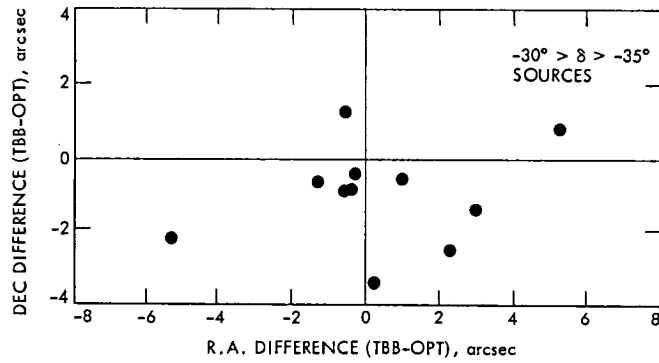
Fig. 5. A comparison between the Tidbinbilla radio and optical positions for the preliminary results from the Parkes −30° to −35° declination catalogue

The Tidbinbilla Interferometer

M. J. Batty and D. L. Jauncey
Division of Radiophysics, CSIRO, Sydney, Australia

S. Gulkis
Planetary Atmospheres Section

M. J. Yerbury
University of Sydney, Australia

Originally printed in the Proceedings of the Astronomical Society of Australia, *this article discusses a proposal to operate a two-element interferometer using the 64-m and 26-m antennas of the Tidbinbilla Deep Space Station.*

The reliable detection and identification of weak, small-diameter radio sources require an instrument with both high sensitivity and high positional accuracy.

The 3.9-m Anglo-Australian telescope is a powerful complementary optical tool for studying weak radio sources, but for unambiguous optical identifications, radio positional measurements to within ~1-2″ arc are highly desirable and often essential. Although some southern hemisphere radio telescopes (the Fleurs synthesis telescope and the Molonglo Cross) provide positional accuracy at or near this level, their sensitivity is generally not high enough to permit rapid searches for sources having flux densities in the millijansky range. The Tidbinbilla interferometer system, largely utilizing existing JPL facilities, will provide an instrument having a combination of sensitivity and positional measurement accuracy unequalled in the southern hemisphere, and with very little capital outlay.

It is proposed to operate a two-element interferometer using the 64-m and 26-m antennas of the Tidbinbilla Deep Space Station near Canberra, A.C.T. operating at a frequency

of 2.3 GHz. With a north-south baseline of ~1500 λ, a positional measurement accuracy approaching 1″ arc appears to be achievable with good sky coverage; the sensitivity of ~1.6 mJy/h⁻¹ means that sources with flux densities to ~10 mJy may be reliably detected and positions measured in a few minutes' observing.

The parameters of the system are as follows:

Operating frequency	2.3 GHz
Baseline length	200 m (north-south)
Lobe separation	2′.3 arc
Predetection bandwidth	12 MHz
Effective system temperature	25 K
IF frequency	70 MHz
Sensitivity	~1.6 mJy/h⁻¹
	(5 × r.m.s. noise)

A block diagram of the system is shown in Fig. 1. The receiver first stages consist of low-noise travelling wave masers having bandwidths of ~40 MHz. These are normally employed

for spacecraft down-links at the station. The 2.22 GHz local oscillator system (Fig. 2) employs a system which has been previously described by Little (1969). The local oscillator signals at the two receivers are derived from phase-locked cavity oscillators. The input reference frequency (96.52 MHz) for these oscillators is synthesized from two signals near 48 MHz (but differing slightly in frequency) which are exchanged along a common cable link between the two receivers. The phase changes in the 96.52 MHz signal resulting from thermal and mechanical effects in this line then depend only on the frequency difference between the two ~48 MHz signals. This difference is chosen to be suitably small (~0.5 MHz).

A stepped compensating delay, inserted into one arm of the interferometer (see Fig. 1), consists of lengths of low-loss 1.3-cm-diameter styroflex coaxial cable. These lengths are chosen to be binary multiples of one wavelength at the intermediate frequency of 70 MHz. This choice of a minimum delay step eliminates extra phasing requirements and results in an average gain error of $< 1\%$ due to operation off the peak of the correlation envelope. The worst phase error of the delay line system is $< 1°$. The total delay is determined by the configuration of coaxial switches, and will be computer-controlled to facilitate source tracking.

The instrument will be operated as a correlation interferometer, the sine and cosine products being sampled once per second and recorded for later analysis. A small amount of on-line processing may be possible with the facilities available. It will also be possible to monitor gain changes, since each aerial system can operate as a noise-adding radiometer.

The receiver systems are currently under development at the CSIRO Division of Radiophysics, and preliminary measurements of the delay line and local oscillator systems and the site cables suggest that a phase stability to within ~1° should be achievable with temperature control of the receiver packages. Figure 3 shows the measured variation of phase for the local oscillator system with some thermal lagging, but no temperature stabilization. The average drift rate is $< 2°$ h^{-1}, with fluctuations of $\lesssim 1°$. A phase error of 1° corresponds to a positional error of ~0".4 arc at the zenith, so that the target positional measurement capability of ~1" arc appears to be within sight. It is expected that a working system can be established within a few months.

Possible future developments include the extension of the system to include the Honeysuckle Creek 26-m antenna, approximately 16 km south, by means of a microwave link, and a fourfold increase in operating frequency. This would provide an instrument with an absolute positional measurement accuracy of $<0".01$ arc. Potential applications of such a system could include the determination of a southern hemisphere astrometric grid from radio measurements and a search for positional shifts in nearby stars due to planetary companions.

Acknowledgment

Reference

1. Little, A. G., *IEEE Trans. Antennas Propag.*, AP-17, 5, p. 547 (1969).
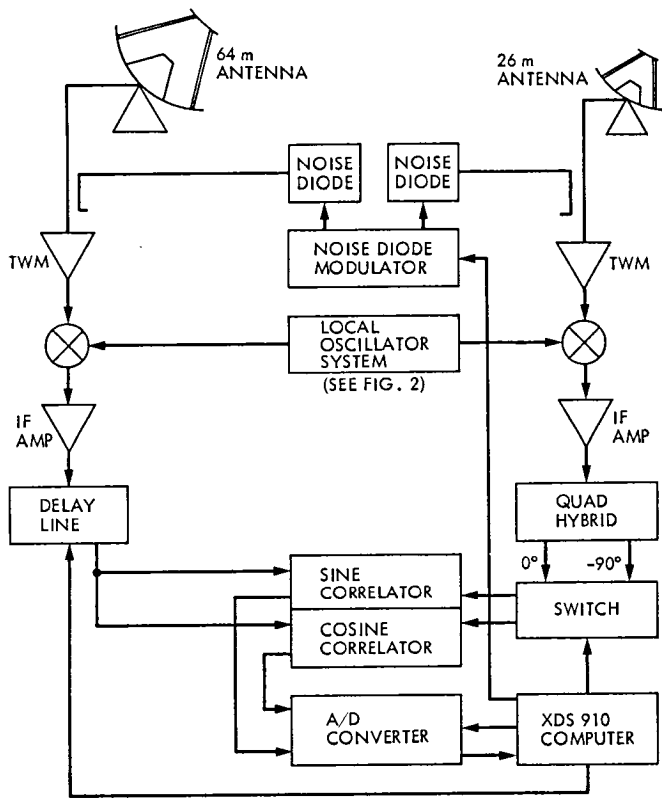
Fig. 1. Schematic diagram of the Tidbinbilla interferometer
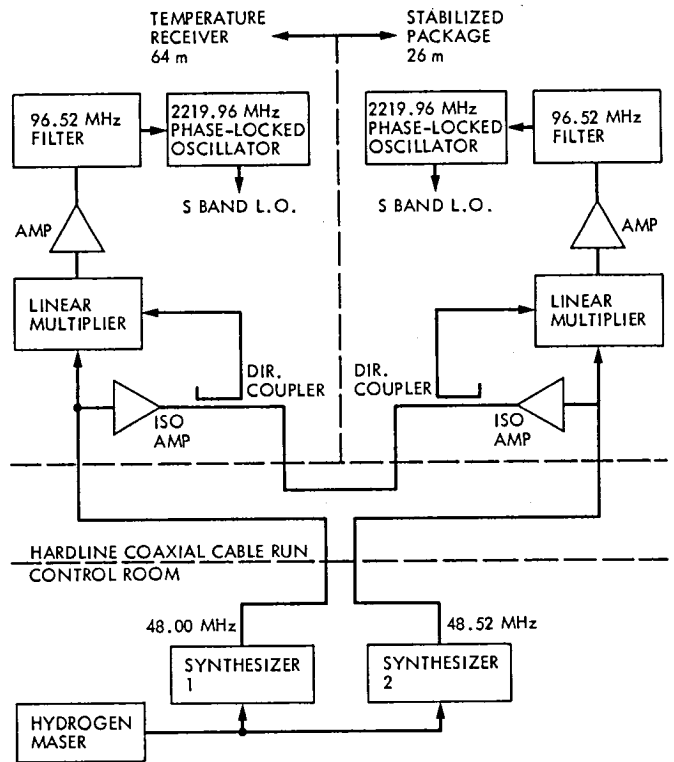
Fig. 2. Schematic diagram of the local oscillator distribution system
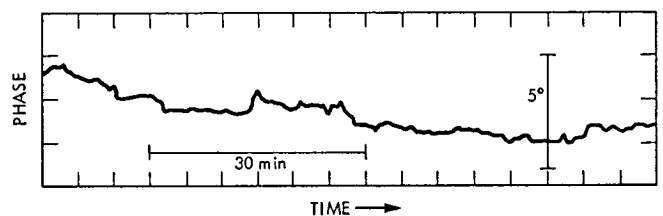
Fig. 3. Typical record of relative phase difference between the outputs of the local oscillator system, measured over a 90-min period. For this test no temperature stabilization was used, although the system was thermally lagged

Digital Recording Acquisition Subsystem for Radio Interferometry Applications Implementation Plan

V. B. Kapoor

DSN Data Systems Section

This is the first in a series of articles describing the implementation of the Digital Recording Acquisition Subsystem (DRAS) for radio interferometry applications in support of NASA's Crustal Dynamics Project. This article describes the functional and performance characteristics of the equipment and the key aspects of the implementation plan.

I. Introduction

The Digital Recording Acquisition Subsystem (DRAS) being implemented for NASA's Crustal Dynamics Project is the operational version of the so-called Mark III Data Acquisition System. Introduced in 1978, the Mark III System is a digital recording system developed jointly by Goddard Space Flight Center (GSFC), Haystack Observatory, National Radio Astronomy Observatory (NRAO), and Massachusetts Institute of Technology (MIT). The Mark III System is being adapted for the mobile Very Long Baseline Interferometry (VLBI) applications with emphasis on operability, reliability, maintainability and severe environmental considerations. As part of the Crustal Dynamics Project managed by GSFC, the initial application of the DRAS equipment will be for the Astronomical Radio Interferometric Earth Surveying (ARIES), Operational Radio Interferometry Observational Network (ORION), and Deep Space Network (DSN) Block II VLBI projects.

II. Functional Overview

The DRAS is a wideband digital recording system that can accommodate data sample rates from 0.125 to 8 MHz in binary increments. The DRAS equipment configuration is shown in Fig. 1. A functional block diagram of the DRAS is shown in Fig. 2.

III. Important Functional Characteristics

A summary of the important functions and performance characteristics of the equipment is as follows:

A. Important Functions

The DRAS performs the following main functions:

(1) Receives and records VLBI and calibration data supplied by Receiver Subsystem as clipped video signals.

(2) Adds housekeeping information to the basic user data for recording.

(3) Provides real-time and non-real-time recording performance monitor and diagnostic capability.

(4) Reproduces data for post-real-time processing or data reduction.

(5) Provides for remote control of the Subsystem.

(6) Provides a dual-recorder configuration for continuous (overlapped) recording capability and as a warm backup in case of equipment failure in the field.

B. Performance Characteristics

The DRAS has the following performance characteristics:

(1) Instrumentation recorder using 2.5-cm (1-in.) tape on 35.6-cm (14-in.) diameter reels.

(2) Record/reproduce heads with 28 tracks according to Electronic Industries Association (EIA) standards.

(3) Longitudinal density of 13 kbits/cm/track.

(4) Recording code used is non-return to zero mark (NRZM).

(5) Operating modes are normal (recording on all 28 tracks) or shuttle (any number of tracks recorded in successive forward and reverse passes of the tape).

(6) Local or remote control via ASCII teletype current loop or RS232C interface.

(7) Is compatible with the Haystack Mark III data format as shown in Fig. 3.

IV. Key Aspects of Implementation Plan

A. Availability from Commercial Sources

In April 1979, it was jointly agreed between GFSC, Haystack Observatory, and JPL that a commercial source must be found and contracted to replicate the Mark III Data Acquisition System.

JPL agreed to generate documentation packages for competitive procurement bids and identify commercial sources to fabricate complete Mark III systems with JPL acting as the systems contractor for the first unit. For subsequent units, a commercial systems contractor will be sought.

JPL contracted Haystack Observatory to deliver two (2) Mark III Data Acquisition Systems in July 1980 and March 1981, respectively, to ARIES in order to meet its schedule commitments in support of the Crustal Dynamics Project.

B. Operability and Reliability Considerations

The most common reservations generally expressed about recording equipment center around operability, maintainability and reliability. The Mark III System was not designed for the mobile environment (mounted inside an electronics van) as required by ARIES and ORION projects. In an attempt to be responsive to these concerns, the following system design goals apply:

(1) The recorder electronics equipment will be ruggedized to withstand shock and vibration due to roadability and air transportability requirements.

(2) An automated prepass performance verification of the recording equipment will be provided.

(3) Some degree of real-time read-after-write data monitoring capability will be provided.

(4) The Monitor and Control Subsystem will remotely monitor and control the DRAS operation.

(5) Tape change will be the only real-time function that the operator will perform; all other functions such as starting, stopping, and rewinding tape will be automated.

(6) The DRAS mean time between failures will be more than 600 hours.

(7) There will be no mechanical or electrical adjustments associated with the recorders.

(8) Modular design will facilitate troubleshooting and repair.

C. Environmental Considerations

The sites that the mobile stations will visit will be very diverse geographically as well as weatherwise. The following conditions are extremely detrimental to the recorder equipment:

(1) Sand and dust can wear the record/reproduce heads rather critically. The head stacks are very expensive and the quality of data recording will be deteriorated significantly. A system will be designed to provide clean, filtered air in the head area.

(2) Relative humidity (RH) chemically reacts with the binder material in almost all the tapes commercially available to be used on the recorder equipment. The design goal will be to keep the head-tape interface area inside the recorder to approximately 50% RH to prevent tape degradation.

V. Current Status Summary

A brief description of the various activities in progress is as follows:

A. Documentation

(1) A large portion of the documentation of the DRAS equipment has been input into the JPL Document

Control. Haystack Observatory (with drafting support from JPL) is currently working on finalizing the Recorder Electronics documentation.

(2) JPL has already initiated the generation of Technical Requirements Documents (TRDs) and/or specifications for the DRAS equipment.

(3) Test procedures will be generated jointly by Haystack and JPL.

B. Hardware

(1) Various options are under study to determine the most cost-effective approach to ruggedizing the DRAS equipment.

(2) Designs to provide clean and controlled environment in the head-tape interface area are being evaluated.

(3) JPL Quality Assurance (QA) personnel are working closely with Haystack personnel to resolve QA problems on systems to be delivered to the ARIES project.

C. Commercial Sources

A potential list of commercial sources with capability and experience to manufacture, test, deliver and document DRAS equipment is being generated.

Subsequent articles will cover the implementation status in greater detail.
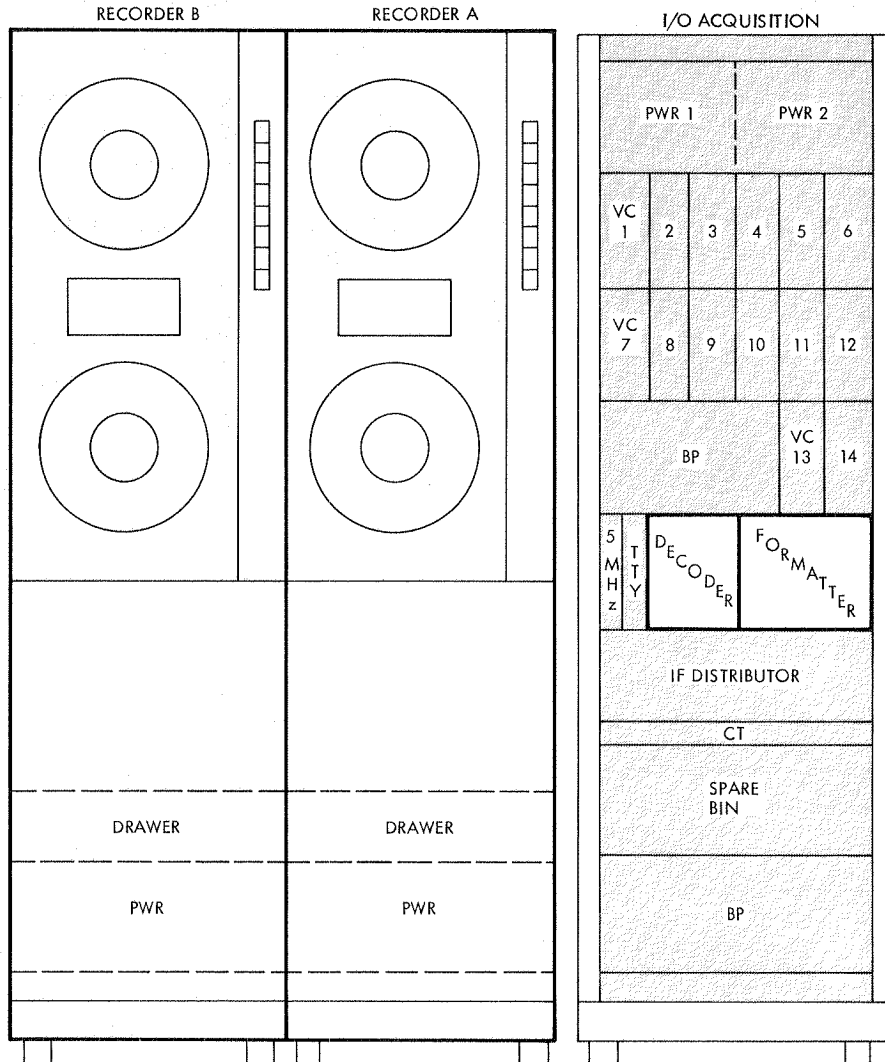
Fig. 1. Equipment configuration, Digital Recording Acquisition Subsystem
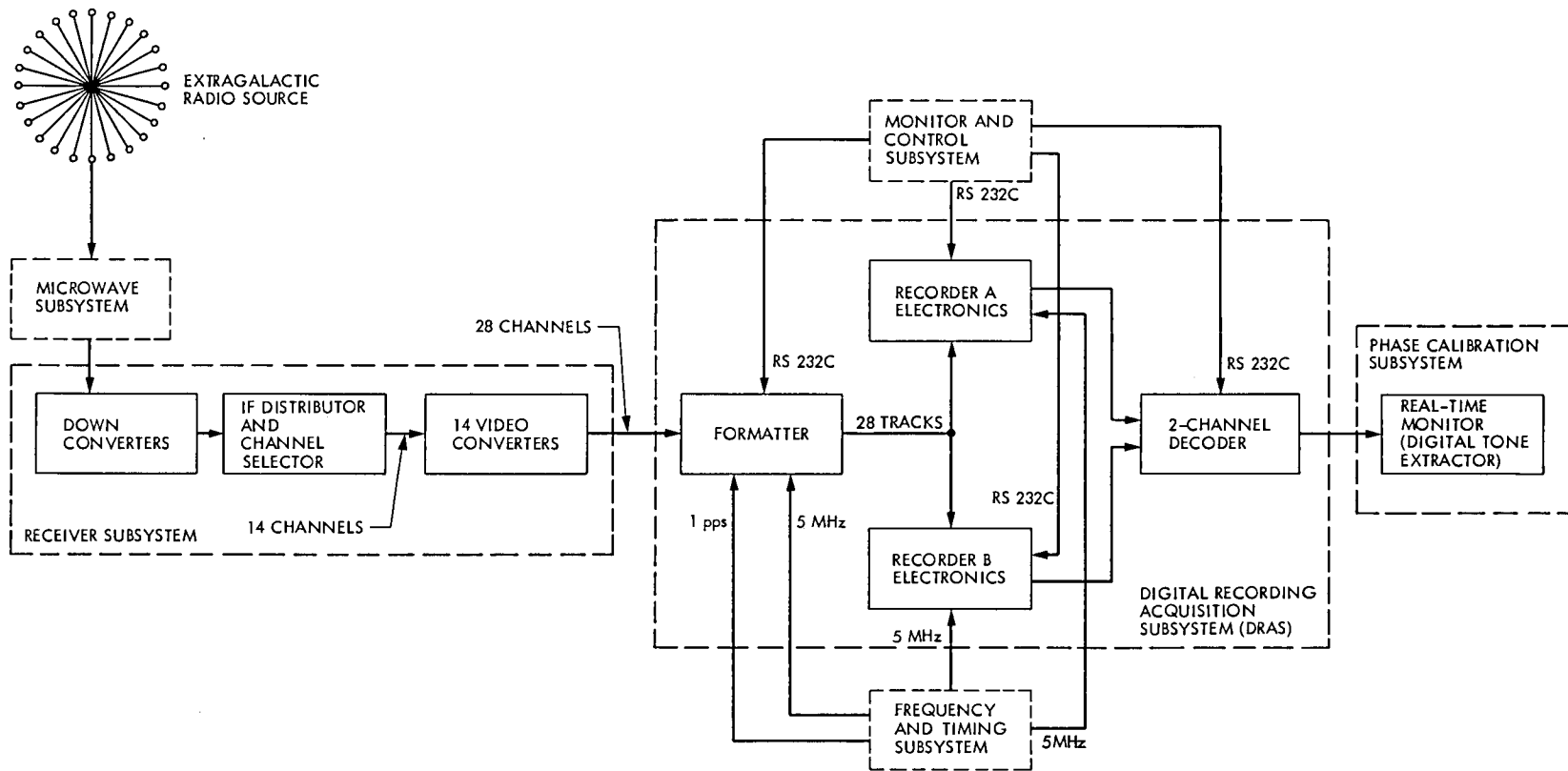
Fig. 2. Functional block diagram, Digital Recording Acquisition Subsystem

1 FRAME = 125 BLOCKS (5 msec PERIOD AT 4 Mbit/sec SAMPLE RATE)
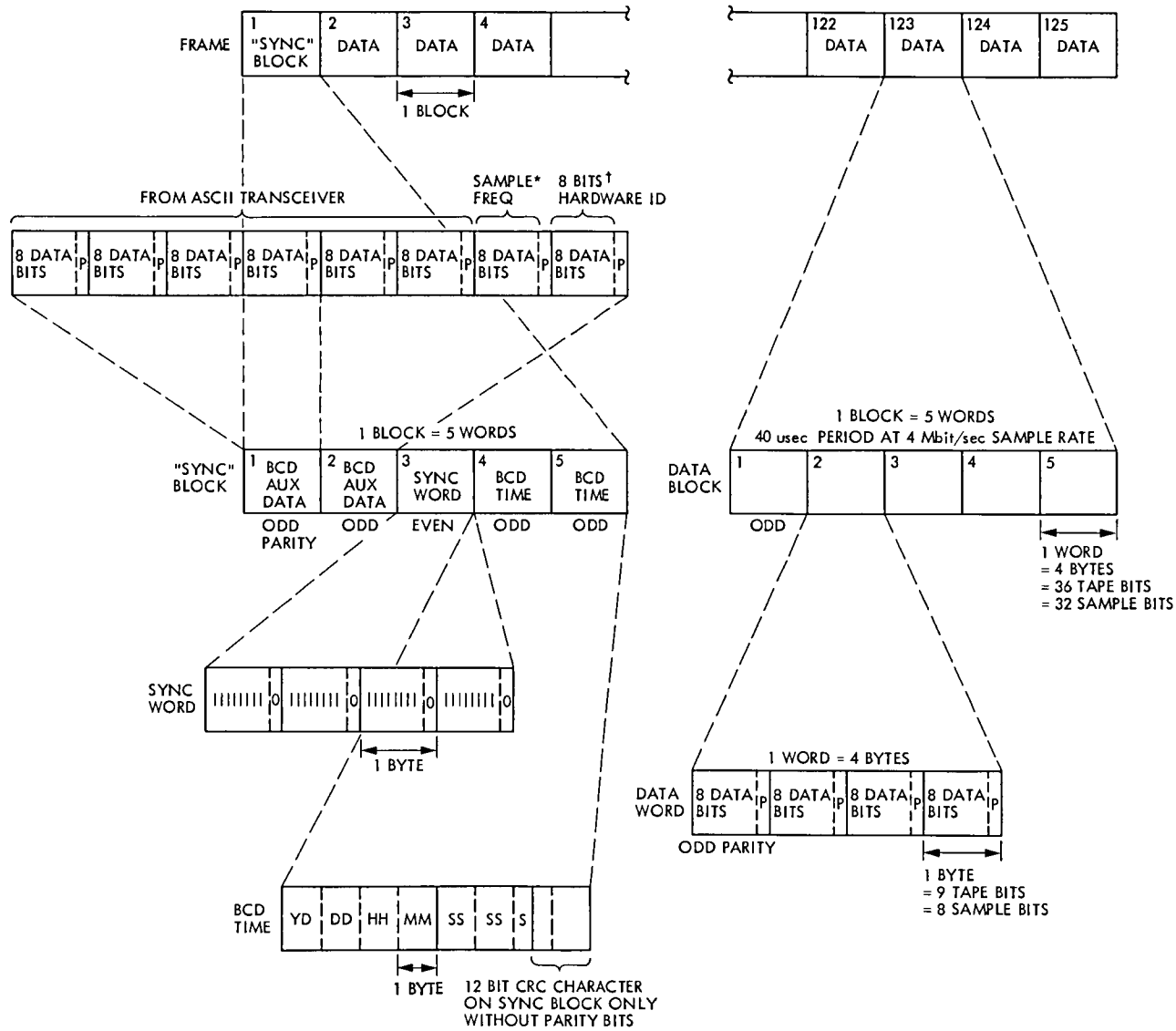
*SAMPLE FREQUENCY CODE

00_8	8 Mbits/sec
07	4
06	2
05	1
04	0.5
03	0.25
02	0.125

† HARDWARE ID CODE SHOULD HAVE
AT LEAST ONE BIT SET TO ZERO

Fig. 3. Mark III data format

VLBI System for Weekly Measurement of UT1 and Polar Motion: Preliminary Results

M. Roth and T. Yunck
Tracking Systems and Applications Section

The DSN implementation of a system for measuring UT1 and polar motion using very long baseline interferometry (VLBI) is currently being tested. VLBI experiments are being conducted on a weekly basis on each of two intercontinental baselines. During a 17-day period in September 1979, data were obtained for seven consecutive experiments using an early version of that system. Those experiments, described here, were used to refine the estimation procedure to be used in the operational system and to provide a preliminary assessment of the performance of the system.

I. Introduction

To help meet the coming need for high-accuracy navigation at outer planet distances with rapid turnaround during encounters, the DSN will soon begin operating its own system to measure UT1 and polar motion by means of very long baseline interferometry (VLBI) (Refs. 2, 7, 8, 9). In astrometric applications, VLBI has already achieved more than an order-of-magnitude improvement in angular resolution compared to the best optical techniques (Ref. 5). Angular uncertainties at the 10-milliarc-second level are now being reported for radio source positions and additional improvements can be expected. For future spacecraft navigation the desired angular uncertainty for the orientation of the Earth is less than $0.''01$ in each axis (Ref. 3). This translates to 0.7 ms in UT1 and 30 cm for both the X and Y components of polar motion. In its present configuration, the VLBI system should be able to achieve the desired accuracy with relatively short (<2 hr) passes. Previously reported experiments used from 10 hours to 24 hours of antenna time (Refs. 2 and 6).

A catalog of radio source positions is the basis for any VLBI measurement. Preliminary analyses of the effect of source position errors on the measurement of Earth orientation indicate that the source positions must be known to about $0.''01$. The best sources in the JPL catalog now satisfy this requirement (Ref. 1) and continued improvement of the catalog will provide additional sources that are needed to fill gaps in certain parts of the sky.

From the known source positions the baseline vector connecting two VLBI stations can be determined in an inertial frame. If the earth-fixed coordinates of the baseline are known, Earth orientation can be determined except for a rotation about the baseline. To uniquely determine the Earth orientation it is therefore necessary to observe on two non-parallel baselines. Errors in baseline coordinates change the baseline orientation with respect to the Earth. Therefore, these coordinates must be known to an accuracy of about $0.''01$ (0.3 m) in order to achieve the desired accuracies for

UT1 and polar motion. The accuracy goals for the system and a priori requirements for source positions and baseline vectors are summarized in Table 1.

The operational system, referred to as the Block I implementation, calls for weekly observing sessions of approximately 90 minutes on each of two intercontinental baselines, typically Goldstone-Madrid and Goldstone-Canberra, using 64-meter antennas. Simultaneous observations on both baselines are not possible because of visibility limitations. When the observations are not taken simultaneously, the motion of the pole and changes in UT1 between sessions introduce additional uncertainty in the estimates for these parameters. From their known rates of change, it was determined that a maximum baseline observation separation of 24 hours is consistent with the desired accuracies.

The observing schedule calls for 10 source scans (scans may repeat sources) recorded at 500 kb/s for a total of 1×10^9 bits on each of two baselines. From these data, seven parameters will be estimated: UT1, polar motion (X, Y), clock epoch offsets for two stations with respect to the third station and the two corresponding clock offset rates. In the Block I system, the data will be transmitted from each of the DSN stations to JPL over the wideband data link. It is expected that during critical events such as planetary encounters, results can be produced within 24 hours from the time of data acquisition. The operational goals for Block I are shown in Table 2.

II. Experimental Procedures

Data for the present study were recorded and processed using the developmental Block O system. The Block O procedures, summarized in Table 3, differ in certain respects from those of operational Block I. Most importantly, the number of source scans on each baseline was smaller than desired, ranging from 2 to 12, with 5 about average. In addition, the data were recorded at 4 Mb/s on video tapes, which were shipped to JPL for processing and parameter estimation.

Using the VLBI fitting software on the IBM 3032 at Caltech, Earth orientation and station clock parameters were estimated from the seven experiments summarized in Table 4. The normal operations schedule calls for a maximum separation of 24 hours between baselines, but a preliminary analysis indicates that a 48-hour separation could be tolerated. Four of the baseline pairs meet the 48-hour requirement. However, the ability to use even larger separations would be advantageous, particularly in cases where data are available for only one baseline of a scheduled pair. To test the effect of larger separations, three additional pairs of baselines were processed with separations of 7 to 15 days. The resulting reference times for the Earth orientation parameters (UT1, X-pole and Y-pole)

are the means of the observation times on each pair of baselines. The pairs chosen give reference times spanning the 17-day period covered by the experiments. Each pair of baselines was used to estimate UT1-UTC, X-pole, Y-pole and the clock offsets and rates for DSS 43 (Canberra) and DSS 63 (Madrid) with respect to DSS 14 (Goldstone).

III. UT1, Polar Motion Results

Figures 1 – 3 show the results for the Earth orientation parameters. The individual experiments are shown along the time axis and are keyed by baseline. The pair of numbers next to each data point identifies the experiments from which the data were taken. For comparison, the figures show the difference between the VLBI values and the values computed by the Bureau International de l'Heure (BIH) and published monthly in Circular D. The dashed lines show the means of the VLBI-BIH values. The error bars shown do not consider the effects of errors in baseline vectors or source positions, which can introduce additional random and systematic errors in the orientation parameters. The effect of baseline time separation has been included in the errors for X-pole and Y-pole, using the rates of change of these parameters obtained from the BIH values.

The results for UT1-UTC show formal errors ranging from 0.5 ms to 4.3 ms. The large error in 68-69 is due to the small number of scans and poor data quality of experiment 68. The mean difference between the VLBI and BIH values was -0.81 ms, which is smaller than the accuracy quoted by BIH and can be attributed to a difference in the origins of the VLBI and BIH coordinate systems. With the mean difference removed, the VLBI estimates have an rms deviation from BIH of 0.91 ms. If pair 68-69 is deleted, the mean difference and rms deviation are reduced to -0.55 ms and 0.69 ms, respectively.

For the X- and Y-pole estimates, the formal errors range from 0.″008 to 0.″073. The larger errors in the baseline pairs 66-69, 67-70, and 69-70 are primarily due to the baseline separations, which are 8, 15, and 7 days, respectively. Experiment 68 again degrades the estimates for 68-69. The errors in the remaining pairs are about 0.″010, which is typical for good data on close baselines. The mean difference between the VLBI and BIH X-pole estimates is -0.″043 with an rms value of 0.″019. (With pair 68-69 deleted, the mean difference is -0.″036 with an rms of 0.″008.) The Y-pole estimates have a mean difference of -0.″005 with an rms of 0.″009.

IV. Conclusions

The rms deviations, summarized in Table 5, are a measure of the random error uncertainties in the parameter estimates. The rms values for UT1 and X-pole are larger than the desired

levels given in Table 1, while the value for Y-pole is smaller. When baseline pair 68-69 is not included, the rms values for all parameters are consistent with the accuracy goals. While it is not claimed that these results constitute a validation of system performance specifications, they do indicate that the specified performance is attainable. In support of this conclusion, we note that several factors in the Block O system which contribute to the uncertainties of the estimates will be eliminated or reduced in the Block I system. Although the best available station locations and source positions were employed, they must still be regarded as preliminary because they do not completely satisfy the stated accuracy requirements. Calibrations for certain components of the VLBI delay observable will also be improved in the Block I system. The present data were processed using a fixed tropospheric delay at zenith and no instrumental delay calibration was available. In the operational system, atmospheric conditions will be monitored, including water vapor content, to determine the wet and dry components of the tropospheric delay (Ref. 4). In addition, phase calibration of instrumental delays will be performed (Ref. 10). Other sources of error are present in the models for Earth precession and nutation. These models will be improved as additional VLBI source catalog data become available. Finally, it should be possible to increase the fraction of successful source scans and to minimize the time separation between baselines through better scheduling of observations. These improvements should enable the operational Block I system to meet or exceed the specified accuracy requirements.

References

1. Purcell, G. H., et al., "Current Results and Developments in Astrometric VLBI at JPL," IAU Colloquium No. 48, Vienna, Austria, 1978.

2. Fanselow, J. L., et al., "Determination of UT1 and Polar Motion by the Deep Space Network Using Very Long Baseline Interferometry," Proceedings of IAU Symposium No. 82, Time and the Earth's Rotation, 1979, pp. 199-209.

3. Melbourne, W. G., and Curkendall, D. W., "Radiometric Direction Finding: A New Approach to Deep Space Navigation," AAS/AIAA Astrodynamics Specialist Conference, Jackson Hole, WY, 1977.

4. Resch, G. M., et al., "Atmospheric Water Vapor Calibrations: Radiometer Technique," DSN Progress Report 42-32, Jan.-Feb. 1976, Jet Propulsion Laboratory, Pasadena, Calif., pp. 38-49.

5. Shapiro, I. I., "Estimation of Astrometric and Geodetic Parameters from VLBI Observations," in Methods of Experimental Physics, M. L. Meeks, Ed. (Academic Press, New York, 1976), Vol. 12c, pp. 261-276.

6. Shapiro, I. I., et al., "Transcontinental Baselines and the Rotation of the Earth Measured by Radio Interferometry," Science, 186, 920-922, 1974.

7. Thomas, J. B., An Analysis of Long Baseline Interferometry, Part I, Technical Report 32-1526, Vol. VII, Jet Propulsion Laboratory, Pasadena, Calif., pp. 37-50.

8. Thomas, J. B., An Analysis of Long Baseline Interferometry, Part II, Technical Report 32-1526, Vol. VIII, Jet Propulsion Laboratory, Pasadena, Calif., pp. 29-38.

9. Thomas, J. B., An Analysis of Long Baseline Interferometry, Part III, Technical Report 32-1526, Vol. XVI, Jet Propulsion Laboratory, Pasadena, Calif., pp. 47-64.

10. Thomas, J. B., The Tone Generator and Phase Calibration in VLBI Measurements, DSN Progress Report 42-44, Jan.-Feb. 1978, Jet Propulsion Laboratory, Pasadena, Calif., pp. 63-74.

Table 1. Accuracy goals and a priori accuracy requirements

	Accuracy goals
UT1	− 0.7 msec
Polar motion	− 0.01 arc sec (0.3 m)

	Accuracy requirements
Baselines	− 0.3 m
Source positions	− 0.01 arc sec

Table 2. Operational goals

Weekly recording sessions of ~ 90 min on each of
two baselines (California-Spain, California-Australia) in 24 hr

Record ~ 1 × 10⁹ bits per baseline (10 sources)

Observe ~ 20 total sources on 2 baselines

Make measurements of UTI, polar motion (X, Y), clock
epoch offset, clock rate offset

Eventual 24-hr turnaround

Table 3. Experimental procedures

Observe on two baselines
 30 − 90 min (2 − 12 sources) each baseline
 S- and X-band observations
 28.2 MHz synthesized bandwidth
Record 4 Mbs data on video tape recorders
Correlate and estimate at JPL

Table 4. VLBI experiments

Experiment no.	Date, 1979	Baseline[a]	Sources
7966	10 Sept	14-63	4
7967	10 Sept	14-43	5
7968	17 Sept	14-63	2 (X-band only)
7969	18 Sept	14-43	5
7970	25 Sept	14-63	7
7971	25 Sept	14-43	12
7972	27 Sept	14-43	5

[a]Station codes: 14, Goldstone; 43, Canberra; 63, Madrid.

Table 5. Summary of UT1 and polar motion results

	VLBI − BIH	VLBI rms
UT1 − UTC	−0.81 ms	0.91 ms
X-pole	−0.043 arc sec	0.019 arc sec
Y-pole	−0.005 arc sec	0.009 arc sec
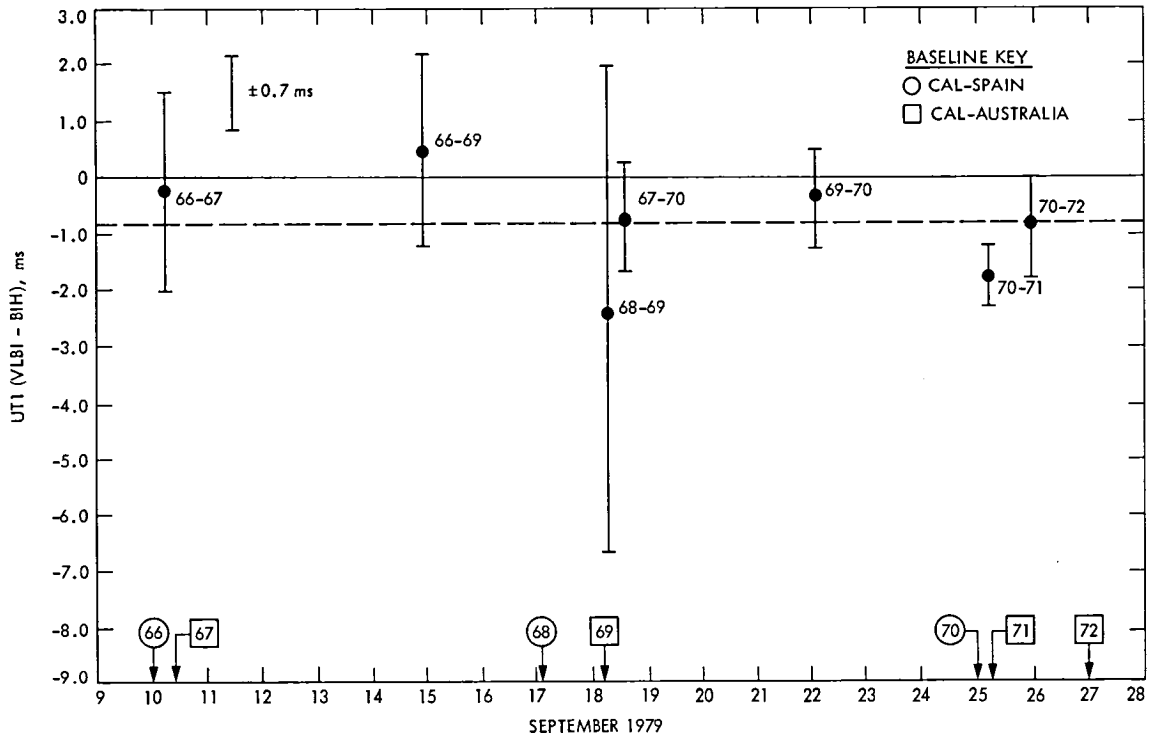
Fig. 1. UT1
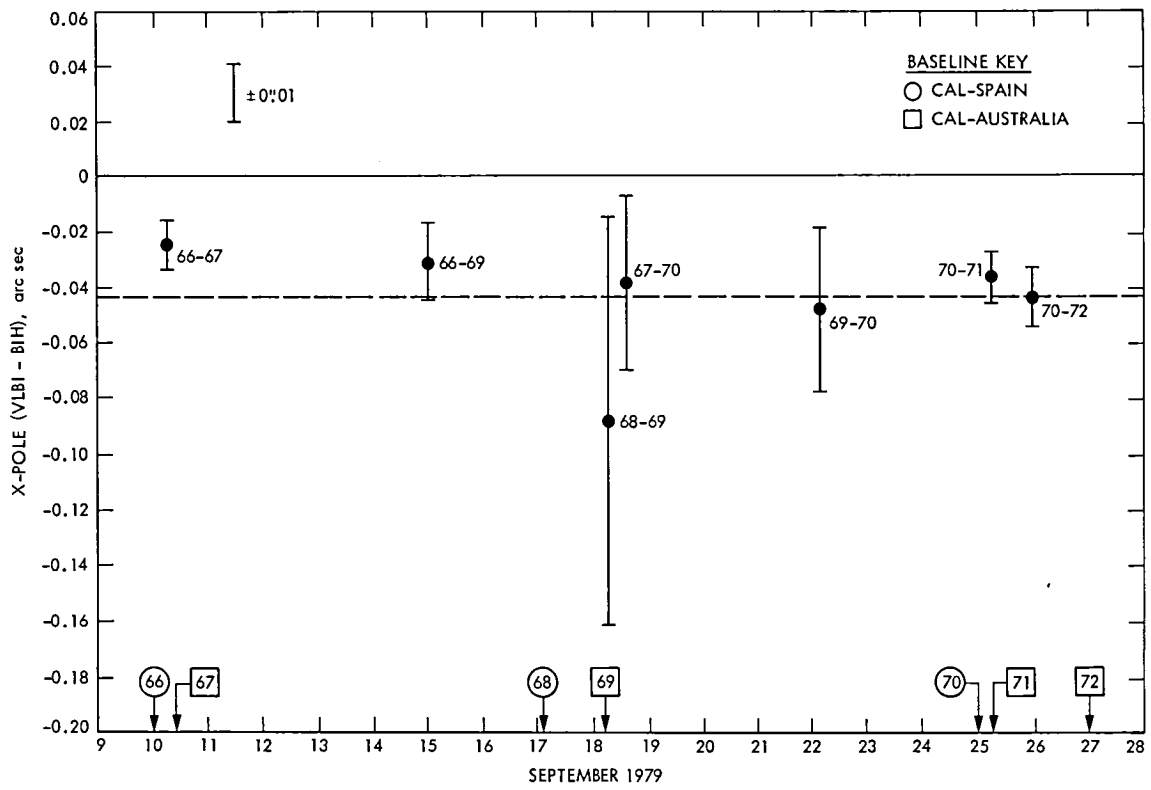
Fig. 2. Polar motion (X-pole)
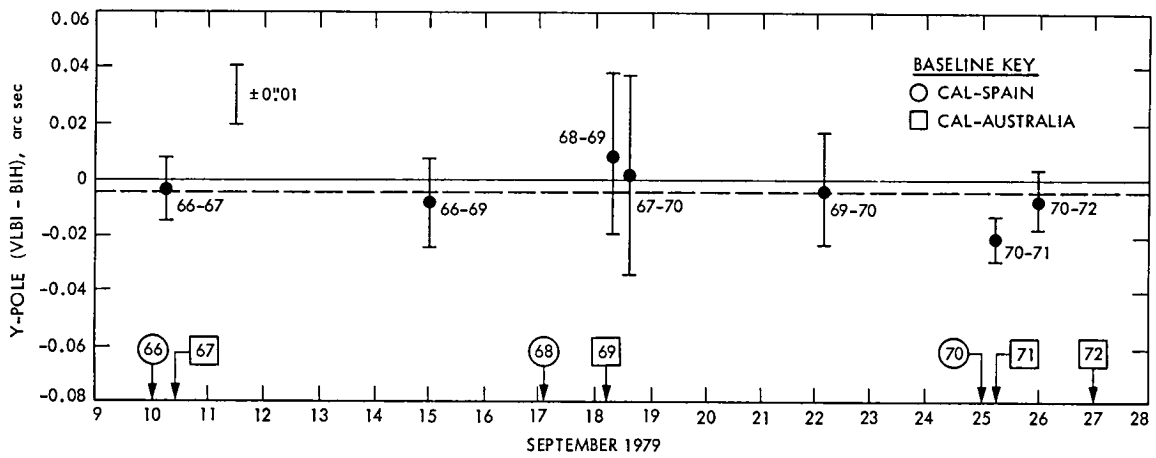
Fig. 3. Polar motion (Y-pole)

Progress Report on the Block I VLBI Correlator Implementation

J. C. Peterson and J. W. Dillon
DSN Data Systems Section

D. H. Rogstad
Tracking Systems and Applications Section

This article is a status report and final design summary for the DSN Block I VLBI Processor Subsystem.

I. Introduction

The DSN is currently in the process of implementing a very long baseline interferometry (VLBI) system for the determination of station clock-sync parameters, UT1 and polar motion, and station platform parameters and for use in spacecraft tracking. This article is directed toward what is referred to as the Block I VLBI Processor Subsystem (VPS) portion of this implementation effort. *DSN Progress Report 42-50*, page 226, presents a discussion of the correlator overall design and hardware detailed design, while here we are giving the current status of the VPS implementation and some of its key characteristics.

The Block I VPS performs three basic functions: it receives the 500-kbit/sec video data over the GCF wideband data lines from each of the three DSN 64-m antennas; it cross-correlates data; and finally, it performs several postcorrelation data reduction operations on the correlated data including calibration, editing and parameter estimation. The VPS hardware consists of a Digital Equipment Corp. (DEC) VAX 11/780 computer and the special purpose correlator hardware designed and built by the DSN and attached to the VAX

computer via high-speed DMA interfaces. The VPS software consists of a real-time interrupt driven program which resides in the VAX computer and controls the cross-correlation process, and of five non-real-time but interactive routines which also reside in the VAX computer and perform the postcorrelation functions.

II. Hardware

The communications hardware (Fig. 1) for tying the VPS to the GCF wideband data line has been installed and is currently undergoing tests. This equipment consists of 56 K-band modems and computer interfaces which will permit data to be transferred directly to the VPS from two DSN stations simultaneously for near-real-time data correlation.

The design and construction of the special purpose cross-correlation hardware has been completed. Validation tests have been performed module by module and also as a system. The hardware is presently being used together with the correlation software to process some preliminary VLBI video data. Results of these tests indicate that the system is

performing well. In its final configuration this hardware consists of six DSN standard subchassis including two Phase Processors, one Buffer/Mixer, one Cross-Correlator, one Correlator Processor, and one I/O Controller.

The Phase Processors, one for each video-data input stream, contain 32-bit microprocessors made up from AMC 2900 bit-slice chips. They perform the phase and phase-calibration linear updates every bit-time and the quadradic model updates every 5000 bit-times.

The Buffer/Mixer contains the delay line, the phase mixers, and the phase-calibration tone tracking for both data streams. The delay line, which is implemented using eight 16k dynamic RAMS, is 100k bits in length. The 3-level phase mixers, implemented in PROMS, has its output accumulated on the Cross-Correlation board. The phase-calibration tone trackers consist of 256-level mixers, 1k × 8 PROMS, and 32 bit accumulation for both sine and cosine.

The Cross-Correlator computes the cross-product sums using a 3-level by 3-level complex multiplication for 16 lags, and then accumulates the 32 results at the bit rate. Every 5000 bit-times this accumulated data is sent to the Correlator Processor for further processing.

The Correlator Processor performs a fast Fourier transform (FFT) and a fractional-bit-shift correction on the cross-correlated data. The FFT process results in series of 32 values representing the real and imaginary part of the input data cross-correlated at 16 lag points. These 32 values are then multiplied by a predetermined twiddle-factor to provide the fractional-bit-shift correction. The values are then accumulated for later transfer to the controlling computer.

The I/O Controller performs all information transfer between the correlation hardware and the controlling computer, except for the video data which is transferred through the Buffer/Mixer.

Each board has built-in self-test capabilities, some of which are performed at startup, some continuously, and some under computer control. All self-test status is available to the controlling computer.

III. Software

The RECEIVE program for receiving the VLBI video data over the wide-band data lines has been designed, coded and tested using IDR tapes as the source of input. The VAX system I/O driver for operating the wide-band line hardware interface to the computer has been written but not fully tested. Once this is completed, the video data can then be sent from each of the DSN 64-m antennas directly to the VPS, where it will be reformatted into records appropriate for the correlation process.

The MAKESCN program for converting the ancillary data into a correlation control record has been completed and tested (Fig. 2). The ancillary contains all the source scan information, recorder start-stop times, observing frequencies, weather data, etc., and is sent to the VPS over the wideband data lines in front of the video data. MAKESCN determines how this data is edited, merged together with similar data from both DSN stations and used to form the scan blocks for running the correlation process.

The CORLATE program for controlling the correlation process is completed and presently undergoing system tests with the correlator hardware. This routine is in the form of an interrupt handler. It reads the VLBI data and meters it time-synchronously to the correlator hardware. It calculates the geometric model parameters needed to perform proper correlation of the data and sends these to the hardware. It also outputs these model parameters, together with the correlation coefficients, to the postcorrelation record. Finally, it displays various status information and samples of the correlated data to the operator. All of these functions are normally performed under control of the Processor Control Record produced by MAKESCN, but with operator override capability.

The post-correlation software has been running in an RD mode for several years on the IBM 370 computer on the Caltech campus. This software consists of FORTRAN programs running in batch mode. These programs are to be converted to structured FORTRAN and made to run on the VPS VAX 11/780 computer. This conversion process is nearly complete at the present time.

In addition, the postcorrelation routines are to be restructured where necessary so that they can be run in an automatic mode under control of a control-record similar to that in the correlation process. Some of the routines will also be made to run interactively, with capability for operator intervention. This part of the implementation is still in the development stage and will not be complete until July 1981.
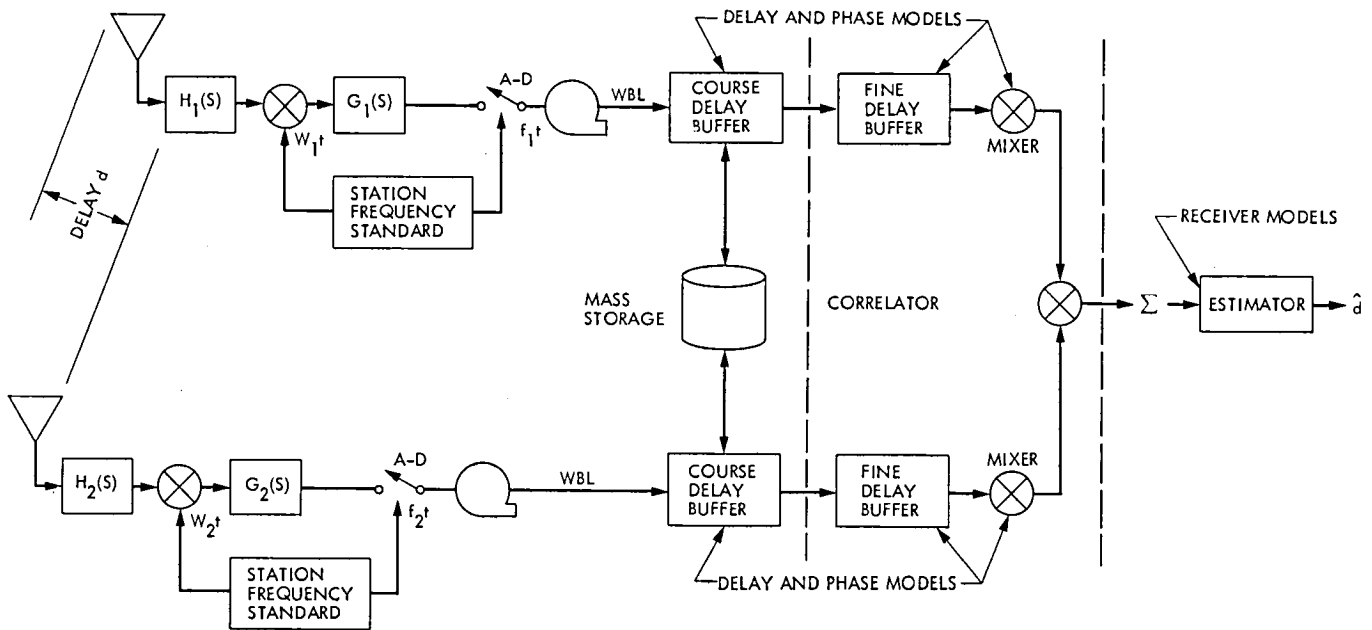
Fig. 1. VLBI data acquisition and processing (simplified)
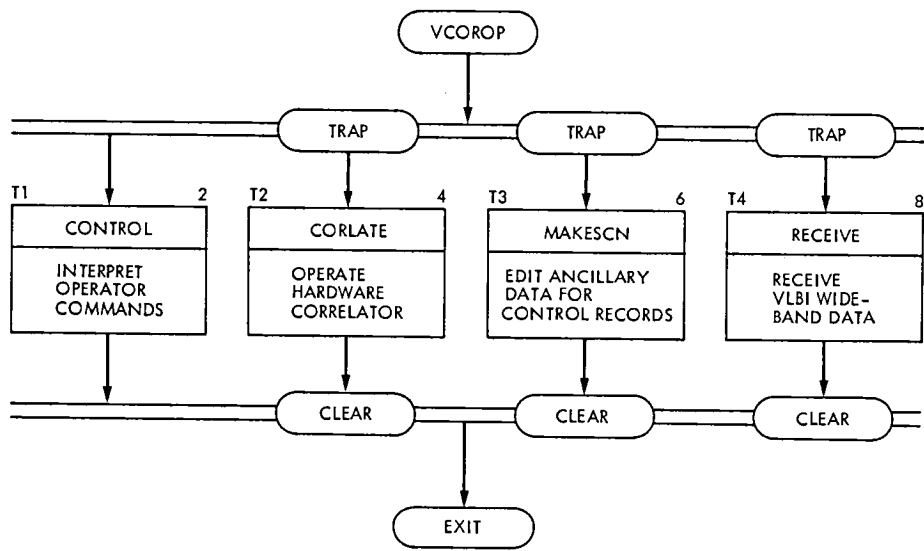
Fig. 2. Block I VLBI correlator software

Block I, Phase I Very Long Baseline Interferometry Implementation

J. H. Wilcher

DSN Data Systems Section

This article is a status report on the implementation of the Block I, Phase I VLBI System.

I. Introduction

The Block I, Phase I VLBI System has been implemented in the Deep Space Network and is currently undergoing system testing. The Block I, Phase I VLBI System (Ref. 1) can be characterized as the modification of existing equipment and the addition of new software in the 64-m subnet and the addition of new hardware and software in the Network Operations and Control Center (NOCC).

II. DSS Configuration

The DSS configuration for Block I, Phase I is shown in Fig. 1. The system utilizes the standard S-band and X-band Antenna Microwave Subsystem and Block IV Receiver Assembly along with the advanced systems VLBI IF converters. The Deep Space Station (DSS) Radio Science Subsystem has been modified by adding a VLBI converter subassembly and a wideband data interface to the Occultation Data Assembly. New Occultation Data Assembly software for Block I VLBI, along with modified software for the Metric Data Assembly and the Antenna Pointing Assembly have been supplied. No changes have been made to any of the remaining DSS subsystems for VLBI. Except for some mechanical change to the Antenna Mechanical Subsystem and the formal transfer of the Metric Data Assembly software, all subsystem changes required for Block I Phase I VLBI have been transferred to

Operations. The Antenna Mechanical Subsystem changes are expected by 1 September 1980 and the Metric Data Assembly software transfer by 7 July 1980.

III. Ground Communications Facility and Network Operations and Control Center Configuration

The GCF-NOCC configuration for Block I, Phase I VLBI is shown in Fig. 2. The Ground Communication Facility remained relatively unchanged except for adding a Data Records Processor and software in order to create a real-time Intermediate Data Record. This Real-Time IDR was not of itself a Block I VLBI requirement, but was necessary for timely creation of Telemetry IDR's. In order to provide real-time visibility into the DSS Operations for Block I VLBI, a Network Radio Science Real-Time Monitor (NRS RTM) and Software were added to the Network Data Processing Area of the NOCC. The NRS RTM monitors the configuration and status of the Deep Space Stations in real-time during the Block I VLBI data acquisition phases. The monitor data are displayed via the Network Display Subsystem in the Network Operations Control Area. Selected monitor data are also backfed to the participating Deep Space Stations for onsite monitoring.

A Block I VLBI predicts program was added to the Network Support Subsystem in order to generate and transmit to the DSSs the predicted angle and source time for the scheduled Block I VLBI passes.

IV. Correlation and Postcorrelation

Correlation and postcorrelation processing of the data received from the participating DSSs is carried out by a program developed and implemented on a general-purpose computer. The products of this processing are clock offset, UT1, polar motion, and station location parameters.

V. Operations Training

Since Block I VLBI operations are not an everyday occurrence (they are scheduled once a week on each baseline), training for the network was a prime implementation consideration. In order to enhance the proficiency for Block I VLBI operations, training packages for VLBI operation were specifically designed and implemented.

The training packages were implemented in two parts. The first part dealt with an overview of VLBI: the purpose, the data type and the Block I system. The second part dealt with the various subsystems involved and with specific subsystem operations and data flow.

During the March, April, May 1980 time frame (DSS 14 downtime), weekly VLBI training passes were conducted on the DSS 43-DSS 63 baseline. These passes were used specifically to maintain proficiency in the network and to train the network controllers in VLBI operation.

Single baseline passes were scheduled on the DSS 14, DSS 43 baseline and on the DSS 14-DSS 63 baseline during the last three weeks of May and the first week in June to reestablish and verify the proficiency at DSS 14 after its downtime.

VI. System Testing

Commencing the first week in June 1980, dual baseline passes (DSS 14-DSS 63, DSS 14-DSS 43) were scheduled weekly. The goal of these system tests is to demonstrate the ability of the network to reliably conduct the Block I VLBI passes and provide the required data results in a timely manner. The system test will be completed 7 July 1980, at which time the Block I Phase I VLBI System will be transferred to DSN Operations.

VII. Summary

The Block I, Phase I VLBI System will be operational to support Voyager project navigation requirements. The system will provide, on a weekly basis, the information related to station clock synchronization, UT1 and polar motion.

Reference

1. Chaney, W.D., and Ham, N.C., "DSN VLBI System MK 1-80," in *The Deep Space Network Progress Report 42-56*, pp. 26-34, Jet Propulsion Laboratory, Pasadena, Calif., April 15, 1980.
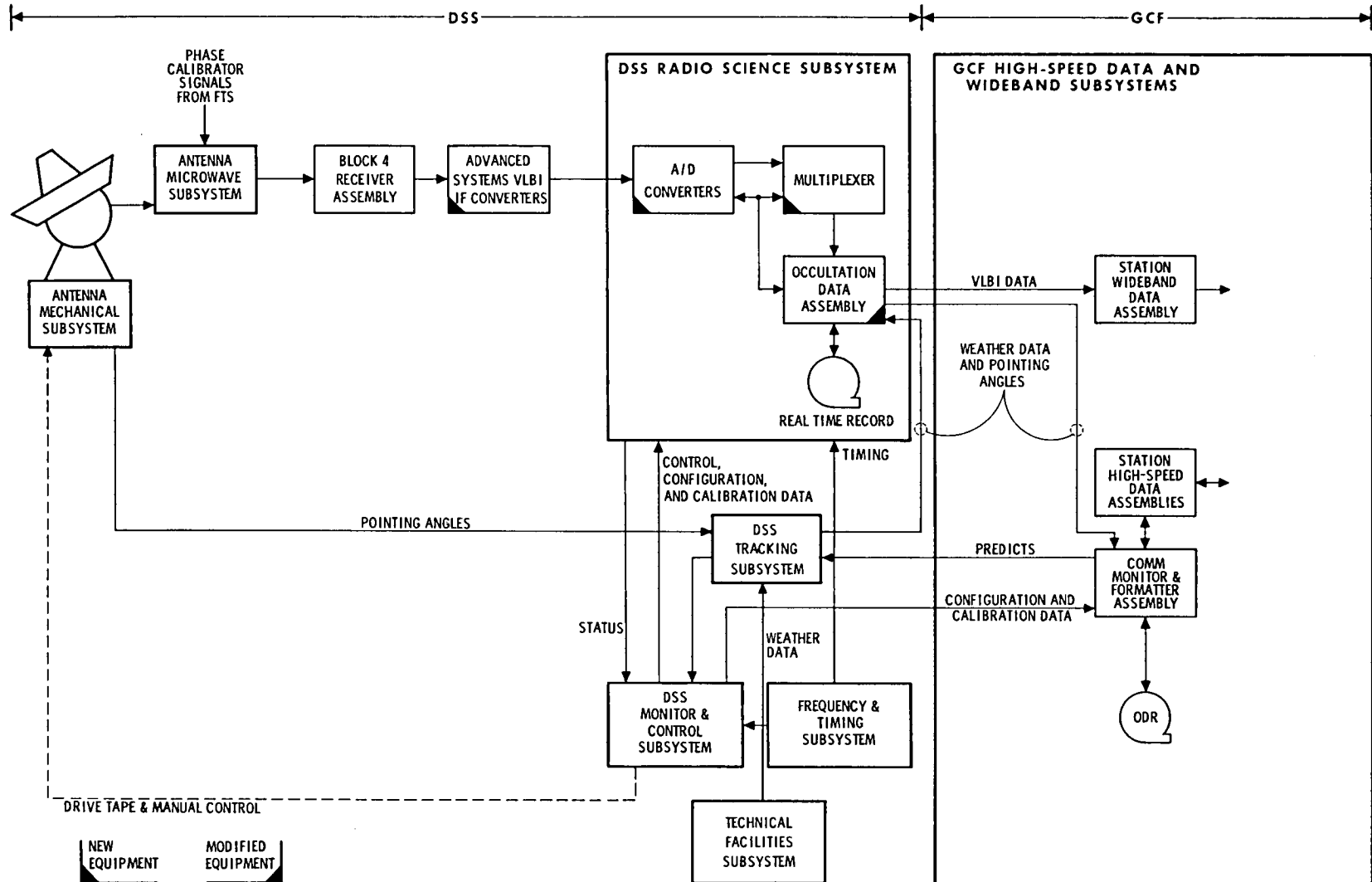
Fig. 1. Deep Space Station block diagram, Block 1, Phase 1
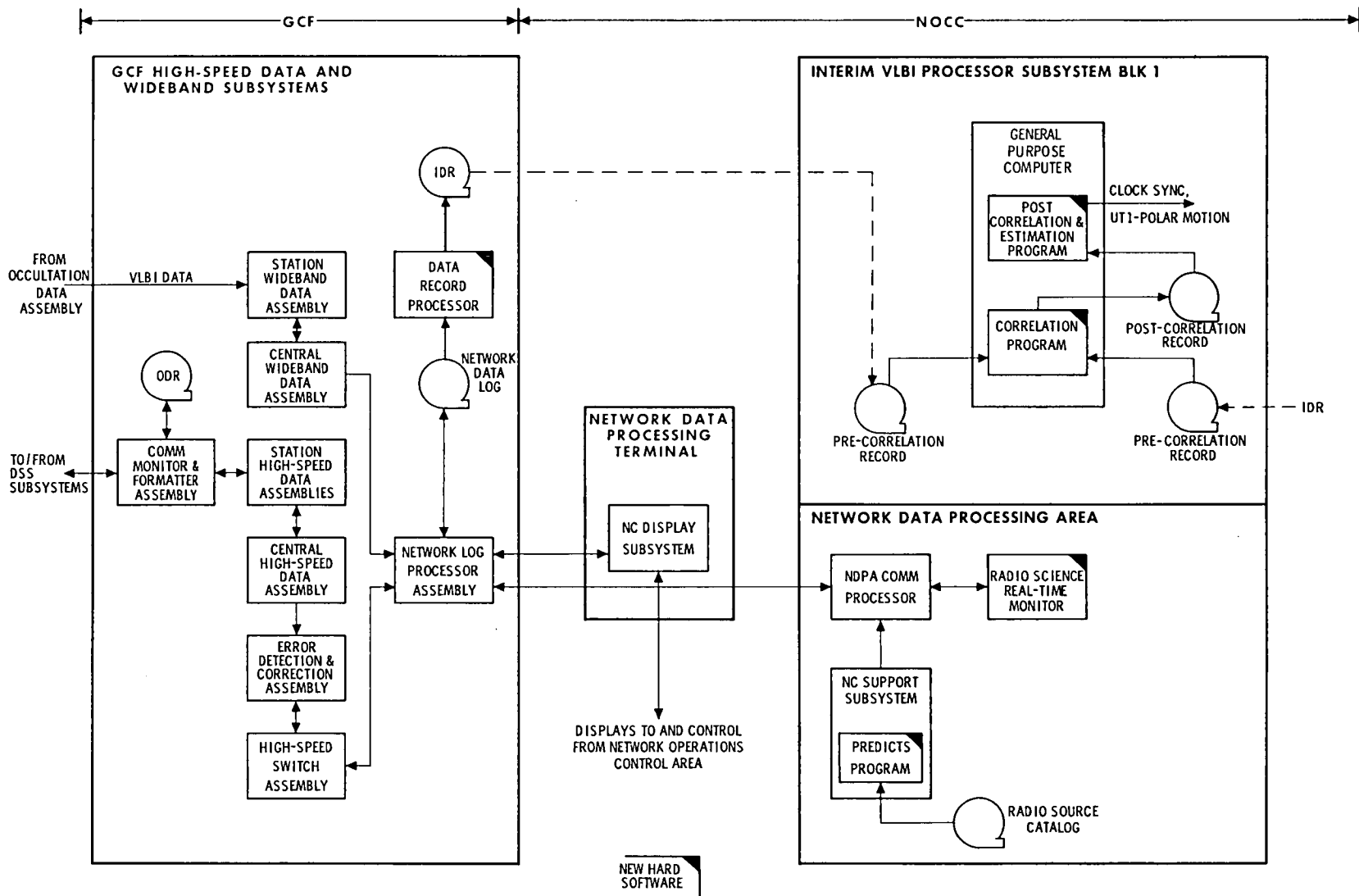
Fig. 2. GCF-NOCC block diagram, Block 1, Phase 1

Network Functions and Facilities

N. A. Renzetti

Office of Tracking and Data Acquisition

The objectives, functions, and organization of the Deep Space Network are summarized; deep space station, ground communication, and network operations control capabilities are described.

The Deep Space Network was established by the National Aeronautics and Space Administration (NASA) Office of Space Tracking and Data Systems and is under the system management and technical direction of the Jet Propulsion Laboratory (JPL). The network is designed for two-way communications with unmanned spacecraft traveling approximately 16,000 km (10,000 miles) from Earth to the farthest planets and to the edge of our solar system. It has provided tracking and data acquisition support for the following NASA deep space exploration projects: Ranger, Surveyor, Mariner Venus 1962, Mariner Mars 1964, Mariner Venus 1967, Mariner Mars 1969, Mariner Mars 1971, and Mariner Venus-Mercury 1973, for which JPL has been responsible for the project management, the development of the spacecraft, and the conduct of mission operations; Lunar Orbiter, for which the Langley Research Center carried out the project management, spacecraft development, and conduct of mission operations; Pioneer, for which Ames Research Center carried out the

project management, spacecraft development, and conduct of mission operations; and Apollo, for which the Lyndon B. Johnson Space Center was the project center and the Deep Space Network supplemented the Manned Space Flight Network, which was managed by the Goddard Space Flight Center. The network is currently providing tracking and data acquisition support for Helios, a joint U.S./West German project; Viking, for which Langley Research Center provided the Lander spacecraft and project management until May, 1978, at which time project management and mission operations were transferred to JPL, and for which JPL provided the Orbiter spacecraft; Voyager, for which JPL provides project management, spacecraft development, and is conducting mission operations; and Pioneers, for which the Ames Research Center provides project management, spacecraft development, and conduct of mission operations. The network is adding new capability to meet the requirements of the Galileo mission to Jupiter, for which JPL is providing the Orbiter spacecraft, and

the Ames Research Center the probe. In addition, JPL will carry out the project management and the conduct of mission operations.

The Deep Space Network (DSN) is one of two NASA networks. The other, the Spaceflight Tracking and Data Network (STDN), is under the system management and technical direction of the Goddard Space Flight Center (GSFC). Its function is to support manned and unmanned Earth-orbiting satellites. The Deep Space Network supports lunar, planetary, and interplanetary flight projects.

From its inception, NASA has had the objective of conducting scientific investigations throughout the solar system. It was recognized that in order to meet this objective, significant supporting research and advanced technology development must be conducted in order to provide deep space telecommunications for science data return in a cost effective manner. Therefore, the Network is continually evolved to keep pace with the state of the art of telecommunications and data handling. It was also recognized early that close coordination would be needed between the requirements of the flight projects for data return and the capabilities needed in the Network. This close collaboration was effected by the appointment of a Tracking and Data Systems Manager as part of the flight project team from the initiation of the project to the end of the mission. By this process, requirements were identified early enough to provide funding and implementation in time for use by the flight project in its flight phase.

As of July 1972, NASA undertook a change in the interface between the Network and the flight projects. Prior to that time, since 1 January 1964, in addition to consisting of the Deep Space Stations and the Ground Communications Facility, the Network had also included the mission control and computing facilities and provided the equipment in the mission support areas for the conduct of mission operations. The latter facilities were housed in a building at JPL known as the Space Flight Operations Facility (SFOF). The interface change was to accommodate a hardware interface between the support of the network operations control functions and those of the mission control and computing functions. This resulted in the flight projects assuming the cognizance of the large general-purpose digital computers which were used for both network processing and mission data processing. They also assumed cognizance of all of the equipment in the flight operations facility for display and communications necessary for the conduct of mission operations. The Network then undertook the development of hardware and computer software necessary to do its network operations control and monitor functions in separate computers. A characteristic of the new interface is that the Network provides direct data flow to and from the stations; namely, metric data, science and engineering telemetry, and such network monitor data as are useful to the flight project. This is done via appropriate ground communication equipment to mission operations centers, wherever they may be.

The principal deliveries to the users of the Network are carried out by data system configurations as follows:

(1) The DSN Tracking System generates radio metric data, i.e., angles, one- and two-way doppler and range, and transmits raw data to Mission Control.

(2) The DSN Telemetry System receives, decodes, records, and retransmits engineering and scientific data generated in the spacecraft to Mission Control.

(3) The DSN Command System accepts spacecraft commands from Mission Control and transmits the commands via the Ground Communications Facility to a Deep Space Station. The commands are then radiated to the spacecraft in order to initiate spacecraft functions in flight.

(4) The DSN Radio Science System generates radio science data, i.e., the frequency and amplitude of spacecraft transmitted signals affected by passage through media such as the solar corona, planetary atmospheres, and planetary rings, and transmits these data to Mission Control.

(5) The DSN Very Long Baseline Interferometry System generates time and frequency data to synchronize the clocks among the three Deep Space Communications complexes. It will generate universal time and polar motion and relative Deep Space Station locations as by-products of the primary data delivery function.

The data system configurations supporting testing, training, and network operations control functions are as follows:

(1) The DSN Monitor and Control System instruments, transmits, records, and displays those parameters of the DSN necessary to verify configuration and validate the Network. It provides the tools necessary for Network Operations personnel to control and monitor the Network and interface with flight project mission control personnel.

(2) The DSN Test and Training System generates and controls simulated data to support development, test, training and fault isolation within the DSN. It participates in mission simulation with flight projects.

The capabilities needed to carry out the above functions have evolved in the following technical areas:

(1) The Deep Space Stations, which are distributed around Earth and which, prior to 1964, formed part of the Deep Space Instrumentation Facility. The technology involved in equipping these stations is strongly related to the state of the art of telecommunications and flight-ground design considerations, and is almost completely multimission in character.

(2) The Ground Communications Facility provides the capability required for the transmission, reception, and monitoring of Earth-based, point-to-point communications between the stations and the Network Operations Control Center at JPL, Pasadena, and to the JPL Mission Operations Centers. Four communications disciplines are provided: teletype, voice, high-speed, and wideband. The Ground Communications Facility uses the capabilities provided by common carriers throughout the world, engineered into an integrated system by Goddard Space Flight Center, and controlled from the communications Center located in the Space Flight Operations Facility (Building 230) at JPL.

The Network Operations Control Center is the functional entity for centralized operational control of the Network and interfaces with the users. It has two separable functional elements; namely, Network Operations Control and Network Data Processing. The functions of the Network Operations Control are:

(1) Control and coordination of Network support to meet commitments to Network users.

(2) Utilization of the Network data processing computing capability to generate all standards and limits required for Network operations.

(3) Utilization of Network data processing computing capability to analyze and validate the performance of all Network systems.

The personnel who carry out the above functions are located in the Space Flight Operations Facility, where mission operations functions are carried out by certain flight projects. Network personnel are directed by an Operations Control Chief. The functions of the Network Data Processing are:

(1) Processing of data used by Network Operations Control for control and analysis of the Network.

(2) Display in the Network Operations Control Area of data processed in the Network Data Processing Area.

(3) Interface with communications circuits for input to and output from the Network Data Processing Area.

(4) Data logging and production of the intermediate data records.

The personnel who carry out these functions are located approximately 200 meters from the Space Flight Operations Facility. The equipment consists of minicomputers for real-time data system monitoring, two XDS Sigma 5s, display, magnetic tape recorders, and appropriate interface equipment with the ground data communications.

DSN Monitor and Control System, Mark III-80

J. G. Leflang
TDA Engineering Office

A description of the DSN Monitor and Control System, Mark III-80 is presented. The major implementations required to evolve from the Mark III-78 to the Mark III-80 configuration are identified.

I. Introduction

The DSN Monitor and Control System, Mark III-80, is a multimission system utilized by the DSN to support Pioneer 6-11, Helios, Viking, Pioneer Venus, and Voyager missions. Figure 1 provides a block diagram of the DSN Monitor and Control System, Mark III-80 configuration.

Since 1978, implementation of equipment and software changes within the DSN facilities has resulted in enhanced capability within the DSN Monitor and Control System. The affected facilities are the Deep Space Stations and the Network Operations Control Center.

At the Deep Space Stations (DSS) a Stand-Alone Host Processor is being implemented. Included are software ("host" software) changes which provide downline loading to the Stand-Alone Host Processor from a disc unit of any idle data system computer.

At Deep Space Stations with a 34-m antenna, the Microwave Subsystem has been provided with an interface which allows remote configuration selection at the central monitor and control operator's position.

In the NOCC, software changes have been implemented to provide precision power monitor and GCF monitor displays for use by the Network Operations Control Team.

II. Deep Space Station

As part of the DSN Monitor and Control System, the DSS Monitor and Control Subsystem (DMC) provides two primary functions: (1) The DMC provides the central control and monitor capability for the DSS, and (2) the DMC receives control data from and furnishes monitor data to the NOCC for Network Central Control and Monitor purposes.

There are four major assemblies of the DMC that accomplish the above functions. The four major assemblies are:

(1) Digital Instrumentation Assembly.

(2) Stand-Alone Host Processor.

(3) Station Monitor and Control Console.

(4) Data System Terminal.

A. Digital Instrumentation Assembly (DIS)

The DIS, (an XDS 920 computer) is utilized as a central collection point for station monitor data and for interfacing with the NOCC. For collecting station monitor data, the DIS has interfaces with all of the station subsystems. The station monitor data are accumulated by the DIS and displayed to the station operator located at the Station Monitor and Control Console. Additionally, a subset of this station monitor data is sent to the NOCC for central monitoring purposes.

B. Stand-Alone Host Processor Assembly (SHP)

An SHP, which consists mainly of the Modcomp 7810 classic computer, is being installed in the DIS Monitor Interface Assembly (DMI) cabinet at all Deep Space Stations for the Mark III-80 configuration. Previously, the host software operated concurrently with the communications program in the Communications Monitor and Formatter Assembly (CMF). The SHP is being implemented to remove constraints which arise from the use of the CMF to support data recalls and system performance tests. The SHP provides the interface for centralized operation of DSS data system computers.

The SHP operational program is downline loaded using a disc drive of an idle data system computer (either the Command Processor Assembly, Metric Data Assembly, Communications Monitor and Formatter Assembly or Telemetry Processor Assembly). The SHP is interfaced to the data system computers via a Star Switch Controller (SSC) and operates in an unattended manner in conjunction with the Data System Terminal.

Changes to the host software occurred to provide loading of the operational program in the SHP, but the operator interface has not been changed. The software is currently undergoing soak testing prior to DSN operations acceptance.

C. Station Monitor and Control Console (SMC IIA, SMC IIB)

The SMC IIA and SMC IIB were implemented as part of the Mark III-78 System configuration for the purpose of providing a central monitor and control operator's position for some of the noncomputerized subsystems. Two different configurations, designated SMC IIA for the 64-m DSS and SMC IIB for all others, were developed for the DSN.

D. Data System Terminal Assembly (DST)

The DST is used as a central DSS input-output device for computers in the Command, Telemetry, Tracking, and Radio Science Subsystems, and for the Communications Monitor Formatter at the DSS. It consists of four elements: two keyboard-CRTs, a hardcopy printer, and "host" software capability. The keyboard-CRTs and printers interface with the host software, and the host software then interfaces with all of the data system computers via the star switch controller. In this manner, the data system computers can be centrally controlled and monitored. The DST and the Station Monitor and Control console are collocated within the DSS control room and form a centralized operator position for monitor and control.

III. Network Operations Control Center (NOCC)

The NOCC Monitor and Control Subsystem provides the processing capability for central network monitor and control. Software changes have occurred to provide monitoring of the signal level and noise temperature parameters from the Precision Power Monitor Assembly (part of the Receiver/Exciter Subsystem at the DSS). Signal and noise measurement data are returned to the NOCC to enable system level monitoring of baseband combining of the signal received by two Deep Space Stations. Other software changes have been implemented to provide readouts of the GCF Monitor data (line performance and status) at the NOCC Displays.

NETWORK OPERATIONS CONTROL CENTER — GROUND COMMUNICATIONS FACILITY — DEEP SPACE STATION

DSS SUBSYSTEMS

TELEMETRY (2)

COMMAND (2)

TRACKING

RADIO SCIENCE

STAR SWITCH CONTROLLER (2)

MONITOR AND CONTROL

STAND-ALONE HOST PROCESSOR

DATA SYSTEM TERMINAL

DIGITAL INSTRUMENTATION ASSEMBLY

STATION MONITOR AND CONTROL CONSOLE

NON-COMPUTERIZED SUBSYSTEMS

RECEIVER-EXCITER

MICROWAVE

ANTENNA MECHANICAL

FREQUENCY AND TIMING

TRANSMITTER

NOCC SUBSYSTEMS

DISPLAY

MONITOR AND CONTROL

TELEMETRY (3)

TRACKING (2)

TEST AND TRAINING (2)

SUPPORT (2)

COMMAND

SPARE

STAR SWITCH CONTROLLER (3)

NOCC COMMUNICATIONS SUBSYSTEM

NCE

HIGH-SPEED DATA SUBSYSTEM

ERROR CORRECTION AND SWITCH ASSEMBLY

CMF

CENTRAL COMMUNICATIONS MONITOR

GCF SUBSYSTEMS
WIDEBAND
VOICE
TELETYPE

NCE - NOCC COMMUNICATION EQUIPMENT

CMF - COMMUNICATIONS MONITOR FORMATTER

DSN MONITOR AND CONTROL MAJOR ELEMENTS

Fig. 1. DSN Monitor and control Subsystem Mark III-80

Pioneers 10 Through 12 Support

R. E. Nevarez

Deep Space Network Operations Section

This article reports on the activities of DSN Operations in support of the Pioneer 10 and 11 and Pioneer 12 (Pioneer-Venus) Missions from 16 December 1979 through 31 May 1980.

I. Introduction

The information contained in this article covers the cruise phases of Pioneer 10, Pioneer 11, and Pioneer 12 orbital operations and the continuing efforts of the Deep Space Network in support of Pioneer Mission Operations.

II. Mission Operations and Status

A. Pioneer 10

This spacecraft each day continues to set distance records. As of this report it has achieved a distance of 20 AU, which relative to Earth puts it at a distance of 6,811,500,000 kilometers on its course out of the solar system. The data being received from the spacecraft continues to indicate all onboard systems are functioning nominally.

B. Pioneer 11

The Pioneer-11 onboard systems continue to function nominally. The spacecraft continues on its course out of the solar system in the opposite direction of its sister spaceship (Pioneer 10). At present Pioneer 11 is at a distance relative to Earth of 2,760,600,000 kilometers.

C. Pioneer 12

The Pioneer-12 Venus Orbiter continues in a healthy state. Data received from the spacecraft indicates that all of its onboard systems are functioning nominally. Since the last occultation cycle in December 1979, there has been no occultation activity.

III. Special Activities

The Deep Space Network Compatibility Test Area (CTA-21) continues to support Pioneer Project command software development and command operator training.

IV. Summary

At this time, Pioneer 10, 11, and 12 spacecraft appear to be operating nominally. Pioneers 10 and 11 are in cruise mode and Pioneer 12 continues Venus orbital operations. Tracking coverage from November 1979 through May 1980 is shown in Table 1.

Table 1. Pioneers 10 through 12 tracking coverage

Month	Pioneer spacecraft	Station type	Number of tracks	Tracking time (hrs/mins)
November	10	34 m	11	62:31
1979		64 m	36	241:29
	11	26 m	28	205:09
		34 m	1	3:30
		64 m	6	37:57
	12	26 m	50	283:32
		34 m	1	3:30
		64 m	68	482:24
December	10	34 m	1	4:15
1979		64 m	49	313:15
	11	26 m	28	219:49
		34 m	3	26:03
		64 m	19	151:42
	12	26 m	53	405:32
		34 m	4	27:16
		64 m	42	362:36
January	10	64 m	41	312:14
1980	11	26 m	30	271:08
		64 m	18	137:51
	12	26 m	43	351:07
		34 m	2	9:30
		64 m	58	405:41
February	10	64 m	36	233:00
1980	11	26 m	28	191:09
		64 m	23	149:51
	12	26 m	60	528:13
		34 m	4	25:45
		64 m	33	190:36
March	10	26 m	4	5:25
1980		34 m	6	17:19
		64 m	38	217:52
	11	26 m	31	210:46
		34 m	4	21:10
		64 m	19	139:13
	12	26 m	80	588:29
		34 m	4	28:26
		64 m	48	197:11
April	10	26 m	3	7:17
1980		34 m	3	5:19
		64 m	37	140:16
	11	26 m	35	250:04
		34 m	3	25:45
		64 m	18	120:44
	12	26 m	71	546:15
		34 m	21	129:44
		64 m	18	92:27
May	10	34 m	3	8:29
1980		64 m	36	246:05
	11	26 m	40	290:36
		34 m	2	14:42
		64 m	9	64:28
	12	26 m	76	611:33
		34 m	21	111:25
		64 m	8	57:04

Pioneers 6 Through 9 Support

R. E. Nevarez

Deep Space Network Operations Section

This article reports on the activities of DSN Operations in support of the Pioneer 6 through 9 Missions from 16 December 1979 through 31 May 1980.

I. Introduction

The information contained in this article covers the cruise phases of Pioneer 6 through 9 operations and the continuing efforts of the Deep Space Network in support of Pioneer Mission Operations.

II. Mission Operations and Status

A. Pioneer 6

Pioneer 6 was not tracked during the month of December. On 18 January 1980 almost a year to the day since the last Pioneer-6 support, the spacecraft was supported by DSS 43 (Ballima, Australia). During this support no downlink from the spacecraft could be found. After an extensive study it was determined that possibly the spacecraft had turned off due to an undervoltage condition. The decision was made to attempt to turn the spacecraft back on by transmitting a sequence of commands in the blind, utilizing the high power transmitter at DSS 43. On 15 February 1980 a downlink was acquired from the Pioneer-6 spacecraft. Again on 21 February a downlink was acquired from the spacecraft. However, on both days the signal was weak, as the spacecraft was entering superior conjunction. Because the data obtained was not of good quality, it is difficult to determine the true status of the spacecraft.

B. Pioneers 7 through 9

During the month of December there were no scheduled tracks for these spacecraft. In January 1980 scheduled tracking support commenced on a regular basis. Data received from all three spacecraft indicate that they are healthy and functioning nominally. Pioneer 8 continues to require the 100 kW transmitter from 64-m stations due to the spacecraft's degraded receiver.

III. Summary

At this time, Pioneer 6 through 9 are in cruise mode and spacecraft appear to be operating nominally. Tracking coverage from November 1979 through May 1980 is shown in Table 1.

Table 1. Pioneers 6 through 9 tracking coverage

Month	Pioneer Spacecraft	Station type	Number of tracks	Tracking time (hrs, mins)
January	6	64 m	1	00:46
1980	7	64 m	1	03:45
	8	64 m	4	11:36
	9	64 m	1	03:05
February	6	64 m	3	10:30
1980	7	64 m	2	5:57
	8	64 m	3	9:17
	9	64 m	3	12:08
March	6	64 m	1	6:20
1980	7	64 m	1	5:42
	8	64 m	4	19:00
	9	64 m	4	14:54
April	7	64 m	1	5:30
1980	8	64 m	2	10:52
	9	64 m	5	26:33
May	8	64 m	1	3:57
1980	9	64 m	6	41:11

Automated Frequency Standard Stability Data Reduction

L. J. Knapp

Communications Systems Research Section

This article describes a design using a medium-sized computer, a fiber optic communication link, and a desk top computer to reduce data collected at a remote site for analysis of frequency standard tests.

I. Introduction

In the past, the reduction of data acquired at the Interim Frequency Standards Test Facility was performed by hand. However, increased testing of frequency standards resulted in the need for a faster method of data reduction. With this need in mind a design was initiated that would allow data input to the Xerox Sigma V computer to be analyzed (by a program developed as a part of this effort), then transmitted via a fiber optic link to a desk top computer, where the results could be plotted automatically on a printer/plotter.

II. Description

Data generated at the Interim Frequency Standards Test Facility is collected on magnetic tape, which is then transported to the Xerox Sigma V computer. An Allan Variance (two sample variance) is then calculated. The Allan Variance (sigma vs tau) is then written to a data file in the Sigma V.

A fiber optic communication link between the Sigma V and a desk top computer (located in a remote laboratory) was designed to transmit data in the Sigma V file to the desk top computer. The fiber optic link consists of a module to house the power supply for the fiber optic link as well as the wiring for data transfer (Figs. 1 and 2). The fiber optic link (a standard RS232 full duplex link) operates at data rates of up to 100k baud over a distance of 200 meters.

A program was written for the desk top computer that will automatically access the data file in the Sigma V, process the data and provide a data plot (Fig. 3). An overall block diagram of this system is shown in Fig. 4.

III. Conclusion

The Automated Data Reduction System is now operating and has improved data reduction by a factor of 10 over the hand method. An example of a typical data output is shown in Fig. 5. A fiber optic link has been installed between the Mesa and the Timing and Frequency Systems and Research Laboratory at JPL. This link will be connected to the Interim Frequency Standards Test Facility and the desk top computer in the laboratory where the Allan Variance computation will be performed and the data plotted in real-time, eliminating the need for magnetic tape transports and the use of the Sigma V computer.
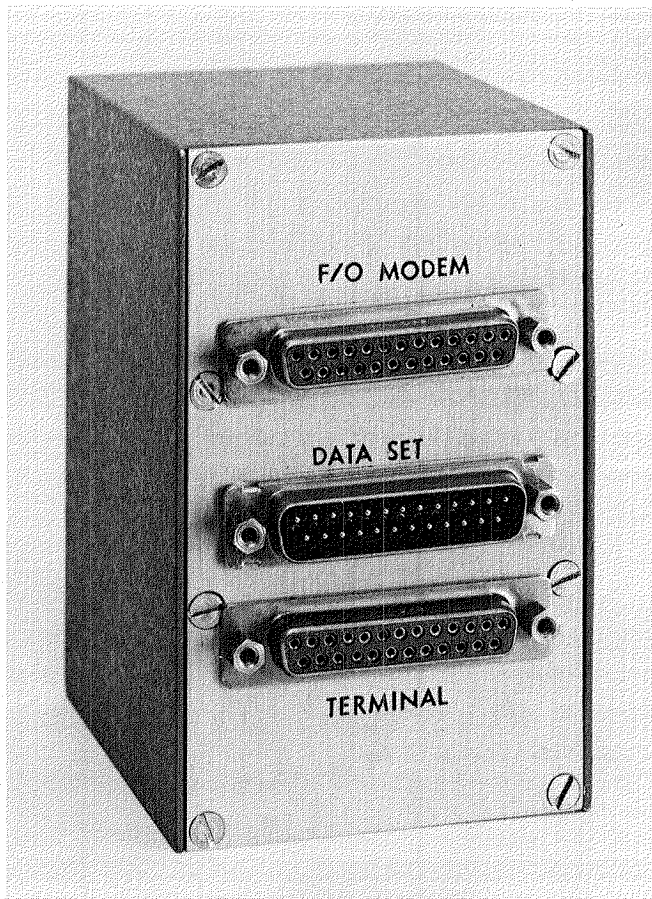
Fig. 1. Fiber optic-RS232 interface module
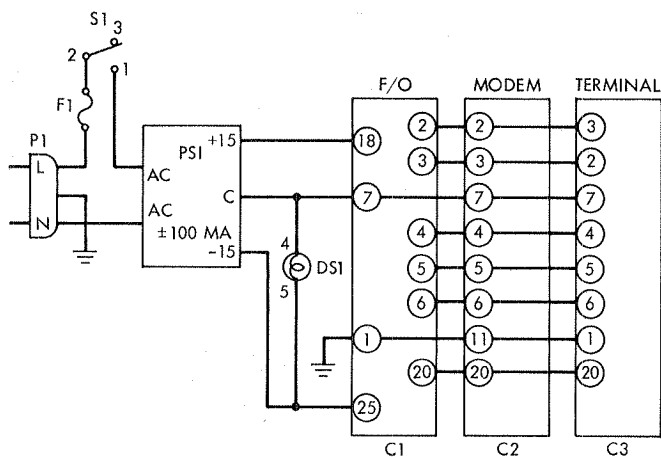
Fig. 2. Fiber optic-RS232 interface schematic
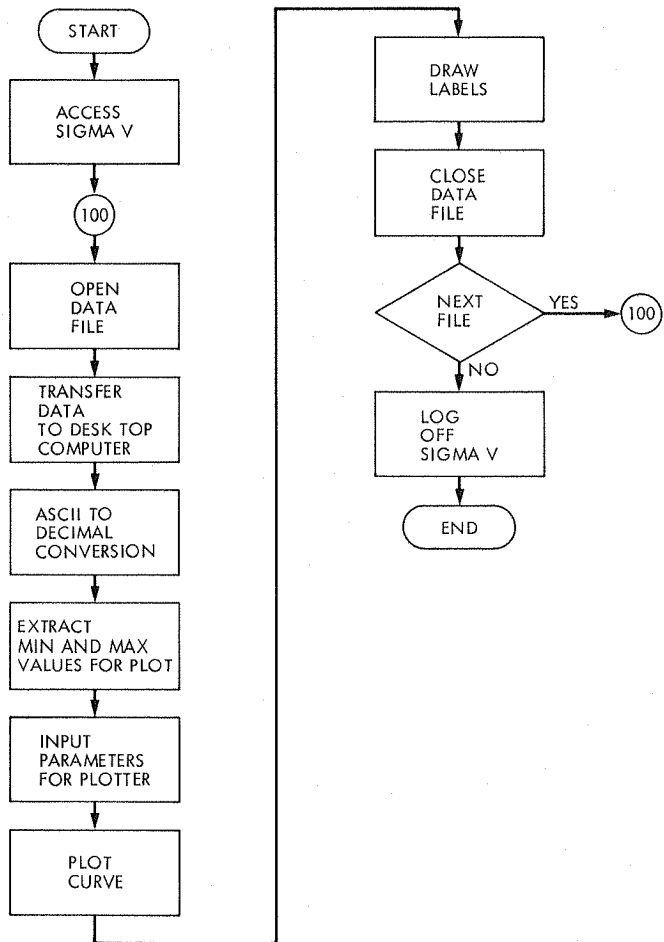
Fig. 3. Program flowchart for data transfer and manipulation
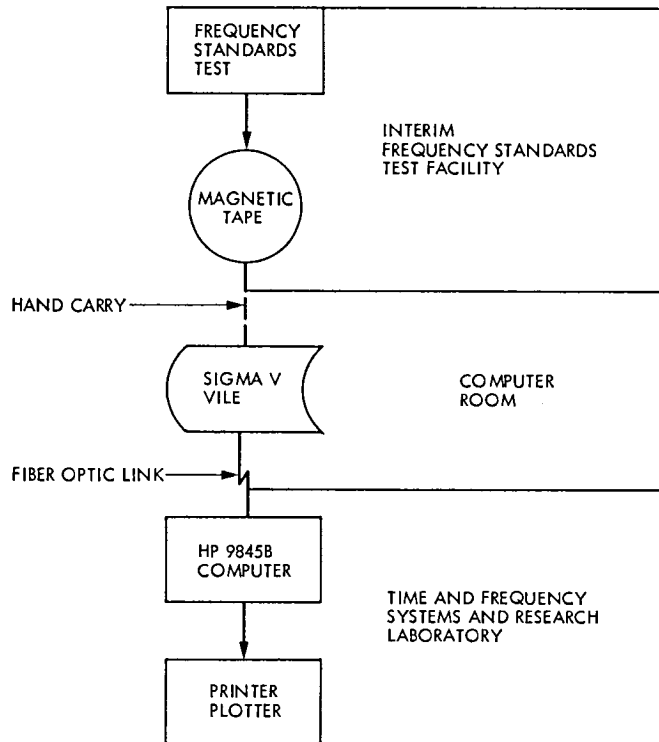
Fig. 4. Allan Variance data flow
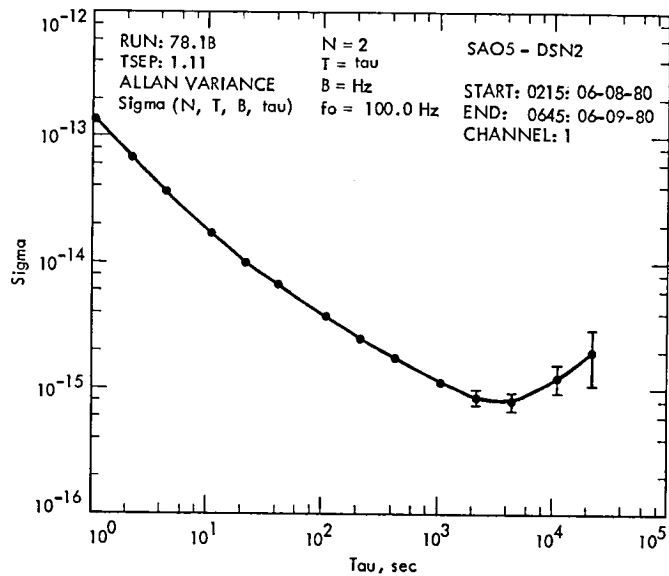
Fig. 5. Typical Allan Variance plot, sigma vs tau

Signal-to-Noise Ratio Calculation for Fiber Optics Links

K. Y. Lau

Communications Systems Research Section

In this article, the signal-to-noise ratio (SNR) effect upon the maximum transmission length of a fiberoptic system is discussed. The relationships of different system parameters are discussed. A general formula to obtain the SNR of a single mode fiberoptic system is derived.

Using the specification of a commercial avalanche photo decode, the SNR is estimated to be 5×10^{12} $m^2/\Delta\nu$ for $L \leqslant 30$ km and

$$1.1 \times \frac{10^{19} \; m^2 10^{-\alpha L/5}}{\Delta\nu}$$

for $L > 30$ km. The main bandwidth limitating factor in multimode fiberoptic systems is found to be intermodal dispersion.

It is concluded that for frequency standard transmission a respectable SNR can be obtained for different fiber optic systems, providing that we are operating within the bandwidth of the fiber.

I. Introduction

In this article, we would like to answer the following question: Given a certain signal-to-noise ratio (SNR), what is the maximum transmission length of an optical fiber system used primarily for frequency and time synchronization? In Section II, we describe the system under consideration. The SNR for single mode optical fiber systems is derived in Section III and estimated numerically in Section IV. In Section V, the SNR for multi-mode fiber links is derived and compared with single-mode fiber links.

II. The System

Let us consider the fiber optics link sketched in Fig. 1. The laser diode oscillates at a single optical frequency ω, and the light output is modulated by the signal source, which is a high precision frequency standard. The optical fiber has a loss of an α dB/km, is L km long, and we assume that the signal baseband lies well within the bandwidth of the fiber (which can be as high as hundreds of GHz-km for single mode fibers). The detector used is assumed to be an avalanche photodiode (APD) followed by a phase-locked amplifier. The output is

delivered into a 50 Ω load. We further assume that the baseband signal is within the detection bandwidth of the APD.

We assume that the modulated light output from the laser diode is purely sinusoidal at baseband frequency Ω, with a modulation depth m. The optical power fed into the fiber is then

$$P_{in}(t) = P(1 + m \cos \Omega t) + S(t) \qquad (1)$$

where P is the average optical power. $S(t)$ is the noise generated by the laser. The magnitude and spectral characteristic of this noise are quite complicated, and have been investigated by several authors (Refs. 1 and 2). It has the properties of a shot-noise-driven resonant tuned circuit. Figure 2 illustrates the spectral properties of the laser noise at different average output optical powers, P. Above lasing threshold, the output power abruptly increases while the relative noise power $\langle S^2 \rangle / P$ abruptly decreases. ($\langle \ \rangle$ denotes time average of a quantity.) Figure 3 illustrates the relative noise power density at low frequencies (< 1 GHz) vs the average output power P. However, as observed from Fig. 2, the noise power density shows a spike in the frequency range around 2-4 GHz, which can be orders of magnitude higher than in the "midband" range ($\sim 0-1$ GHz). This noise spike is related to the relaxation oscillation of the laser diode. In addition to the unusually intense noise in this region, there are other undesirable effects, such as high harmonic distortion. Therefore, it is recommended that our baseband signal be below the frequency at which the noise spike appears in the laser diode response, and we shall confine our analysis similarly.

Propagation of the signal in Eq. (1) through a fiber of length L attenuates its power by a factor of $10^{-\alpha L/10}$, and hence the output optical power is

$$P_{out}(t) = 10^{-\alpha L/10} P_{in}(t) \qquad (2)$$

The current generated by the APD is proportional to the incident optical power (lumping splicing and insertion losses into the attenuation term) and is given by

$$i(t) = \frac{Ge\eta}{\hbar\omega} P_{out}(t) \qquad (3)$$

where G and η are respectively the avalanche gain and the internal quantum efficiency of the APD, $\hbar$ is the Planck's

constant, ω is the optical frequency, and e is the electronic charge. Using Eq. (2) we have

$$i(t) = \frac{GPe\eta}{\hbar\omega}(1 + m \cos \Omega t)10^{-\alpha L/10}$$

$$+ \frac{GeP_B\eta}{\hbar\omega} + i_d \qquad (4)$$

$$+ \frac{Ge\eta}{\hbar\omega} S(t)10^{-\alpha L/10}$$

where the dark current of the APD (i_d) and the background light entering the APD P_B is included. This current is then amplified by the phase-lock amplifier. We assume the phase-lock amplifier has bandwidth $\Delta\nu$ and has gain G_A.

III. Derivation of the SNR

The noise in the detection system arises from four sources: the dark current and laser source noise as in Eq. (4), plus shot noise and thermal noise (Ref. 3).

(1) The shot noise current has a mean square value of

$$\overline{i^2_{N_{shot}}} = 2e\bar{I}\Delta\nu \qquad (5)$$

where $\bar{I}$ is the average amplified current from Eq. (4),

$$\bar{I} = \frac{G_A Ge\eta}{\hbar\omega}(P \times 10^{-\alpha L/10} + P_B) + G_A i_d \qquad (6)$$

(2) The thermal noise current has a mean square value given by

$$\overline{i^2_{N_{thermal}}} = G_A^2 \frac{kT}{R_L} \Delta\nu \qquad (7)$$

where R_L is the load resistance = 50 Ω, k is the Boltzmann constant, G_A is the amplifier current gain, and T is the temperature of the system (including the equivalent noise temperature of the amplifier).

(3) The laser source noise $S(t)$ is attenuated in passing through the fiber, and generates a mean square noise current in the APD equal to

$$\overline{i^2_{N_{laser}}} = \left(\frac{Ge\eta}{\hbar\omega}\right)^2 \langle S^2 \rangle 10^{-\alpha L/5} \Delta\nu \qquad (8)$$

The total noise power is thus

$$\overline{i_{N_{shot}}^2} + \overline{i_{N_{thermal}}^2} + \overline{i_{N_{laser}}^2} =$$

$$2eG_A \left\{ \frac{Ge\eta}{\hbar\omega} (P \times 10^{-\alpha L/10} + P_B) + i_d \right\} \Delta\nu \quad (9)$$

$$+ G_A^2 \frac{kT}{R_L} \Delta\nu + \left(\frac{GG_A\eta}{\hbar\omega} \right)^2 \langle S^2 \rangle 10^{-\alpha L/5} \Delta\nu$$

The signal power, from Eq. (4), is:

$$\overline{i_S^2} = \frac{1}{2} \left(\frac{G_A GPe\eta}{\hbar\omega} m \right)^2 10^{-\alpha L/5} \quad (10)$$

The signal-to-noise ratio is then:

$$\frac{S}{N} = \frac{\dfrac{1}{2} \left(\dfrac{G_A GPe\eta}{\hbar\omega} m \right)^2 10^{-\alpha L/5}}{2eG_A \dfrac{Ge\eta}{\hbar\omega} (P \times 10^{-\alpha L/10} + P_B) \Delta\nu + 2e G_A i_d \Delta\nu + \dfrac{kTG_A^2}{R_L} \Delta\nu + \left(\dfrac{GG_A\eta}{\hbar\omega} \right)^2 \langle S^2 \rangle 10^{-\alpha L/5} \Delta\nu} \quad (11)$$

IV. Numerical Estimations

We shall estimate the contributions of the four terms in the denominator of Eq. (11), which are due to, respectively, shot, dark current, and thermal and laser noise.

Typical parameters for a silicon avalanche photodiode (RCA model C30902E) are:

$$\frac{eG\eta}{\hbar\omega} = \begin{array}{l} \text{65 amps/watt around the wavelength} \\ \text{of GaAs laser diodes,} \end{array}$$

$$i_d = \text{dark current} = 16 \text{ nA}$$

Typically, the power coupled from the laser diode into the optical fiber is approximately 1 mW. Assuming the background leakage light P_B to be zero, the shot noise contribution is

$$2e \frac{G_A Ge\eta}{\hbar\omega} P \times 10^{-\alpha L/10} \approx 2 \times 10^{-20} G_A \times 10^{-\alpha L/10} \text{ amp}^2/\text{Hz}$$

The dark current contribution is

$$2ei_d G_A \approx 5.1 \times 10^{-27} G_A \text{ amp}^2/\text{Hz}$$

Assuming an ambient temperature of 300 K, and the noise figure of the amplifier to be 2 dB, the thermal noise contribution is

$$G_A^2 \frac{kT}{R_L} \simeq 1.31 \times 10^{-22} G_A^2 \text{ amp}^2/\text{Hz}$$

Lastly, from Figs. 2 and 3, the laser noise power is, assuming an average optical output of 3 mW from the laser diode, approximately $\langle S^2 \rangle = 10^{-19}$ watt/Hz. The noise current at the detector due to laser noise is

$$\left(\frac{GG_A\eta}{\hbar\omega} \right)^2 \langle S^2 \rangle 10^{-\alpha L/5} \simeq$$

$$4.2 \times 10^{-16} \times 10^{-\alpha L/5} G_A^2 \text{ amp}^2/\text{Hz}$$

The signal power is

$$\frac{1}{2} \left(\frac{Ge\eta}{\hbar\omega} P m \right)^2 10^{-\alpha L/5} G_A^2 \simeq$$

$$2.1 \times 10^{-3} m^2 10^{-\alpha L/5} G_A^2 \text{ amp}^2$$

Thus, the signal-to-noise ratio is

$$\frac{S}{N} = \frac{A m^2 10^{-\alpha L/5} G_A}{(B 10^{-\alpha L/10} + C + G_A D + G_A E \times 10^{-\alpha L/5}) \Delta\nu} \quad (12)$$

where

$A = 2.1 \times 10^{-3}$ (signal)

$B = 2 \times 10^{-20}$ (shot noise)

$C = 5.1 \times 10^{-27}$ (dark current noise)

$D = 1.31 \times 10^{-22}$ (thermal noise)

$E = 4.2 \times 10^{-15}$ (laser noise)

Equation (12) is our principal result. In Fig. 4, we plot the contribution of the various noises vs the link length-attenuation product. If the attenuation is 1 dB/km, then the x-axis will be scaled in km. The amplifier gain G_A is assumed to be 100, and for a fiber loss of 1 dB/km, we see that laser noise dominates for $L \leqslant 30$ km, and that the signal-to-noise ratio is approximately constant.

$$\frac{S}{N} \simeq \frac{A\, m^2}{E\, \Delta\nu} \simeq 5 \times 10^{12}\, \frac{m^2}{\Delta\nu} \tag{13}$$

Beyond 30 km, we have

$$\frac{S}{N} \simeq \left(\frac{A}{D}\right) \frac{m^2\, 10^{-\alpha L/5}}{\Delta\nu} \simeq 1.1 \times 10^{19}\, \frac{m^2\, 10^{-\alpha L/5}}{\Delta\nu} \tag{14}$$

In Fig. 5, we plot SNR vs αL for $\Delta\nu = 10$ Hz. Thus, a respectable SNR can be maintained for a link length as long as 70 km with fibers of about 1 dB/km loss.

Since the bandwidth $\Delta\nu$ of the amplifier appears in the denominator of SNR, it follows that for wideband signal transmission of bandwidth B the SNR will be that shown in Fig. 5 minus $10 \log(B/10)$ dB (since we have assumed $\Delta\nu = 10$ Hz in Fig. 5).

V. SNR Calculation for Multimode Fibers

Our previous calculations have assumed that the baseband signal falls within the transmission bandwidth of the optical fiber. For single-mode fibers, the bandwidth-length product can be as high as 100 GHz-km (assuming a single mode laser source) while multimode fibers are commonly in the range of 1 GHz-km. For a 100 km link with a baseband signal of 500 MHz, say, the signal lies comfortably within the bandwidth of single mode fibers but not multimode fibers. In the following we include this effect and examine its consequences.

The bandwidth-limiting factor in multimode fibers is intermodal dispersion. Multimode fibers support a large number (several hundred) of *transverse* optical modes due to their relatively large size. These transverse modes, however, each carrying a sinusoidal baseband modulation, travel down the fiber at different group velocities. Hence, the received signal is a sum of sinusoids of different phases. The result is a lowering of the modulation depth as compared with that at the input (where each mode carries modulation with the same phase).

The amount of intermodal dispersion in a multimode fiber is usually specified in time-spread/km. When an optical impulse is fed into the fiber, the output can be approximated by a gaussian pulse with half-width increasing linearly with fiber length. (With strong mode-coupling and for sufficiently long fiber length, the gaussian width increases as the square root of distance instead of linearly — see Ref. 4.) A typical number for multimode fiber is approximately 1 ns/km. Thus, the impulse response of the fiber is

$$g(t) = e^{-t^2/L^2}/L\sqrt{\pi} \tag{15}$$

where t is measured in ns, and L is the total length of the fiber in km. The factor $L\sqrt{\pi}$ is required for power conservation.

The response of the fiber due to an arbitrary input is given by the convolution integral

$$P_{\text{out}}(t) = \int_{-\infty}^{\infty} P_{\text{in}}(t - \tau)\, g(\tau)\, d\tau \tag{16}$$

For a purely sinusoidal input with modulation depth m,

$$P_{\text{in}}(t) = P(1 + m \cos \Omega t)$$

and the output is

$$P_{\text{out}}(t) = \frac{P}{L\sqrt{\pi}} \int_{-\infty}^{\infty} (1 + m \cos \Omega\, (t - \tau)) e^{-\tau^2/L^2}\, d\tau$$

$$= P + \frac{mP}{L\sqrt{\pi}} Re \left(e^{i\Omega t} \int_{-\infty}^{\infty} e^{-i\Omega t} e^{-\tau^2/L^2}\, d\tau \right)$$

$$= P + \frac{mP}{L\sqrt{\pi}} Re \left(e^{i\Omega t} e^{-\left(\frac{L\Omega}{2}\right)^2} \int_{-\infty}^{\infty} e^{-\left(\frac{\tau}{L} - \frac{iL\Omega}{2}\right)^2}\, d\tau \right)$$

$$= P \left(1 + m e^{-\left(\frac{L\Omega}{2}\right)^2} \cos \Omega\, t \right) \tag{17}$$

Hence the modulation depth is reduced to an effective value

$$m' = me^{-(\Omega_L/2)^2} \qquad (18)$$

Since, according to Eq. (12), the signal-to-noise ratio is proportional to m^2, it follows that SNR decreases as $\exp(-(\Omega_L)^2/2)$. In Fig. 6, we plot SNR vs αL for various baseband modulation frequencies. The effect is drastic once the baseband falls outside the fiber bandwidth. As long as this is not the case, the difference between single mode and multimode fibers is minimal. For a 100 km link, this requirement is satisfied if the baseband frequency is less than several GHz for single mode fibers and ~10 MHz for multimode fibers.

VI. Conclusion

The SNR attainable with single mode and multimode fiber optics links was calculated from fundamental noise considerations. It was found that for single mode fibers, laser noise dominates the noise contributions for links less than 30 km long, while thermal noise dominates for longer links. Multimode fibers degrade SNR for long links because of intermode dispersion. For frequency standard transmission, as long as the baseband modulation signals are within the bandwidth of the fibers, respectable SNR can be attained with low-loss fibers (~1 dB/km) for links as long as 70 km. For wideband transmission SNR is decreased by a factor equal to the ratio of the bandwidth.

References

1. D. E. McCumber, "Intensity fluctuations in the output of CW laser oscillators. I," *Physical Review*, Vol. 141, No. 1, p. 306, 1966.

2. D. J. Morgan and M. J. Adams, "Quantum noise in semiconductor lasers," *Phys. Stat. Sol.* (a), 11, p. 243, 1972.

3. A. Yariv, *Introduction to optical electronics*, Holt, Rinehart and Winston, 1971.

4. S. D. Personik, "Time dispersion in dielectric waveguides," Bell System Technical Journal, Vol. 50, p. 843, 1971.
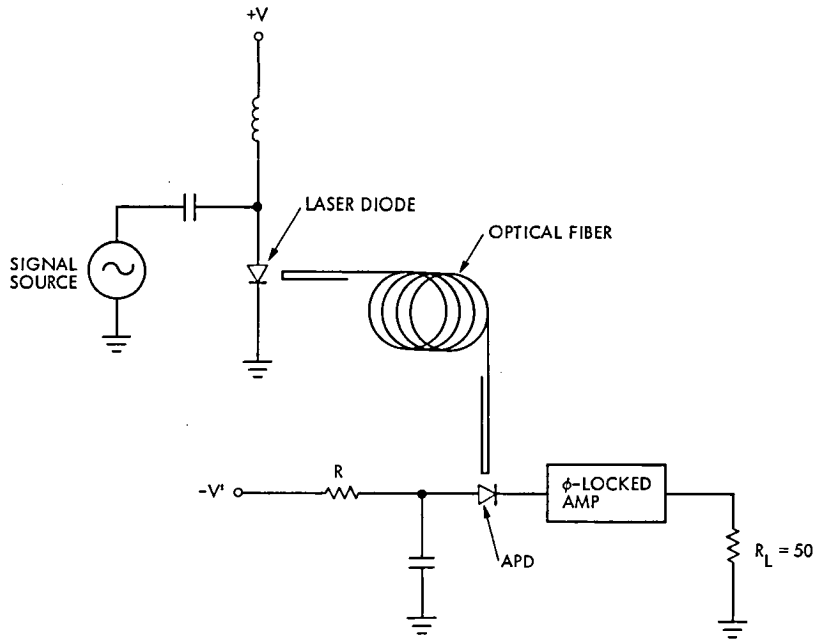
Fig. 1. Schematic fiber optics link
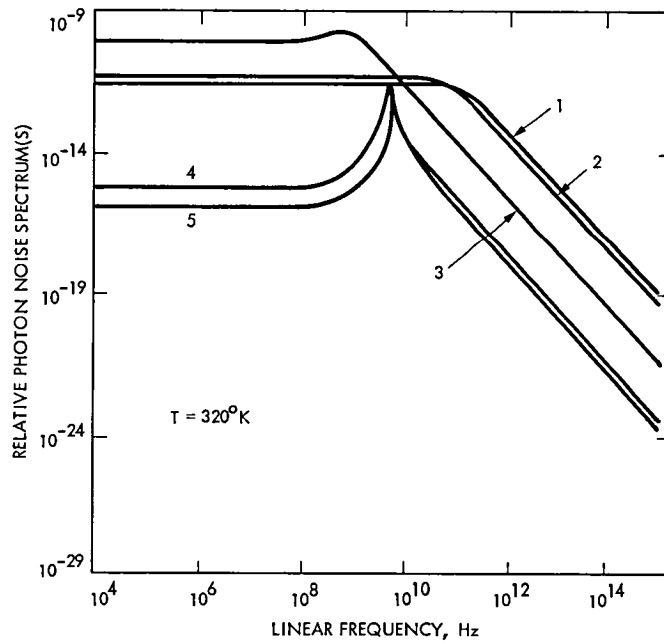
1. AVERAGE LASER OUTPUT POWER = 7.88×10^{-8} WATT
2. 1.98×10^{-7} WATT
3. 2.39×10^{-5} WATT
4. 2.38×10^{-3} WATT
5. 4.76×10^{-3} WATT

Fig. 2. Relative laser noise spectrum for various laser power outputs (from Ref. 2, assuming lasing wavelength = 9000 Å, laser cavity lifetime = 5 ps)
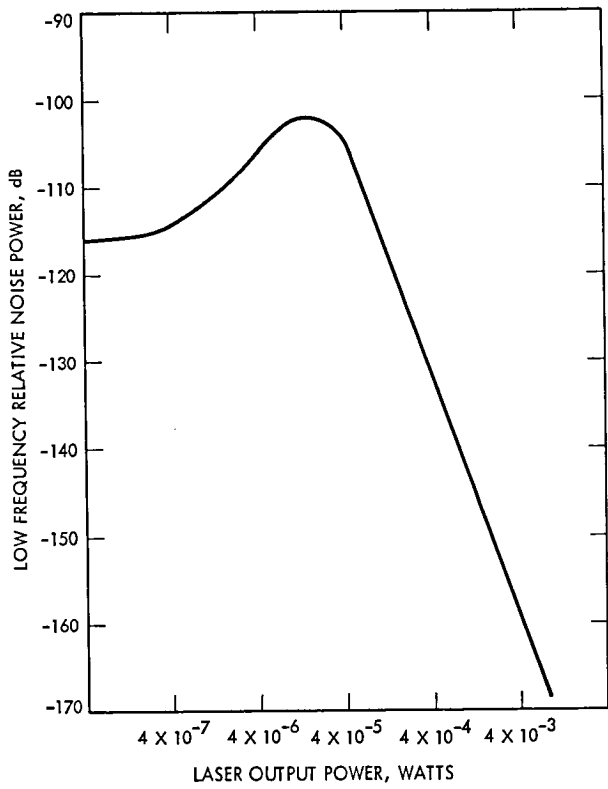
Fig. 3. Low frequency (<1 GHz) relative noise power vs average laser output power
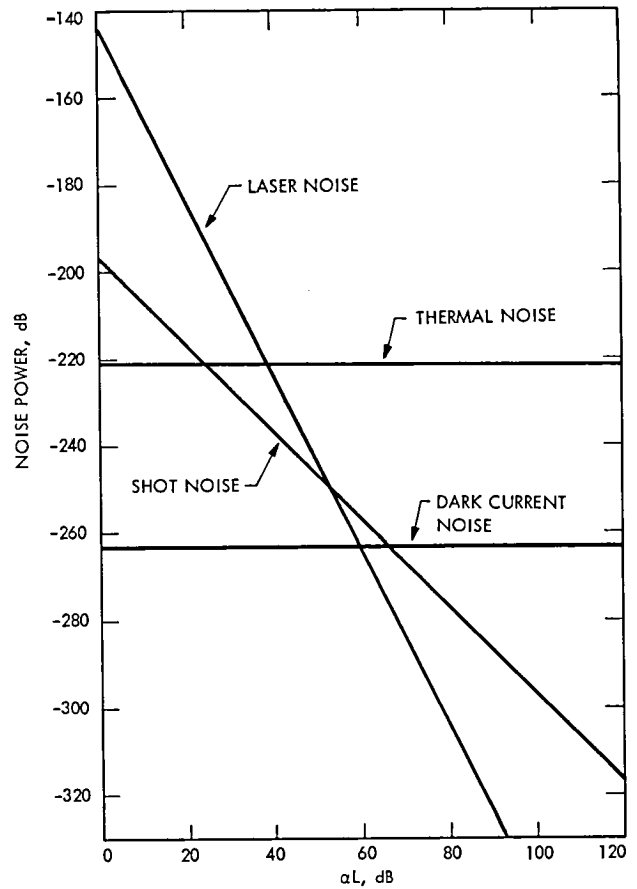
Fig. 4. Relative contributions of various noises vs total attenuation
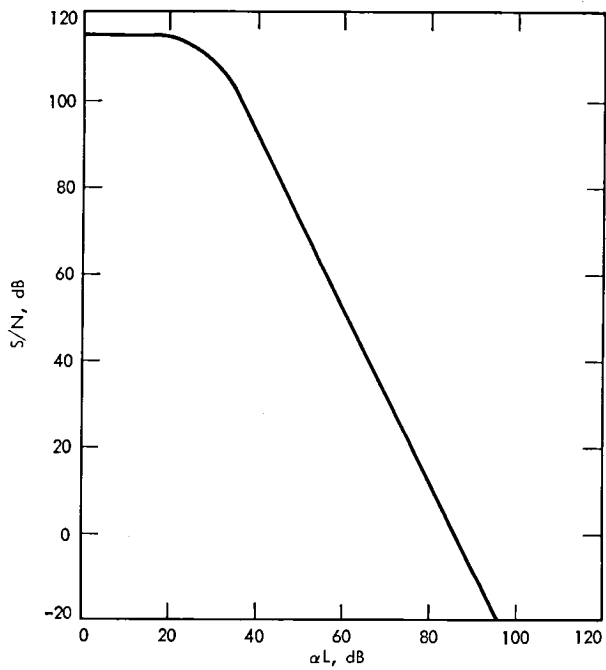
Fig. 5. Signal-to-noise ratio vs total fiber attenuation αL
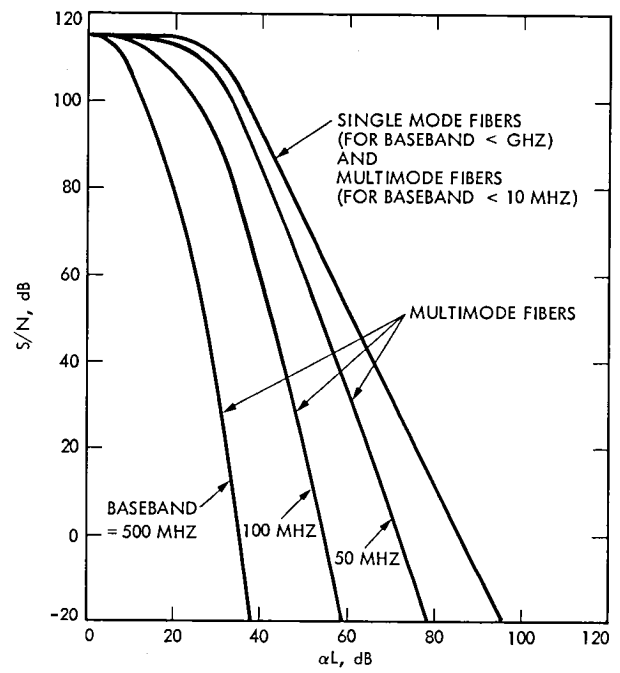
Fig. 6. Signal-to-noise ratio vs total fiber attenuation for
multimode fibers

Input Signal Conditioner for the Multimegasymbol Telemetry System Feasibility Model

G. L. Stevens

Communications Systems Research Section

Described in this article is the input signal conditioner portion of the Multimegasymbol Telemetry Demodulator and Detector Feasibility Model (MTDD-F). The input signal conditioner accepts the 55-MHz wideband IF signal of a Block IV DSN receiver and provides selectable bandpass filtering, total power automatic gain control (AGC), and frequency translation providing inphase and quadrature (I&Q) outputs at baseband.

I. Introduction

Future spacecraft carrying synthetic aperture radars (SAR's) will require telemetry systems capable of much higher symbol rates than can currently be supported in the Deep Space Network (DSN). Radar return signals received by a SAR-equipped spacecraft may be digitized and retransmitted to earth in real-time, with little or no data compression performed onboard the spacecraft. Current technology, coupled with spacecraft size, weight and power constraints, discourages onboard processing of the radar signals. As a consequence, the high rate data must be relayed to earth to be recorded and processed, producing radar reflectivity maps of the planetary surface.

In the mid-1980's the Venus Orbiting Imaging Radar (VOIR) spacecraft will carry a SAR into a Venusian orbit where it will probe through heavy clouds and gather radar information necessary to produce high-resolution radar images. This mission will require a telemetry system capable of symbol rates of several megasymbols per second (msps). Currently the highest symbol rate which the DSN can support is about 250 kilosymbols per second (ksps).

A Multimegasymbol Telemetry Demodulator and Detector-Feasibility Model (MTDD-F) is currently being developed at JPL which will be capable of demodulating and detecting telemetry streams having symbol rates of 125 ksps to 30 msps. The input signal conditioner portion of this equipment has been completed and is the subject of this article.

II. System Hardware

Figure 1 is a block diagram of the MTDD-F. Of the five elements shown, only the input signal conditioner will be discussed in this article. Other parts of the MTDD-F will be described in subsequent articles.

Figure 2 is a detailed block diagram of the input signal conditioner. Provided in the input signal conditioner is a set of IF band pass filters, an AGC loop and a complex mixer. The input signal conditioner receives its input from a wideband 55-MHz IF output port of a Block IV receiver. Inphase and quadrature baseband output signals are generated and supplied to the high-speed front end section of the MTDD-F.

A. Input Filter Module

The input filter module contains a set of five selectable 55-MHz bandpass filters which limit the receiver IF bandwidth for symbol rates in the range of 125 ksps to 4 msps. Another filter select position consists of a straight-through connection which is used when the telemetry symbol rate lies between 4 and 30 msps. In this wideband mode, system bandwidth is limited by the maser bandwidth (approximately 60 MHz two sided at -1 dB) and by the 5-pole, 40-MHz, Butterworth low-pass arm filters in the complex mixer.

Filter selection is accomplished with a pair of six-position coaxial RF relays which are controlled by a three-line TTL interface.

The bandwidths of these five filters vary in steps of one octave and are listed in Table 1 with their respective symbol rates. All of these filters are three-section Butterworth designs. Filters 2 through 5 use conventional topologies with coupled L-C sections and, in the narrow filters, input and output impedance transformers to bring element values into a realizable range. The sixth and narrowest bandpass filter is a three-section helical resonator design which exhibits a fractional frequency bandwidth of about 2-1/2 percent.

Associated with each bandpass filter is an attenuator which is used to maintain a constant gain bandwidth product for all filters. This feature makes the noise output power independent of which filter is selected, thereby reducing the required AGC range.

Shown in Fig. 3 is the input bandpass filter set with mechanical details of filter 6 shown in Fig. 4. Figure 5 shows frequency response plots of filters 2 through 6.

B. AGC Module

The input signal conditioner is designed to operate with a 55-MHz IF signal whose total signal-plus-noise (S+N) power is in the range of -20 to -50 dBm, and with symbol signal-to-noise ratios (SNR's) between -4 and +20 dB. Because of the bandlimiting which occurs in the input filter module, the AGC module must accommodate input power levels of -53 to -6 dBm.

A wideband AGC amplifier was developed which incorporates a pair of current-controlled attenuators manufactured by Mini-Circuits Laboratory (Part No. PAS-1). The configuration of this AGC amplifier is shown in Fig. 6. Simple, two-breakpoint diode linearizers are inserted in the dc control lines of the attenuators, producing a net gain coefficient of approximately 10 dB per volt over the entire 47-dB operating

range. The performance of the AGC amplifier is summarized below:

(1) Total AGC range: 60 dB.

(2) Operating AGC range: 47 dB.

(3) Gain control sensitivity: 10 dB/volt.

(4) Deviation from linear phase: $< 7°$ (25 to 85 MHz).

(5) Frequency response: ± 0.2 dB (25 to 85 MHz).

(6) Phase shift vs gain setting: $< 2°$ (Δ gain = 60 dB).

The output of the AGC amplifier is fed through a wideband IF amplifier and then passes out of the module. A sample of the AGC amplifier output is supplied to the AGC detector which is a square law, total power device. It produces an output dc voltage which is proportional to the total signal plus noise power present in the 55-MHz IF spectrum at the output of the AGC amplifier. This high-performance detector has an operating range of greater than 30 dB and is similar to one described in Ref. 1. The heart of the detector is a germanium back-diode which has a parabolic region in its current/voltage relationship. The detector output is supplied to the AGC loop filter shown in Fig. 7 whose transfer function is:

$$F(s) = \frac{\dfrac{R_2}{R_1}}{1 + R_2 CS}$$

This loop filter transfer function results in a first-order AGC control loop with a closed loop bandwidth of 16 Hz and a steady-state output power level held constant to within ± 0.3 dB over an input dynamic range of 60 dB. A dc voltmeter with special scale markings indicating proper operating range monitors the AGC control voltage.

C. Complex Mixer Module

The complex mixer receives the 55-MHz IF signal from the AGC module and a 55-MHz local oscillator (LO) signal from the MTDD-F carrier loop hardware. In the suppressed carrier mode of operation, the IF and LO signals are centered at exactly 55 MHz. In the residual carrier mode, the IF and LO signals are at 55 MHz ± 20 kHz, with the offsets being a function of the carrier doppler shift. Generated within the complex mixer are the I and Q output signals which are supplied to the high-speed front end.

Upon entering the complex mixer module, the local oscillator signal is passed through a saturating RF amplifier to establish a fixed power level. Then a 7-pole, 65-MHz low-pass

filter removes any second harmonic distortion from the limited signal. This must be done to prevent LO energy at 110 MHz from translating a portion of the input spectrum's upper sideband (which extends above 85 MHz in the wideband mode) into the dc to 30-MHz output spectrum. The filtered LO signal is further amplified and applied to a quadrature hybrid which produces 0° and 90° outputs at 55 MHz. These signals drive the LO ports of a pair of high-level, double balanced mixers.

The 55 MHz IF signal is split with a two-way power divider and applied to the R-ports of the mixers. Frequency difference terms comprise the desired baseband signals. Also included are the original input spectrum and LO signals (both attenuated by the double balanced mixer), the frequency sum terms and higher order mixer products.

Filters were designed to suppress the undesired high-frequency components at the mixer outputs, yet pass the desired dc to 30-MHz baseband signals with minimum distortion. The filters which follow the mixers are passive, lumped constant 5-pole Butterworth low-pass filters with -3 dB corner frequencies of 40 MHz. At 30 MHz these filters are down 0.5 dB, yet they provide 14 dB of attenuation to the LO leakage at 55 MHz and a minimum of 30 dB attenuation at 80 MHz, which is the lower band edge of the image spectrum centered at 110 MHz.

When the widest IF bandwidth is selected, the input spectrum extends below 25 MHz (55 MHz ±30 MHz at -1 dB). Therefore, there is an overlap in the spectra of the input and output signals and the suppression of the undesired components of the input spectrum at the mixers' outputs is limited by the isolation through the mixers and by other leakage paths. Careful layout and reasonable RF construction practice minimize the external leakage paths. Proper terminating impedances for the quadrature hybrid, inphase power splitters and mixers are insured by fixed, 50-ohm pads between these devices. Symmetry of layout and careful selection of filter components result in excellent gain and phase tracking of the I and Q channels over the entire operating frequency range of dc to 30 MHz.

After passing through the low-pass arm filters, the I and Q signals are applied to direct-coupled wideband amplifiers which boost the signal levels, provide a 50-ohm source impedance for driving terminated coaxial output cables, and include clamp circuits which hard limit the outputs at 140 percent of the full-scale output voltage.

Commercially available, ultrawideband hybrid operational amplifiers which appeared to meet the requirements of gain bandwidth product, slewrate, output current, and dc stability were procured and evaluated. These hybrid op-amps were unstable in the configuration required by this application. A discrete wideband op-amp was developed which fulfilled the requirements of the complex mixer output amplifiers. The design uses two stages of differential amplifiers plus a high current output structure. An inverting amplifier configuration is used with the voltage gain of -33 set by input and feedback resistor values. A diode clamp network limits the peak output voltage to 140 percent of the normal full scale value to protect the input circuits of the high-speed analog-to-digital converters in the high-speed front end.

These amplifiers have a closed-loop frequency response which is flat to beyond 40 MHz and operate at slew rates exceeding 400 volts per microsecond. Group delay matching of the two amplifiers permits excellent phase tracking of I and Q channels to beyond 30 MHz. DC offset controls provided in the op amps null internal offsets and also cancel mixer-generated dc offset currents. A schematic of this operational amplifier is shown in Fig. 8. The amplifiers used in I and Q channels are identical.

The complex mixer performance is summarized in Table 2.

III. Packaging

The input signal conditioner hardware is packaged in three aluminum RF modules. These modules were designed to mount in the same rack-mounted cages which are used to hold wire wrap logic boards and can therefore be conveniently employed in systems requiring a mixture of digital and RF hardware. These modules measure approximately 35 cm wide by 15 cm tall. Depth of a two-card slot module is 5.5 cm, and a three-slot module's depth is 9 cm.

Cover plates secured to each side of the modules form an RF tight enclosure. Power and dc control lines pass through multiple inductance — capacitance cavity wall feedthroughs before entering the main cavity, thus providing adequate RF isolation from outside sources of interference. Three terminal voltage regulators provide local power supply regulation within each module, generating all required voltages from single positive and negative supply mains. Shown in Fig. 9 is the complex mixer module with its cover plate removed.

IV. Summary

The MTDD-F input signal conditioner has been designed, constructed and tested. This hardware represents a significant portion of the overall system hardware. Other elements of this system are presently in development and will be the subjects of future articles.

Reference

1. Reid, M. S., Gardner, R. A., and Stelzried, C. T., *A New Broadband Square Law Detector*, Technical Report 32-1599, Jet Propulsion Laboratory, Pasadena, CA, Sept. 1, 1975.

Table 1. Bandpass filter characteristics

Number	Symbol rates	Measured, 2-Sided 3-dB bandwidths
1	4-30 msps	*
2	2-4 msps	21.8 MHz
3	1-2 msps	12.0 MHz
4	0.5-1 msps	5.9 MHz
5	250-500 ksps	2.9 MHz
6	125-250 ksps	1.25 MHz

*Bandpass filtering for the wideband mode (filter 1) is provided by the master amplifier frequency response (-1 dB at ±30 MHz) and the 5-pole, 40-MHz low-pass arm filters in the complex mixer module.

Table 2. Complex mixer performance

Parameter	Value	Comment
Total IF input power	+ 16 dBm	From AGC module output
Data peak voltage	± 0.5 volt	Noise free signal, in phase
3σ noise peaks	± 1.0 volt	Noise only, no signal
Output noise voltage	0.33 vrms (+3.5 dBm)	Noise only, no signal
Output clamp level	± 1.4 volts peak	
I&Q phase relationship	90° ± 4.3° worst case	25 MHz < F_{in} < 85 MHz
I&Q gain tracking	Within 0.2 dB	DC through 30 MHz
I&Q gain matching	Within 0.2 dB	At 10 MHz
55-MHz LO leakage	-30 dBm max.	At I&Q outputs
IF signal leakage	-40 dBc max.	At I&Q outputs
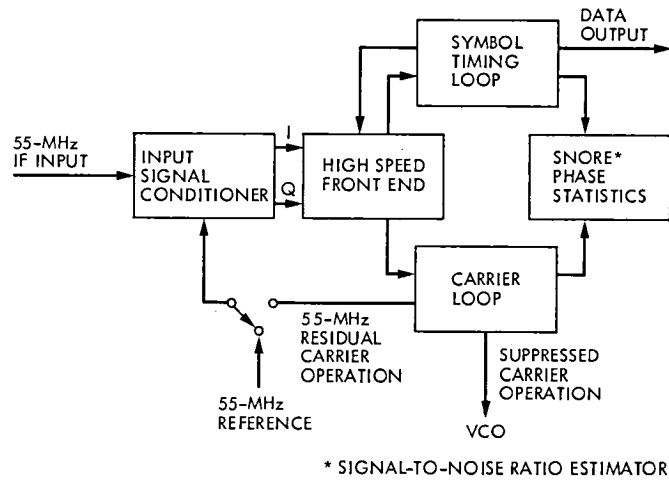
Fig. 1. Multimegasymbol demodulator and detector
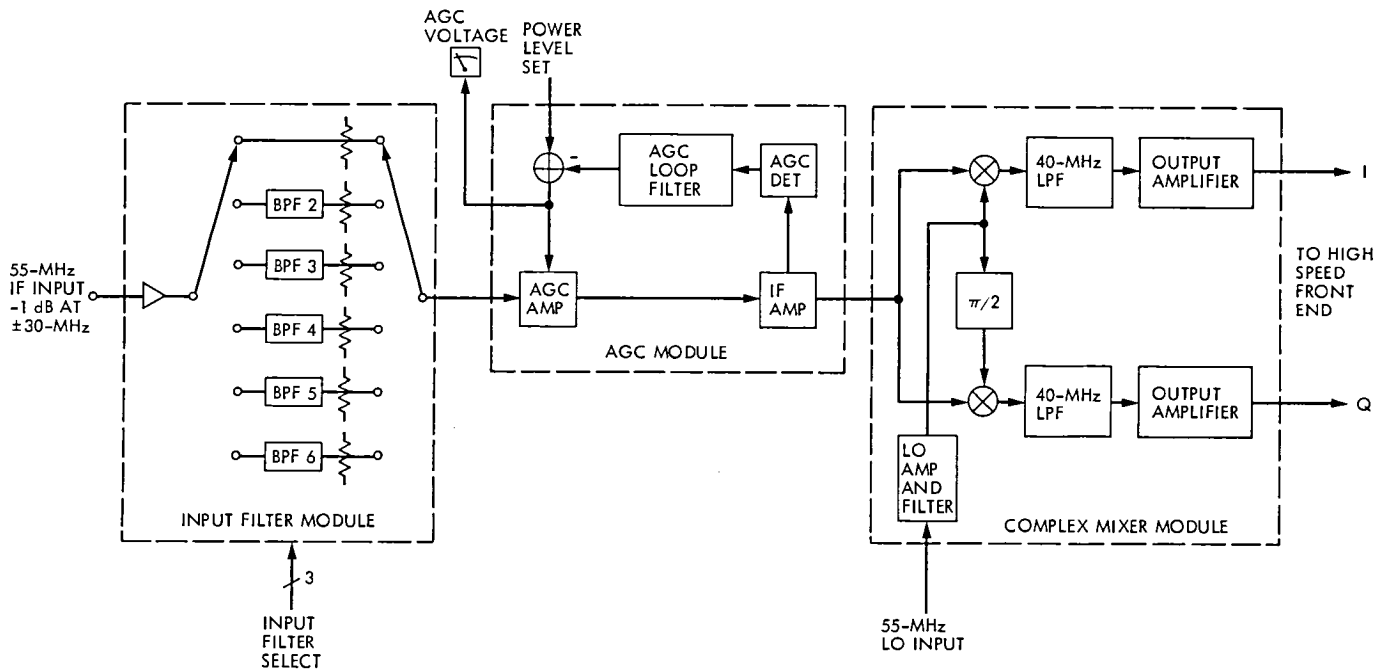
Fig. 2. Block diagram of input signal conditioner
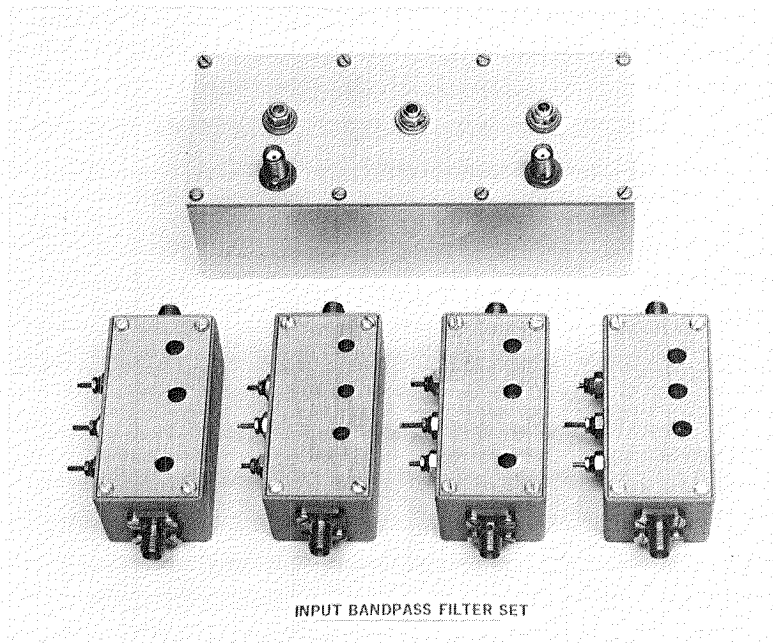
Fig. 3. Input bandpass filter set
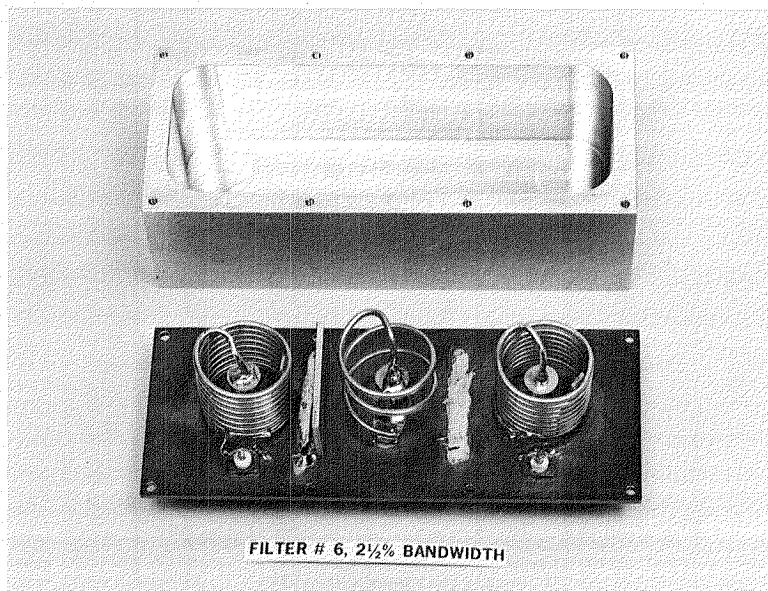
Fig. 4. Filter 6 disassembled
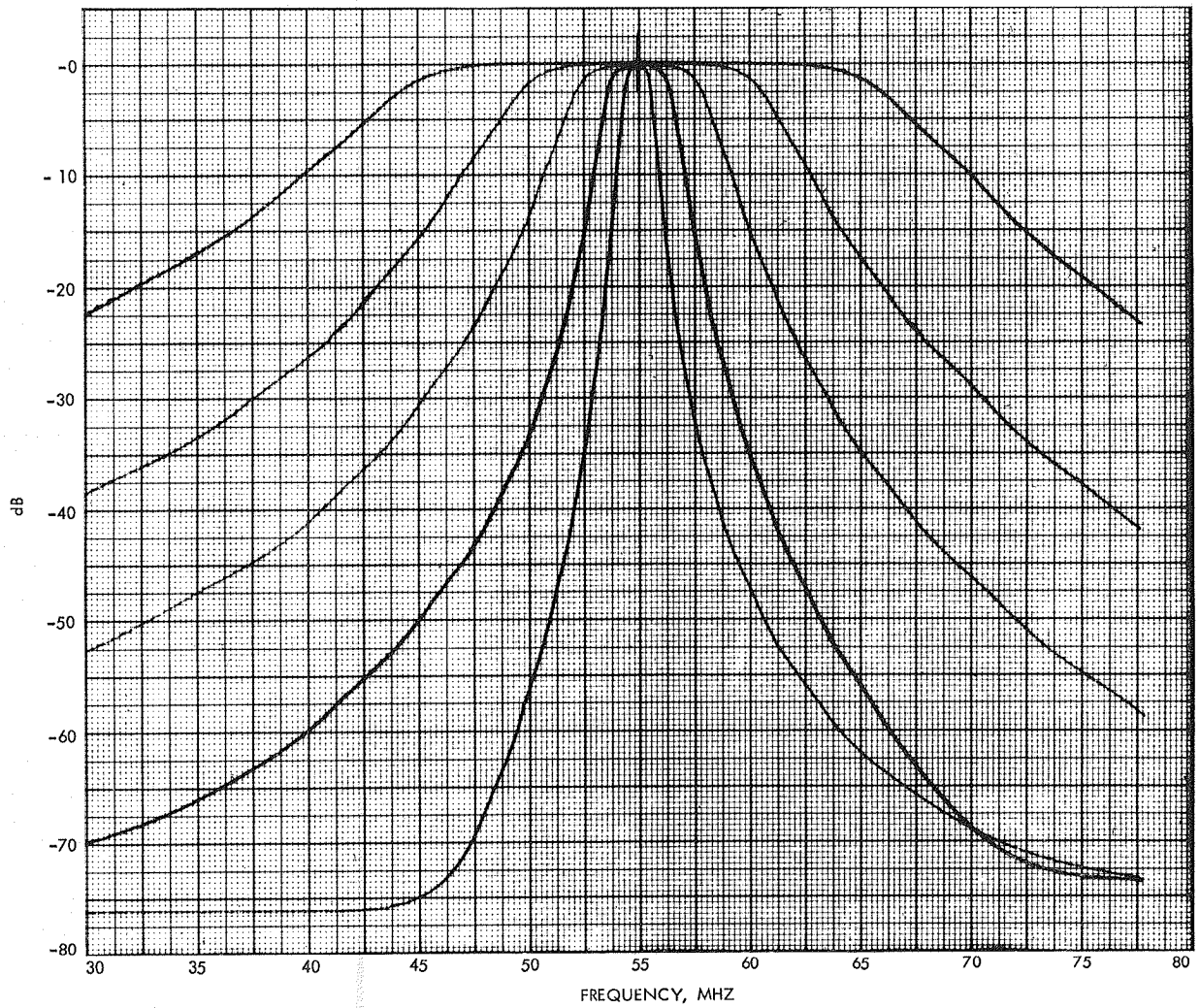
Fig. 5. Frequency response plot of filters 2 through 6
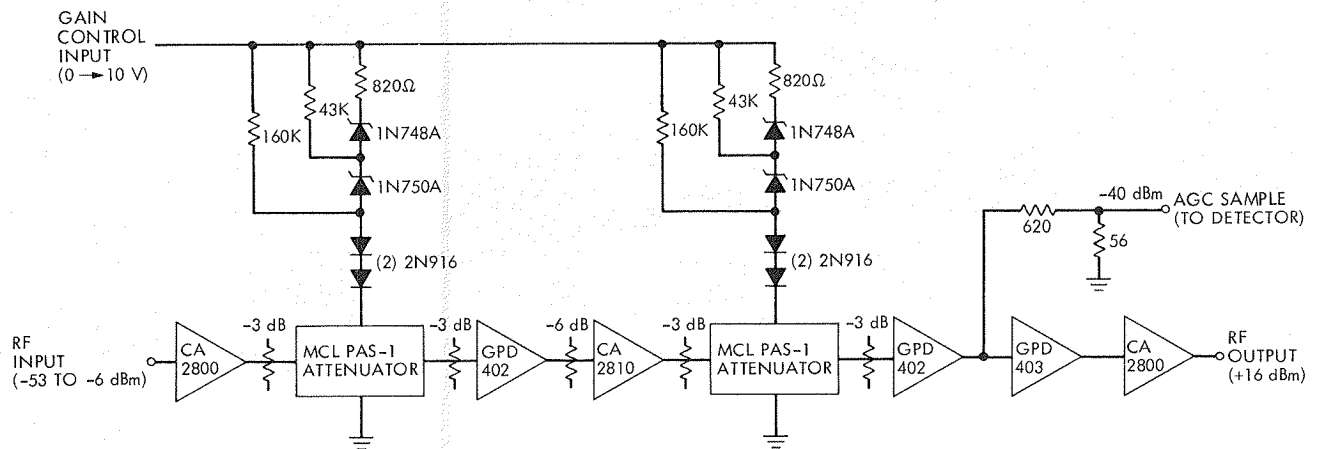
Fig. 6. Wideband AGC amplifier
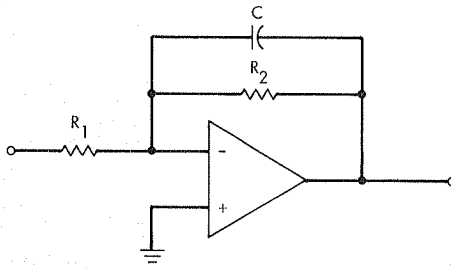
Fig. 7. AGC loop filter
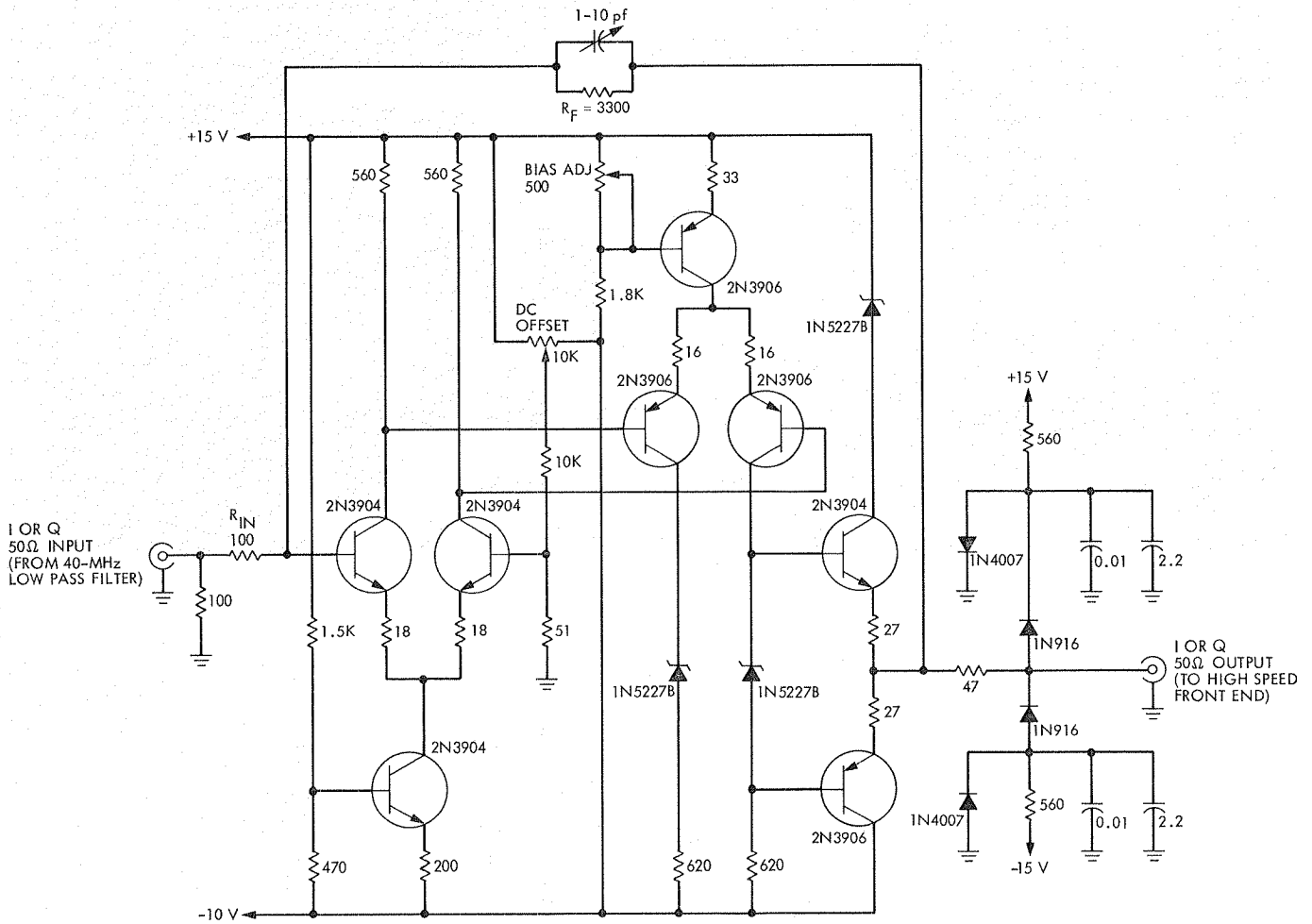
Fig. 8. Complex mixer I and Q output amplifiers
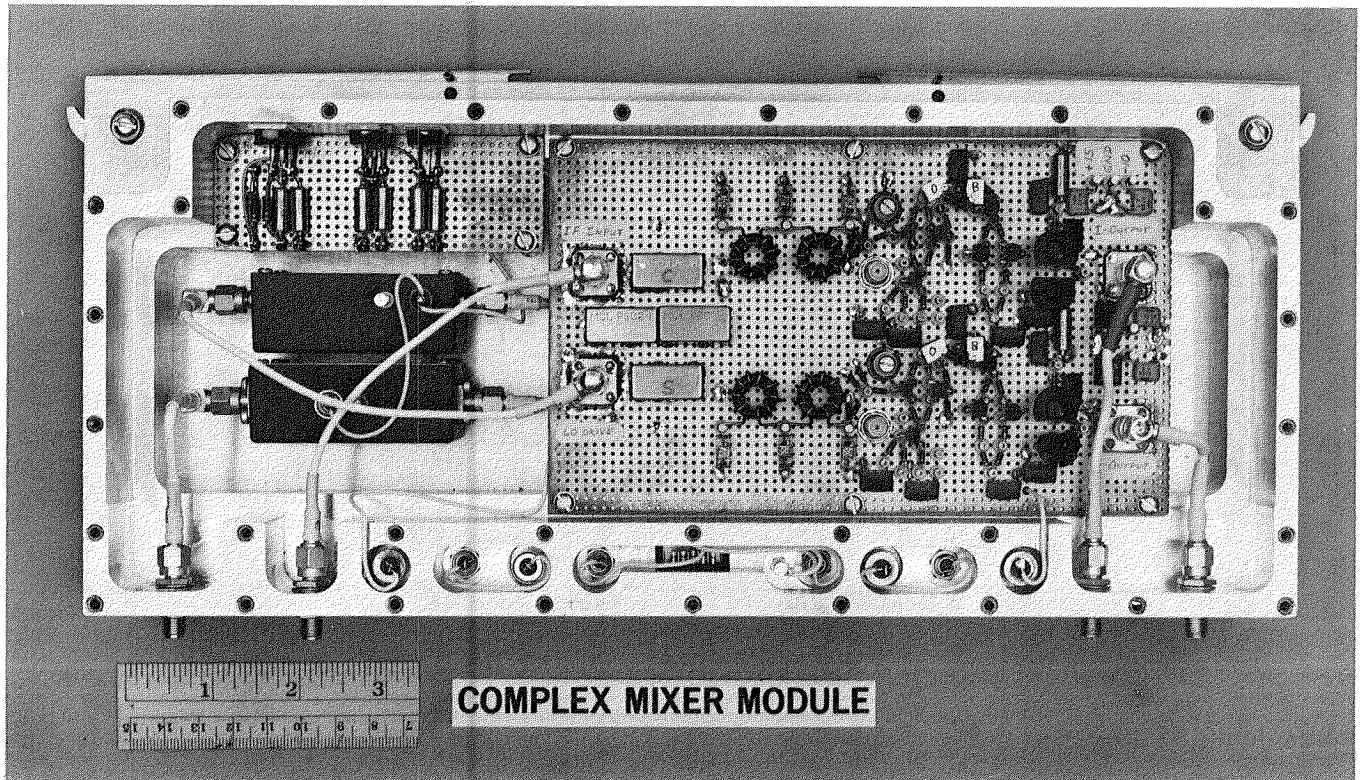
Fig. 9. Complex mixer module

Use of K$_A$-Band for Radio Metric Determinations

P. D. Potter

Radio Frequency and Microwave Subsystems Section

An article in the previous Progress Report (42-57) introduced an FY-80 study being conducted at JPL to assess the applicability of the 32 GHz K$_A$-band frequency region to planetary exploration, and considered in detail the use of the DSN 64-m antenna network at 32 GHz. The emphasis in that reporting was on increased communications link capacity by use of K$_A$-band rather than the presently used X-band. In this article, the use of K$_A$-band to alleviate the radio metric degradation caused by charged particles is discussed.

I. Introduction

The results of a study of the use of the DSN 64-m antenna network at K$_A$-band have been previously published (Ref. 1); no serious difficulty is envisioned in obtaining good antenna aperture efficiency and the requisite pointing capability. Although interest in K$_A$-band is primarily motivated by considerations of communications rate improvement and/or spacecraft antenna size reduction, the possibility of grossly reducing the deleterious effects of charged particles on radio metric data is intriguing. It is reasonable to assume that future interplanetary missions will require more precise navigation than is presently being realized, and further that these increased accuracies will be achieved by improvements in virtually all areas, including charged particle effects. While charged particle effects are not presently the dominant navigation error source, the situation might be rather different 10 years from now when the K$_A$-band link capability may have been implemented.

When the K$_A$-band frequency region is implemented, it may turn out that the first applications are radio metric rather than related to communications capability. As an example of how a minimal but effective K$_A$-band radio metric system

could be achieved, a Voyager-sized spacecraft antenna with a raw (unprocessed) power input of 0.5 watt could transmit from the planet Pluto (at its maximum range) to a 64-m antenna on Earth and produce a 10 dB signal-to-noise ratio in a 5 Hz tracking loop. This calculation assumes an overall spacecraft efficiency of 0.13, a ground efficiency of 0.27, a ground antenna elevation angle of 30 degrees, and nominal cloudy atmospheric conditions.

Apart from the interplanetary navigation application, radio metric science is becoming of ever-increasing interest. Studies of the basic properties of space, time, matter and their interrelationships are a major scientific effort. Interplanetary doppler measurements appear to offer an unusual opportunity for detection of the gravity waves predicted by general relativity (Refs. 2-5). Although it is difficult to predict the frequency of detectable gravity waves passing through the solar system (Ref. 5), the first unequivocal detection of such a spacetime disturbance will be a major scientific event. As pointed out by Thorne (Ref. 2), the ability to reliably detect gravity waves would open up a new window onto the universe, a tool for studying those astrophysical phenomena that are poorly reported to Earth by electromagnetic waves.

II. Effect of the Earth Ionosphere

The effect of the Earth ionospheric charged particles on radiowave propagation has been reviewed in detail by Lawrence et al. (Ref. 6). For radio metric considerations, the quantity of primary interest is the refractive index n (the ratio of vacuum light velocity to phase velocity), which at microwave frequencies is given by (Ref. 6),

$$n = \left[1 - \frac{\left(\dfrac{\omega_p^2}{\omega^2} \right)}{1 - \dfrac{1}{2} \dfrac{\omega_H^2 \sin^2 \theta}{\omega^2 \left(1 - \dfrac{\omega_p^2}{\omega^2} \right)} \pm \dfrac{1}{4} \left(\dfrac{\omega_H^4 \sin^4 \theta}{\omega^4 \left(1 - \dfrac{\omega_p^2}{\omega^2} \right)^2} + \dfrac{\omega_H^2 \cos^2 \theta}{\omega^2} \right)^{1/2}} \right]^{1/2} \tag{1}$$

where

ω = angular frequency of the wave

$\omega_p = (Ne^2/\epsilon_0 m)^{1/2}$ = angular plasma frequency

$\omega_H = \mu_0 He/m$ = electron angular gyro frequency

θ = angle between wave normal and geomagnetic field

N = free electron number density

e = electron charge

m = electron mass

H = geomagnetic field intensity

ϵ_0 = free space electric permittivity

μ_0 = free space magnetic permittivity

The $\pm$ sign in the denominator of Eq. (1) pertains to the ordinary and extraordinary wave indices of the refraction. At X- and K_A-bands the gyro frequency ω_H (of order 10^7 radians/sec) is small compared to ω and Eq. (1) is well approximated by,

$$n \approx \left[1 - \frac{\left(\dfrac{\omega_p^2}{\omega^2} \right)}{1 \pm \dfrac{\omega_H \cos \theta}{\omega}} \right]^{1/2} \tag{2}$$

or since $\omega_p \ll \omega$,

$$n \approx 1 - \frac{1}{2} \left(\frac{\omega_p^2}{\omega^2} \right) \left(1 \mp \frac{\omega_H \cos \theta}{\omega} \right) \tag{3}$$

Generally the last term in Eq. (3) can be neglected, resulting in an expression which is isotropic, independent of the geomagnetic field and a function of only the electron density and the frequency of operation. The change in phase pathlength, $\Delta \ell$, caused by the ionosphere, is given by,

$$\Delta \ell = \int_0^\infty (n - 1) \, dl \approx - \frac{b}{\omega^2} \int_0^\infty N dl \tag{4}$$

where

$$b = \frac{e^2}{2\epsilon_0 m} = 1.6 \times 10^3 \text{ (MKS Units)}$$

The radio metric advantage in using a higher frequency is clearly evident in Eq. (4), since uncorrected doppler data will produce the error $\Delta \ell$, and corrected data some fraction of $\Delta \ell$. As the free space light velocity is the geometric mean of phase and group velocities, it is easily shown that a ranging system will produce an opposite error, $-\Delta \ell$. This is the underlying principle of the DRVID (Differenced Range Versus Integrated Doppler) technique for charged particle calibration (Ref. 7).

A complicating feature of the ionospheric effect is that it is rapidly time variant, due both to the changing antenna elevation angle and the varying effect of the sun on the electron density. Thus for missions involving reasonably long light times, the ionospheric effect may be rather different for the transmitted and received signals (posing a problem for the S-X correction technique at least until the advent of an

X-band uplink). Also, the effect is different at different DSN stations, thus complicating the interpretation of certain types of data such as 3-way mode and VLBI.

Roughly speaking, the value of $\Delta\ell$ (Eq. 4) at X-band (8.5 GHz) is 1 cm to 1 m, depending on antenna elevation angle and local ionospheric conditions. Because of the inverse-square frequency dependence displayed in Eq. (4), the ionospheric delay, $\Delta\ell$, at K_A-band is typically a millimeter or less and always less than a few centimeters. Together with Faraday rotation, DRVID, and K_A-X-band dual frequency calibration techniques, use of K_A-band would render ionospheric effects virtually negligible.

In summary it can be said that the ionosphere represents a serious radio metric problem for which no good solution presently exists, other than an increase in frequency (such as to K_A-band). Use of tracking stations not on the Earth's surface has been investigated in detail (Ref. 8) and is not economically viable for the foreseeable future.

III. Effect of the Solar Plasma

The solar electron flux affects microwave propagation in the same way as the Earth's ionosphere; thus, the equations in the preceding section are directly applicable. A brief overview of solar plasma effects was recently published by Callahan (Ref. 9). Table 1 (based on Ref. 9) shows typical plasma properties as a function of distance from the center of the sun, in solar radii. For comparison, the Earth ionosphere is also included. Even close to the sun the effect of the solar magnetic field is small (i.e., the gyro frequency is less than 1 MHz) and the last term in Eq. (3) may be neglected. Although the plasma frequency is less than that of the Earth ionosphere, the integrated plasma effect (see Eq. 4) can be larger because of the large range involved.

Not surprisingly, the solar plasma density has a roughly inverse-square dependence on distance from the sun (Ref. 10). Thus for mission times during which the signal passes near the sun, severe doppler noise is encountered even at X-band. Figure 1 is from a JPL internal document and has been modified by adding X- and K_A-band curves, using inverse-frequency scaling[1] as suggested by A. L. Berman of the JPL Telecommunications and Data Acquisition Engineering section. In Fig. 1, the Viking data were obtained during the 1976-1977 solar conjunction and are for a 60-second doppler sample interval. The advantage of using an X-K_A-band frequency

pair for plasma effect calibrations rather than the presently-used S-X-band pair is clearly shown.

The effect of gravity waves on spacecraft doppler data was analyzed by Estabrook and Wahlquist (Ref. 4). The astronomical significance of such gravity wave tests and some of the tracking system performance requirements were discussed by Thorne and Braginsky (Ref. 5), who pointed out the importance of reducing the effect of charged particle dispersion. The philosophical importance of gravity wave detection has been emphasized by Thorne (Ref. 2). The doppler gravitational wave detection experiment has been translated into DSN performance requirements by Berman (Ref. 11). Based on expected gravity wave characteristics (Refs. 4 and 5), Berman selects solar-wind-induced maximum fractional frequency fluctuation values of 3×10^{-16} and 3×10^{-18} for minimal and desired experiments, respectively. According to Berman's calculations (Ref. 12), simultaneous two-way X-band and S-band will be required to support the minimal experiment; even more advanced techniques will be required for the desired experiment. The doppler noise improvement expected to be obtained with an X-band uplink has been discussed by Berman (Ref. 13). Figures 2 and 3 (from Ref. 13) show the expected performance levels for sun-earth-probe angles of 90° and 180° (gravity wave experiment), respectively. While these performance levels are impressive, they do not appear to be satisfactory for the gravity wave experiment.

It is clear from the discussion above that the use of K_A-band for enhancement of radio metric data by reduction of the solar plasma effect would be most desirable, and may be necessary to gravity wave experiments.

IV. Effect of the Troposphere

The Earth troposphere is of great concern to radio metric determinations because its microwave index of refraction differs by about 3×10^{-4} from unity. Moreover, its index of refraction is highly sensitive to water content along the ray-path, which can only be crudely predicted from conditions at the tracking station. Unlike the effect of charged particles, the index of refraction deviation caused by the troposphere is very nearly independent of frequency in the microwave region, as discussed below.

A very general treatment of the tropospheric index of refraction is given by Kerr (Ref. 14). The following relationship between index of refraction and attenuation is valid for virtually any medium, including gases, clouds, and rain:

$$n^2(f) - 1 = \left(\frac{10^{-6}}{LOG_{10}e} \right) \left(\frac{\lambda}{\pi^2} \right) \int_0^\infty \frac{\alpha(f')f'\,df'}{(f')^2 - f^2} \quad (5)$$

---

[1]This scaling factor arises from the fact that the plasma path length effect varies inversely with the square of the frequency (Eq. 4) and that the phase per unit length varies directly with frequency. For most applications, path length (inverse-square) is more relevant than phase.

where

f = frequency

$n(f)$ = index of refraction

λ = wavelength in cm

$\alpha(f)$ = attenuation in dB/km

e = natural logarithm base

It can be seen qualitatively from Eq. (5) that very large values of attenuation would be necessary to result in a significant variation in n. At 32 GHz, for example, an α value of 1.6 dB/km would be necessary to cause a variation of 10^{-3} in $n^2 - 1$ (Ref. 14, p. 645).

A careful measurement of the dielectric constant water vapor[2] at 9.3 and 24.8 (near the absorption resonance) GHz was reported by Birnbaum and Chatterjee (Ref. 15). With a probable error of approximately 1 percent in their measurements, they could detect no difference between the dielectric constants at these two frequencies, for a variety of temperatures and pressures. Similarly, Smith and Weintraub (Ref. 16) stated that the index of refraction of the atmosphere is independent of frequency to 30 GHz to within 0.5 percent.

Recently Berman and Slobin (Ref. 17) have discussed the expected tropospheric path length fluctuation at DSN sites and its application to gravity wave detection. They derive a typical two-way fractional frequency fluctuation value (1000 second averaging time) of 1.6×10^{-14}. Since this is larger compared to the required values (see Section III above), calibration techniques such as the water vapor radiometer are proposed.

In summary it can be said that the troposphere represents a severe problem for radio metric measurements, but appears to be amenable to calibration techniques which have not yet been implemented. In this section it has been shown that the effect is essentially frequency-independent and that thus these techniques will be as equally efficacious at K_A-band as they are at S- and X-bands.

---

[2]Index of refraction is proportional to the square root of the dielectric constant.

V. Hardware Considerations

In general, the electronic system can be designed such that hardware imperfections do not degrade the radio metric performance. For example, the spectral purity (frequency stability) of the ground transmitter should be a significant function of the frequency and timing base (the hydrogen maser) only, and phase lock loop tracking noise can be controlled by bandwidth/SNR control.

Thus, while electronic stability will be a more serious design constraint at K_A-band than it is at X-band (for example in the ground power amplifier and the spacecraft multiplier stages), this problem is amenable to a state-of-the-art engineering solution.

Two microwave hardware problems are worth considering. The first is microwave delay variation caused by imperfections in the large ground antenna. This problem has been studied in detail by Cha, et al. (Ref. 18). They found that, for example, small (~1 cm) movements of the antenna subreflector could cause delay variations of several tenths of a nanosecond. This result is, however, largely frequency independent and should not affect a decision to use K_A-band for radio metric purposes.

Secondly, the low noise maser amplifier in the ground receiving system is of concern since it has a large group delay. The stability of this delay has been determined for typical S- and X-band DSN equipment (Ref. 19, 20 and 21); typical stability over the time of one pass is ±3° phase and ±0.3 nanosecond group delay. No significant differences exist between S- and X-band data, implying a design of frequency independence and similar performance for a K_A-band maser system.

VI. Conclusion

Those aspects of radio metrics which are relevant to the possible future use of K_A-band deep space-to-earth and earth-to-deep-space links have been reviewed. From the standpoint of reducing the harmful effects of charged particles, the use of K_A-band appears highly desirable.

Acknowledgment

References

1. P. D. Potter, "64-m Antenna Operation at K_A-Band," *The Telecommunications and Data Acquisition Progress Report 42-57*, June 15, 1980.

2. K. S. Thorne, "Gravitational Wave Detection with the Solar Probe: I. Motivation," in *A Close-Up of the Sun*, JPL Publication 78-70, September 1, 1978, pp. 433-440.

3. F. B. Estabrook, "Gravitational Wave Detection with the Solar Probe: II. The Doppler Tracking Method," in *A Close-Up of the Sun*, JPL Publication 78-70, September 1, 1978, pp. 441-449.

4. F. B. Estabrook and H. D. Wahlquist, "Response of Doppler Spacecraft Tracking to Gravitational Radiation," *General Relativity and Gravitation*, Vol. 6, No. 5, October, 1975, pp. 439-447.

5. K. S. Thorne and V. B. Braginsky, "Gravitational-Wave Bursts from the Nuclei of Distant Galaxies and Quasars: Proposal for Detection Using Doppler Tracking of Interplanetary Spacecraft," *The Astrophysical Journal*, Vol. 204, February 15, 1976, pp. L1-L6.

6. R. S. Lawrence, C. G. Little and H. J. A. Chivers, "A Survey of Ionospheric Effects upon Earth-Space Radio Propagation," *Proceedings of the IEEE*, January, 1964, pp. 4-27.

7. P. F. MacDoran and W. L. Martin, "DRVID Charged-Particle Measurement with a Binary-Coded Sequential Acquisition Ranging System," *JPL Space Programs Summary 37-62*, Vol. II, March 31, 1970, pp. 34-41.

8. J. A. Hunter, *Orbiting Deep Space Relay Station Study Final Report (3 Volumes)*, JPL Publication 79-30, June 15, 1979.

9. P. S. Callahan, "Transmission Media Effects on Precise Doppler Tracking," in *A Close-Up of the Sun*, JPL Publication 78-70, September 1, 1978, pp. 450-456.

10. A. L. Berman, "A Unified Observational Theory for Solar Wind Columnar Turbulence," *The Deep Space Network Progress Report 42-50*, April 15, 1979, pp. 124-131.

11. A. L. Berman, "The Gravitational Wave Detection Experiment: Description and Anticipated Requirements," *The Deep Space Network Progress Report 42-46*, August 15, 1978, pp. 100-108.

12. A. L. Berman, "Solar Wind Density Fluctuation and the Experiment to Detect Gravitational Waves in Ultraprecise Doppler Data," *The Deep Space Network Progress Report 42-44*, April 15, 1978, pp. 189-196.

13. A. L. Berman, "Simultaneous Dual-Frequency, Round-Trip Calibration of Doppler Data with Application to Radio Science Experiments" *The Deep Space Network Progress Report 42-48*, December 15, 1978, pp. 48-54.

14. D. E. Kerr, Ed., *Propagation of Short Radio Waves*, McGraw-Hill Book Company, Inc., 1951, pp. 641-646.

15. G. Birnbaum and S. K. Chatterjee, "The Dielectric Constant of Water Vapor in the Microwave Region," *Journal of Applied Physics*, Volume 23, No. 2, February, 1952, pp. 220-223.

16. E. K. Smith, Jr. and S. Weintraub, "The Constants in the Equation for Atmospheric Refractive Index at Radio Frequencies," *Proceedings of the I.R.E.*, Vol. 41, August, 1953, pp. 1035.

17. A. L. Berman and S. D. Slobin, "Tropospheric Path Length Fluctuation in Temperature Semiarid Locales: Application to the Gravitational Wave Detection Experiment," *The Deep Space Network Progress Report 42-55*, February 15, 1980, pp. 79-85.

18. A. G. Cha, W. V. T. Rusch and T. Y. Otoshi, "Microwave Delay Characteristics of Cassegrainian Antennas," *IEEE Trans. on Ant. and Prop.*, Vol. AP-26, No. 6, November, 1977, pp. 860-865.

19. R. Clauss, E. Weibe and R. Quinn, "Low-Noise Receivers: Microwave Maser Development," JPL Technical Report 32-1526, Vol. XI, Oct. 15, 1972, pp. 71-80.

20. D. L. Trowbridge, "X–Band Traveling Wave Maser Amplifier," *The Deep Space Network Progress Report 42-28*, Aug. 15, 1975, pp. 69-77.

21. J. M. Urech, et al., "S–Band Maser Phase Delay Stability Tests," *The Deep Space Network Progress Report 42-48*, December 15, 1978, pp. 102-117.

Table 1. Plasma properties

R ($R_\odot$)	Electron density (cm^{-3})	f_p (Hz)	f_g (Hz)	$(f_p/f_s)^2$	$(f_p/f_s)^2 R$ (m)	f_g/f_s
5	2.8×10^4	1.5×10^6	1.3×10^5	2.9×10^{-8}	9.8×10^1	1.5×10^{-5}
10	5.3×10^3	6.6×10^5	3.3×10^4	5.4×10^{-9}	3.8×10^1	3.9×10^{-6}
21.6	1.1×10^3	2.9×10^5	7.0×10^3	1.1×10^{-9}	1.6×10^1	8.2×10^{-7}
216	9.4	2.7×10^4	7.1×10^1	9.8×10^{-12}	1.4	8.6×10^{-9}
Ionosphere ($R = 200$ km)	2.0×10^5	4.0×10^6	8.4×10^5	2.0×10^{-7}	4.3	9.9×10^{-5}

f_p = plasma frequency = $8.98 \times 10^3 \, N^{1/2}$ Hz

f_g = gyro frequency = $2.80 \times 10^6 \, B$ Hz

$$n^2 = \frac{1 - f_p^2/f^2 \pm f_g/f}{1 \pm f_g/f}$$

f_s = signal frequency = 8.5 GHz
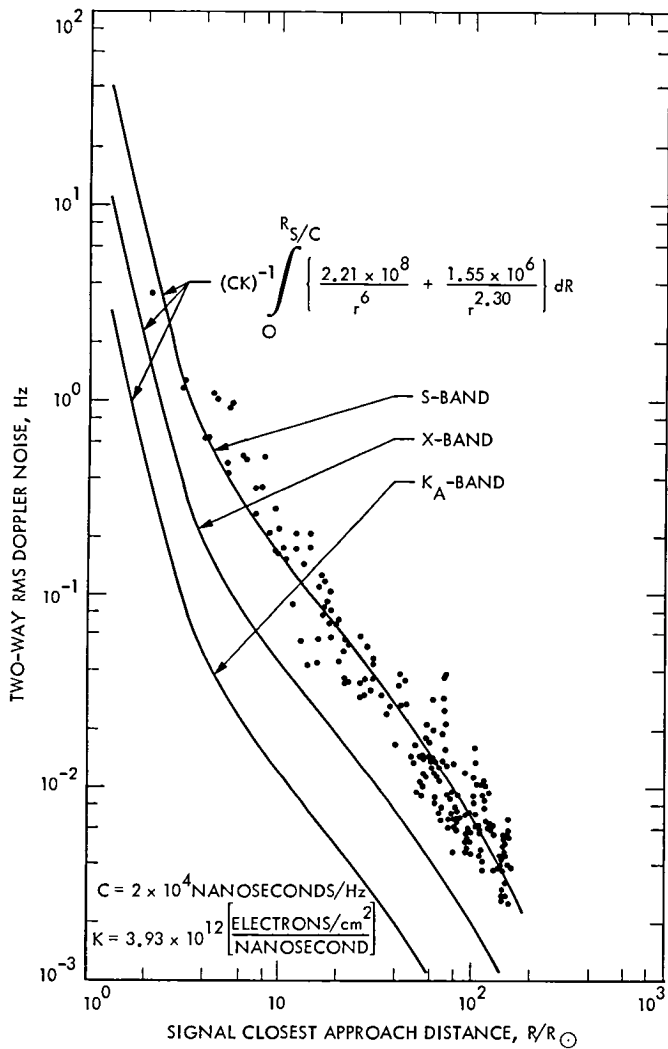
Fig. 1. Doppler phase fluctuation vs signal closest approach to the Sun
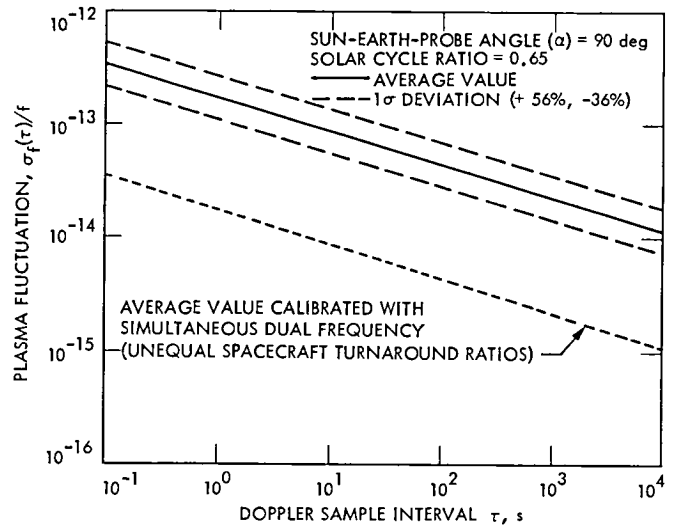
Fig. 2. Two-way X-band plasma fluctuation at solar cycle minimum
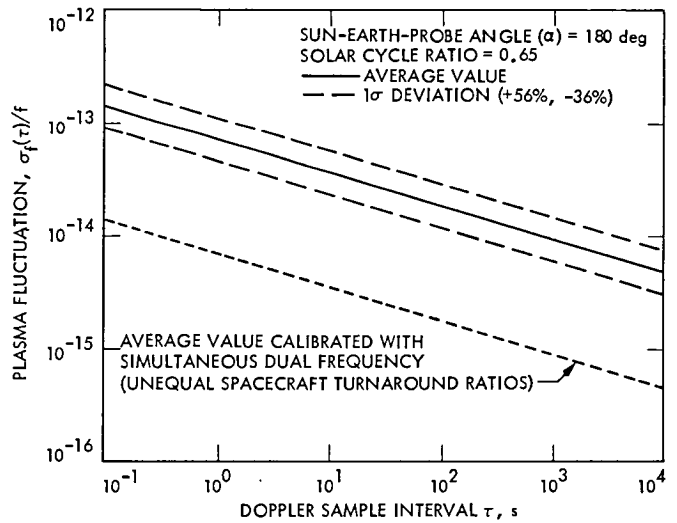
Fig. 3. Two-way X-band plasma fluctuation at solar cycle maximum

Quicklist—The Basis for a Computer-Aided Logic Design System

W. A. Lushbaugh

Communications Systems Research Section

The description of a digital system must eventually include a point-to-point wire list. Previous methods of computer-generated wire lists have required one record of input for each point to be wired. Quicklist is a preprocessor for an existing wire listing program that cuts the description of the wire list by about 67 percent over previous methods. Quicklist is intended to be the basis of a computer-aided logic design system.

I. Introduction

Many digital systems are constructed on wire wrap boards. These boards are most conveniently wired by automatic or semiautomatic wire wrap systems for large quantity productions, but many prototype and small quantity boards are still wrapped by hand. In any event, a computer-generated wire list is advantageous to expedite the work. Most wire listing programs, however, require one record of input for each point to be wired. Quicklist is a preprocessor for an existing wire list program that cuts the description of the wire list by about 67 percent over previous methods. Quicklist is intended to be the basis of a computer-aided logic design system.

II. Review of Wire List Program

H. C. Wilck has written a program that has proved very useful in providing wire listing information for the wire wrap board used by the Digital Projects Group. This program is a very advanced program in that it allows inputs in the form of chip signal names rather than actual chip pin numbers,

although the user may call out chip pin numbers if desired. The method by which this is accomplished is to provide a definition deck in front of the wiring information. Some of the highlights of this program follow:

The definition deck has the following format:

D, type, number of pins, number of defined pins, spacing, description

1, type, pin number — pin function, pin number — pin function, . . .

2, type, pin number — pin function, . . .

.
.
.

D, type, . . .

where the terms have the following definitions:

Type: 1 to 8 alphanumeric characters used to designate the dual in-line package (DIP); e.g., SN 7400.

Number of Pins: A decimal number (NP) specifying the number of pins on the DIP. $2 \leqslant NP \leqslant 88$.

Number of Defined Pins: A decimal number (NDP) specifying the number of pin definitions that follow. If NDP < NP then there are pins that the manufacturer has not connected.

Spacing: A decimal number (SP) specifying the spacing between the two columns of pins on the DIP in tenths of an inch.

Description: 0 to 60 alphanumeric characters describing the nature of the package; e.g., DUAL J-K FLIP-FLOP.

Pin Number: A decimal number (N) that designates the pin to be named. $1 \leqslant N \leqslant NP$.

Pin Function (name): 0 to 4 alphanumeric characters. This name describes the electrical function of the pin; such as OUT1, A0, A1, IN3, Q1', etc. The pin function may be used in lieu of the pin number when the wire listing data is given to the program.

The SIGNAL ASSIGNMENT DECK is the actual wire routing information to the program. This deck is chip oriented, i.e., input is grouped by DIP's, with all signals on one chip entered as a group. The format of this deck is:

P, LOC, Type, Function

1, LOC, pin id(entification) — signal name, pin id — signal name, . . .

2, LOC, pin id — signal name, . . .

.
.
.

P, LOC, Type, . . .

where these terms have the following definitions:

LOC: A five-digit number specifying the location of the corner pin (pin 1) of the chip on the board.

Type: 1 to 8 alphanumeric characters. This must agree with one of the types in the definition deck.

Pin id: Either the actual pin number of the chip or the mnemonic pin function assigned to that pin in the definition deck.

Signal name: 1 to 8 alphanumeric characters that identify the signal to be connected to the pin specified by the pin id.

Every pin tied to the same signal name will be tied together by the wire listing program.

Special Characters. Both in the definition deck and the signal assignment deck the dash (-) between pin number — pin function or pin identification — signal name may be replaced by other special signals. These are:

& — defines the pin to be an output that can be collector or-ed or tri state.

* — defines the pin to be an output that cannot be tied to another output.

+ — defines the pin as connected to +5V.

> — defines the pin to be connected to ground.

III. Quicklist

Quicklist is a preprocessor program written to shorten the input signal assignments to the program described above. Quicklist uses two different methods to shorten the input data. The first of these is the use of parentheses to allow a compact way of describing signal names which increment (or decrement) by one, i.e., typical signal names in a bus. The other method used is the equal sign. Using this symbol in a signal list says that the rest of the signals on that chip are the same as those on the previous chip described. Inputs to Quicklist look very similar to those described above; i.e., a typical signal assignment deck is:

P, LOC, type, function

1, LOC, pin id — signal name, . . .

except that cards with numbers in col. 1 may take the form

1, LOC, pin id $(N_1 - N_2)$ — signal name $(N_3 - N_4)$, . . . , =

where pin id $(N_1 - N_2)$ is the name (as called out in the definition deck) of a *set* of pins that have names that go in order from N_1 to N_2. For example, for the 2147 memory chip A00, A01, . . . A11 are the 12 address inputs. Similarly, signal name $(N_3 - N_4)$ is the name of a set of signals that run from say $SIGN_3$ to $SIGN_4$; e.g., ADBUS 00 to ADBUS 11. As an example, consider two 2147 chips wired to the same address buss, write enable and chip select. The Quicklist input would then be:

P, LOC, 2147, Memory 1

1, LOC, DIN-DATA0, DOUT-DOUT0

2, LOC, A(0-11) — ADBUS(0)

3, LOC, WE-WRTEN, CS-CHPSEL

P, LOC1, 2147, Memory 2

1, LOC1, DIN-DATA1, DOUT-DOUT1, =

The output from these five input cards would be:

P, LOC, 2147, memory 1

1, LOC, DIN-DATA0; DOUT-DOUT0

2, LOC, A00-ADBUS00, A01-ADBUS01, . . .

3, LOC, A04-ADBUS04, . . .

4, LOC, A08-ADBUS08, . . . , A11-ADBUS11

5, LOC, WE-WRTEN, CS-CHPSEL

P, LOC1, 2147, memory 2

1, LOC1, DIN-DATA1, DOUT-DOUT1

2, LOC1, A00-ADBUS00, A01-ABUS01, . . .

3, LOC1, A04-ADBUS04, . . .

4, LOC1, A08-ADBUS08, . . . , A11-ADBUS11

5, LOC1, SE-WRTEN, CS-CHPSEL

In this case, the 16 nonpower and ground signals of the first chip were described with three short inputs cards, and the second chip was described in only two cards due to the use of the equal sign.

It should be noticed that Quicklist provides automatic double digiting; i.e., if either N_1 or N_2 is a two-digit number, then all the numbers from N_1 to N_2 are put in double-digit format. The same is true of the pair N_3 and N_4. The use of N_2 or N_4 is optional, but at least one of them must appear. To clarify this, the following input strings all produce identical output:

A(00-11) − ADBUS (00-11)

A(0-11) − ADBUS(00-11)

A(0-11) − ADBUS(0-11)

A(0-11) − ADBUS(0)

A(0) − ADBUS(0-11)

Notice that the last two of these are the easiest to enter and the second from last is the one to be recommended; i.e., put the range of the bussed signal on the side where the definition deck can pick up any errors.

Either N_1 or N_3 may be a single letter. This accommodates chips whose outputs are, for example, QA, QB, QC, QD as in the SN74163. N_1 must be smaller than N_2 but N_3 is allowed

to be less than N_4 (including letters with $A < B < C \ldots$ etc.). In this case autodecrementing of signal names is supplied, but autoincrementing on N_1 is always done. Thus, the string

A(0) − ADBUS(11-0)

will produce output of the form

A00 − ADBUS11, A01 − ADBUS10, A02 − ADBUS09, etc.

Table 1 shows some typical examples of the forms pin id $(N_1 - N_2)$ - sig name $(N_3 - N_4)$. Note that pin id as well as sign name are optional. Also, one of the pairs N_1, N_2 or N_3, N_4 may be omitted.

IV. Future Expansion

Quicklist can easily be expanded and generalized to be of even more use to the design engineer. The syntax of Quicklist and the associated program should allow dummy variables and loops as in any high-level programming language. To allow this, however, one must, and indeed would like to, allow the LOC(ation) field of the signal list input cards to be mnemonics for locations that would be filled in later by a location deck which would locate the DIPs on the board. This feature would also allow an easy way to leave a design fixed but to transfer it to a different board that might have a different geometry. An example will clarify this. Consider the following set of input cards:

FOR I:=0, 7

P, M(I), 2147, 4K MEMORY

1, M(I), A(0-11) − ADBUS(0)

2, M(I), D IN − DATA(I), DOUT-DOUT(I)

3, M(I), WE-WRTEN, CS-CHPSEL

END

This syntax describes a 4 K by 8-bit memory consisting of eight 2147's all tied to the same address buss, write enable, and chip select. The data input of each of these eight chips is tied to one of a data input bus DATA0 through DATA7 and the data output tied to a data output bus. The locations of these eight chips are unspecified but these locations have been assigned the mnemonics M0 through M7, and will be assigned at a later time. Once dummy variables are allowed, nested loops and arithmetic expressions would be a natural extension.

For example:

FOR I:=0, 3

P, R(I), SN54LS374, 8 BIT REGISTER

1, R(I), D(0-7) — INBUS(0+8*I)

2, R(I), Q(0-7) — OUTBUS(0+8*I)

3, R(I), CL-CLOCK, OS-OUTSEL

END

would describe a 32-bit hold register, consisting of four SN54LS374 DIP's each containing 8 bits.

The constraint that all inputs of a DIP be input as a group should also be dropped. When designing things like counters, many of the inputs can easily be described by the above-mentioned syntax, but certain inputs like carry in and carry out are different for each chip in the design. For instance, a 20-bit counter using SN54163's would most easily be described as

FOR I:=0,3

P, AD(I), SN54163, 4 BIT COUNTER

1, AD(I), (A-D) — INBUS (0+4*I)

2, AD(I), Q(A-D) — AD(0+4*I)

3, AD(I), LD-LOAD, CK-CLOCK, CLR-CLEAR

END

4, AD0, EP-ENABLE, ET-ENABLE, RCO-RIPCRY

4, AD1, EP-RIPCRY, ET-RIPCRY, RCO-CRY1

FOR I:= 2,3

4, AD(I), EP-RIPCRY, ET-CRY(I-1), RCO-CRY(I)

END

V. Conclusion

Quicklist has proven quite useful to those who have used it. The number of keystrokes necessary to describe digital systems has been reduced up to 67 percent in systems that have a highly bussed structure. The future plans for expansion would further increase the effectiveness of the program and make it the basis for a computer-aided-design system.

Table 1. Quicklist examples

Example	Result (first, second, . . . last)
A(0) – BUS(0-11)	A00 – BUS00, A01 – BUS01, . . . , A11 – BUS11
A(0-11) – BUS (0)	A00 – BUS00, A01 – BUS01, . . . , A11 – BUS11
A(0) – BUS(11-0)	A00 – BUS11, A01 – BUS10, . . . , A11 – BUS00
A(5-8) – BUS(0)	A5 – BUS0, A6 – BUS1, . . . , A8 – BUS3
Q(A) – BUS(0-3)	QA – BUS0, QB – BUS1, . . . , QD – BUS3
Q(D) – BUS(D-A)	QD – BUDD, QE – BUSC, . . . , QG – BUSA
A(6-9) – (0)OUT	A6 – 0OUT, A7 – 1OUT, . . . , A9 - 3OUT
A(4-7) – (2(0)B	A4 – 20B, A5 – 21B, . . . , A7 – 23B
IN(A)1 – T(0-4)6B	INA1 – T06B, INB1 – T16B, . . . , INE1 – T46B
A(5-9) – RESET	A5 – RESET, A6 – RESET, . . . , A9 – RESET
A(0-3)>	A0>, A1>, . . . , A3>; grounds four pins
(1-4) – RESET	1 – RESET, 2 – RESET, . . . , 4 – RESET
(1-4) +	1+, 2+, 3+, 4+, ties pins 1-4 to +5V

Concerning the Feasibility of a Real-Time SAR Digital Processor for VOIR Low Resolution Imaging Modes

T. K. Truong and R. G. Lipes

Communications Systems Research Section

In this article, the feasibility of real-time digital processing of synthetic aperture radar data for Venus Orbiting Imaging Radar low resolution modes is investigated. First, it is shown that range migration is not a problem for these modes. Then, under the assumption of no range migration, fast Fourier transform implementations for accomplishing both range and azimuth correlation in real-time are shown to be feasible with current technology. Treatment of other important aspects of real-time processing such as automatic focusing and Doppler centroid location is deferred to subsequent articles.

I. Introduction

An efficient synthetic aperture radar (SAR) processing algorithm such as the one proposed in this article could provide the basis for a real-time SAR correlator implementation in the Deep Space Network (DSN). A real-time SAR correlator located in a DSN station would reduce the high-rate SAR raw data, expected from the proposed Venus Orbiting Imaging Radar (VOIR) mission of the mid 1980s, directly into lower rate image data. This could introduce savings in both time and costs by potentially eliminating the transport of high density tapes of raw SAR data from DSN stations to JPL for processing. Furthermore, it would provide a quick-look capability for verifying that SAR sensor and data communications are operating as expected.

One problem in investigating the feasibility of real-time SAR processing for the VOIR mission arises from changes in mission requirements as different approaches are explored and funding baselines are altered. To avoid tracking these changes, an interim set of requirements (Ref. 1) was chosen as a basis for the feasibility study, with the realization that a final set exhibiting large departures from this set could alter the conclusions. The approach to the feasibility study was to develop a conceptual design that could be implemented with proven special purpose hardware. Furthermore, the initial design discussed in this article was not required to accommodate SAR data with significant range migration. Subsequent studies will address processing techniques for such data.

In Section II, the extent of range migration is determined for the various options in Ref. 1. Only the low-resolution mode is essentially free of range migration. For this mode, a design based on a fast Fourier transform (FFT) implementation is presented. In Sections III and IV, the feasibility of real-time correlation in range and azimuth respectively is demonstrated.

II. Computation of Range Migration of VOIR-SAR Processor

A set of VOIR system characteristics given in Ref. 1 is given in Table 1. From Table 1, one observes that two sets of parameters of low resolution and high resolution at incidence angles $\theta = 25$ and $\theta = 52$ are given. To compute the range migration for these two imaging modes, let

f: carrier frequency

L_a: azimuth length of reference filter per look

L: total azimuth length of reference filter

λ: wavelength

R: slant range

ΔZ: azimuth resolution

ΔR: range resolution

N: number of looks

Δx: pixel spacing in the final imagery

τ_a: integration time per look

ΔR_c: range curvature

ΔR_w: range walk

ΔR_m: range migration

v: the nominal spacecraft speed

B: bandwidth of the pulse

f_s: sampling frequency

f_d: doppler center frequency

H: altitude

θ: incident angle

c: speed of light

PRF: pulse repetition frequency

It was shown (Ref. 2) that the azimuth length of the reference filter per look is

$$L_a = \frac{\lambda R}{2 \Delta Z} \qquad (1a)$$

where R is defined by

$$R = \frac{H}{\cos \theta} \qquad (1b)$$

Then the actual azimuth length of the reference filter is

$$L = N L_a = N \frac{\lambda R}{2 \Delta Z} \qquad (2)$$

It was also shown (Refs. 3 and 4) that the range curvature and the range walk of the reference filter are

$$\Delta R_c = \frac{L^2}{8R} \qquad (3)$$

and

$$\Delta R_w = \frac{\lambda}{2} (f_d N \tau_a) \qquad (4a)$$

where τ_a is given by

$$\tau_a = \frac{L_a}{v} \qquad (4b)$$

and the range migration is given by

$$\Delta R_m = \Delta R_c + \Delta R_w \qquad (5)$$

The sampling frequency is defined by

$$f_s \cong 1.2 \, B > B$$

The pixel spacing of the final imagery is given by

$$\Delta x = \frac{c}{2 f_s} \qquad (6)$$

Note that if $\Delta R_m \leqslant \Delta x$, then range migration is not important. Otherwise, range migration must be treated.

From the parameters given in Table 1 and the assumption of 1 KHz as a representative doppler center frequency, one can compute the range migration of the high-resolution and the low-resolution imaging modes as follows:

Case 1: High-resolution imaging mode from Eq. (6),

$$\Delta x = \frac{c}{2 f_s} = \frac{2.998 \times 10^8}{2 \times 1.2 \times 4.75 \times 10^6} = 26.3 \text{ m}$$

$$\lambda = \frac{c}{f} = \frac{2.998 \times 10^8}{12.75 \times 10^8} = 0.235 \text{ m}$$

(a) For $\theta = 25°$,

$$R = \frac{H}{\cos \theta} = \frac{300 \text{ km}}{\cos 25°} = 331.13 \text{ km}$$

$$L_a = \frac{\lambda R}{2\Delta Z} = \frac{0.235 \times 331.13 \times 10^3}{2 \times 50} = 778 \text{ m}$$

$$\Delta R_c = \frac{1}{8} \frac{(8L_a)^2}{R} = \frac{8 \times (778)^2}{331.13 \times 10^3} = 14.6 \text{ m}$$

$$\tau_a = \frac{L_a}{v} = \frac{778 \text{ m}}{6600 \text{ m/s}} = 0.12 \text{ sec}$$

$$\Delta R_w = \frac{\lambda}{2}(f_d \times 8\tau_a) = \frac{0.235}{2}(1000 \times 8 \times 0.12) = 121 \text{ m}$$

$$\Delta R_m = \Delta R_c + \Delta R_w = 14.6 + 121 \text{ m} = 136 \text{ m}$$

Note that for this case,

$$\Delta R_c = 14.6 \text{ m} < \Delta x = 26.3 \text{ m}$$

$$\Delta R_m = 136 \text{ m} > \Delta x = 26.3 \text{ m} \qquad (7)$$

(b) For $\theta = 52°$,

$$\Delta R_c = 21.5 \text{ m}, \qquad \Delta R_w = 180 \text{ m}, \qquad \text{and}$$

$$\Delta R_m = \Delta R_c + \Delta R_w = 21.5 + 180 = 201.5 \text{ m}$$

Note that

$$\Delta R_c = 21.5 \text{ m} < \Delta x = 26.3 \text{ m}$$

$$\Delta R_m = 201.5 \text{ m} > \Delta x = 26.3 \text{ m} \qquad (8)$$

Case 2: Low-resolution imaging mode. From Eq. (6), one obtains

$$\Delta x = 156 \text{ m} \quad \text{and} \quad \lambda = 0.235 \text{ m}$$

(a) For $\theta = 25°$,

$$\Delta R_c = 3.6 \text{ m}, \qquad \Delta R_w = 53.58 \text{ m}, \qquad \text{and}$$

$$\Delta R_m = 57.18 \text{ m}$$

Note that

$$\Delta R_c = 3.6 \text{ m} < \Delta x = 156 \text{ m}$$

$$\Delta R_m = 57.18 \text{ m} < \Delta x = 156 \text{ m} \qquad (9)$$

(b) For $\theta = 52$,

$$\Delta R_c = 2.8 \text{ m}, \qquad \Delta R_w = 81.78 \text{ m}, \qquad \text{and}$$

$$\Delta R_m = 84.58 \text{ m}$$

Note that

$$\Delta R_c = 2.8 \text{ m} < \Delta x = 156 \text{ m}$$

$$\Delta R_m = 84.58 \text{ m} < \Delta x = 156 \text{ m} \qquad (10)$$

From the above results, it follows that the range curvature of both high- and low-resolution imaging modes with $\theta = 25°$ and $\theta = 52°$ is less than the pixel spacing, and will be neglected. From Eqs. (9) and (10), the range migration is less than the pixel spacing for the low-resolution imaging mode. Thus, FFT techniques can be used to compute the real-time VOIR-SAR range correlation and azimuth correlation. From Eqs. (7) and (8), the range migration is greater than the pixel spacing for the high-resolution imaging mode.

III. Implementation of the Range Correlator

In order to compute the range correlation (Fig. 1), one needs to compute the number m of range points and the number ℓ of the pulse width points, for the low-resolution imaging mode. The number of range points is given by

$$m = f_s \frac{2x}{c} \sin \theta \qquad (11)$$

where f_s is a sampling frequency, x is a swath width, c is the speed of light. The number of pulse width or range filter points is given by

$$\ell = f_s \times \text{pulse length} \qquad (12)$$

Note that the values of the parameters in Eqs. (11) and (12) are given in Table 1.

For low-resolution imaging mode, we consider two cases:

Case 1: $\theta = 25°$, from (11) and (12),

$$m \cong 108 \text{ points}; \qquad \ell \cong 26 \text{ points} \qquad (13)$$

Case 2: $\theta = 52°$, from (11) and (12),

$$m \cong 252; \qquad \ell \cong 26 \text{ points} \qquad (14)$$

To use the FFT (Ref. 5) for implementing the range correlator, let

    a: input rate, samples/sec

R1, R2: m-point buffers, points

    n: length of the FFT, points

    T1: computation time to load *m* range data points into a buffer, sec

    T2: computation time of the range correlator using the *n*-point FFT, sec

    r: number of points of range after range correlation (each point is 4 bits)

A detailed design of a range correlator for the low-resolution imaging mode is given in Fig. 2. Its operation is accomplished as follows:

First, load *m* points of range data into *R1* buffer. The data are then passed to the range correlator for processing while buffer *R2* is being filled. Once the processing is completed in the range correlator, only $r = n - \ell + 1$ values become output. The process is repeated for data from buffer *R2*. Note that if $T2 < T1$, then the FFT can be used to compute one-dimensional range correlation. The time *T1* in Fig. 2 is given by

$$T1 = m/a \text{ sec} \qquad (15)$$

In order to use two FFTs and the pipeline technique to correlate the ℓ-point range filter with m-point input data, one needs to choose *n* such that $n \geqslant m$, where *n* is a power of 2. If the time for computing the *n*-point FFT is τ_n, then *T2* is given by

$$T2 = \tau_n \text{ sec} \qquad (16)$$

Case 1: For $\theta = 25°$, from Eq. (13), $m = 108$ and $\ell = 26$. Thus if one chooses $n = 128 > 108$, then the input rate for $\theta = 25°$ is given by

$$a = 108 \times PRF$$

$$= 108 \times 2180 \cong 236965 \text{ samples/sec}$$

where $PRF = 2180$ Hz is given in Table 1.

From Eq. (15) it follows that

$$T1 = \frac{1}{236965} \times 108 = 4.56 \times 10^{-4} \text{ sec} \qquad (17)$$

Since the JPL RFI Processor takes 6.4 μs and 12.8 μs to compute a 128-point and 256-point FFT respectively, by Eq. (17)

$$T2 = 6.4 \ \mu\text{sec} \qquad (18)$$

From Eqs. (17) and (18), one observes that $T2 < T1$. Hence, a 128-point FFT can be used to compute the range correlation for the real-time low-resolution image mode for $\theta = 25°$.

Case 2: For $\theta = 52°$, using the same procedure as in Case 1, one can show that $n = 256$ points, $T1 = 4.6 \times 10^{-4}$ sec and $T2 = 12.8 \ \mu\text{sec}$. Thus, $T2 < T1$. Hence, a 256-point FFT can be used to compute the range correlation for the real-time VOIR-SAR low-resolution image mode for $\theta = 52°$.

IV. Implementation of the Azimuth Correlator

In order to compute the azimuth correlation, one needs to compute the number k_a of points of the reference filter per look, for the low-resolution imaging mode. The number of points of the reference filter per look is given by

$$k_a = \tau_a \times PRF \qquad (19)$$

The total number of points of the reference filter for all looks is given by

$$k = Nk_a \qquad (20)$$

From the parameters given in Table 1, one can compute k_a and k for the low-resolution imaging modes as follows:

Case 1: $\theta = 25°$. From Eqs. (1a) and (1b),

$$R = \frac{300 \text{ km}}{\cos 25°} = \frac{300 \text{ km}}{0.906} = 331.13 \text{ km}$$

$$L_a = \frac{\lambda R}{2\Delta Z} = \frac{0.235 \times 331.13 \times 10^3}{2 \times 300} = 129.7 \text{ m}$$

$$\tau_a = \frac{L_a}{v} = \frac{129.7}{6.6 \times 10^3} \cong 0.019 \text{ sec}$$

$$k_a = \tau_a \times PRF = 0.019 \times 2180 = 41.42 \text{ points} \qquad (21a)$$

$$k = N \times k_a = 24 \times 41.42 \cong 994 \text{ points} \qquad (21b)$$

Case 2: $\theta = 52°$, from Eqs. (1a) and (1b)

$$k_a = 0.029 \times 2180 = 63 \text{ points} \qquad (22a)$$

$$k = 24 \times 63 = 1517 \text{ points} \qquad (22b)$$

To use the FFT for implementing the azimuth correlator, let

$M_i (1 \leqslant i \leqslant 3)$: memory to store the range lines for azimuth processing; capacity of each M_i for $i = 1, 2, 3$ is $k_a \times r$ complex data, or $k_a \times r$ bytes.

$A_i (1 \leqslant i \leqslant N)$: memory to store the output of azimuth correlator; capacity of each A_i is $(k_a/N) \times r$ real data or $(k_a/N)(r/2)$ bytes.

$T3$: time required to store k_a range lines into M_1 or M_2 or M_3.

$T4$: total computation time of the azimuth correlation of the $2k_a$ range lines and the k_a range filter of all looks.

The overlap-add FFT for computing multiple looks azimuth correlator is suggested by Wu (Ref. 6). For more detail see (Ref. 2). A detailed design of an azimuth correlator for the low-resolution imaging mode is given in Fig. 2. Figure 2 shows that a combination of the overlap-add FFT and pipeline technique can be used to implement the azimuth correlator for the real-time VOIR-SAR low-resolution imaging mode. To illustrate the processing described in Fig. 2, consider three looks for the reference filter, i.e., $N = 3$. The processing is composed of the following steps.

Step 1: The $2k_a$ range lines of complex data in M_3 and M_1 is passed to the azimuth correlator while the M_2 is being stored with k_a range lines of complex data. In the azimuth correlator, $2k_a$ range lines of input data are now convolved with the first look of k_a range lines of the reference filter. This can be performed by using an n-point FFT, where $n \geqslant 2k_a$. After performing the convolution of the third look, only k_a/N lines of real data (each line has r points) becomes output and is added into A_1 in the overlap-add processor. The processing is repeated for the second look of the reference filter while the

k_a/N image lines in A_1 are being read out. When the azimuth correlation is accomplished for the second look, the k_a/N output lines of real-data for the second look is added to A_2 in the overlap-add processor, while A_1 is set to zero. Finally, the processing is repeated for the first look reference filter. When the processing is accomplished, the k_a/N output lines of real data for the first look is added into A_3 in the overlap-add processor. It should be emphasized that timing considerations require all azimuth processing described in this step be completed before the k_a range lines are loaded into M_2, i.e., $T4 < T3$.

Step 2: When all k_a range lines are loaded into M_2, the $2k_a$ range lines of complex data in M_1 and M_2 are passed to the azimuth correlator while M_3 is being filled with the next k_a range lines. Using the same procedure as the azimuth correlator in Step 1, the $2k_a$ of range lines are correlated with the third, the second, and the first look sequentially. The k_a/N lines output of the third look is added to A_2. Then the k_a/N lines output of the second look is added to A_3 while the k_a/N image lines in A_2 are being read out. Finally, the k_a/N line output of the first look is added to A_1, while A_2 is set to zero.

Step 3: When all k_a range lines are loaded into M_3, the $2k_a$ range lines of complex data in M_2 and M_3 are passed to the azimuth correlator while M_1 is being filled with the next k_a range lines. Using the same procedure for azimuth correlation as in Step 1, the $2k_a$ of range lines are correlated with all looks of the reference filter sequentially. The k_a/N lines output of the third look is added to A_3. Then the k_a/N lines output of the second look is added to A_1 while the k_a/N image lines in A_3 are read out. Finally, the k_a/N lines output of the first look is added to A_2, while A_3 is set to zero. The processing is repeated for Step 1.

From the above procedure, one observes that if $T4 < T3$, then the FFT can be used to compute one-dimensional azimuth correlation for the real-time VOIR-SAR low-resolution imaging mode. To show this, one needs to compute the $T3$ and $T4$ as follows:

In order to use the FFT to correlate the k_a-point azimuth filter with $2k_a$ input data, one needs to choose n such that $n \geqslant 2k_a$, where n is a power of 2. To do this, we first take the n-point transform of input data, then multiply the transform of the input data by the transform of filter function. It can be shown that the transforms of the filter function have approximately 8 nonzero values for $\theta = 25$ and $\theta = 52$. Thus, the number of points in the product of the transform of input data and of the filter is 8. Since the k_a/N-point output of the correlation of the k_a-point filter and $2k_a$-point input data is needed to add into A_i, where $1 \leqslant i \leqslant N$, then each row of each of the N looks requires $15 \times k_a/N$ complex additions and

16 × k_a/N complex multiplications to accomplish the inverse transformation and complete the correlation. It follows from a current TRW multiplier specification sheet that the time required to compute either a 16-bit addition or multiplication should be between 100×10^{-9} and 200×10^{-9} sec. If one uses a parallel pipeline technique to compute the inverse transform, then $T4$ is

$$T4 \cong r \times \tau_n + N \times r \times 4 \times 200 \times 10^{-9} \qquad (23)$$

The time required to store the k_a range lines into M_1 or M_2 or M_3 is

$$T3 = k_a \times T1 \qquad (24)$$

where $T1$ is the computation time required to load m range data points into a buffer, as computed in Eq. (15).

Case 1: For $\theta = 25°$, from Eq. (13)

$$r = n - \ell + 1 = 108 - 26 + 1 = 83 \text{ points}$$

From Eq. (21a) we know $k_a = 41 \cong 48$. Thus

$$M_i = k_a \times r = 48 \times 83 = 3984 \text{ bytes for } 1 \leqslant i \leqslant 3.$$

Since $N = 24$, the $k_a/N = 48/24 = 2$ lines are output for each look. Thus,

$$A_i = k_a/N \times r/2 \cong 2 \times (83/2) \cong 83 \text{ bytes for } 1 \leqslant i \leqslant 24$$

From Eq. (24), it follows that

$$T3 = 48 \times 4.56 \times 10^{-4} = 218.88 \times 10^{-4} \text{ sec}$$

where $T1 = 4.56 \times 10^{-4}$ sec is given in Eq. (17). Since the time for computing a 128-point is 6.4 μsec, by Eq. (23)

$$T4 = 83 \times 6.4 \times 10^{-6} + 24 \times 83 \times 0.8 \times 10^{-6}$$

$$\cong 21.25 \times 10^{-4} \text{ sec}$$

Case 2: For $\theta = 52°$, from Eq. (14),

$$r = n - \ell + 1 = 252 - 26 + 1 = 227 \text{ points}$$

From Eq. (22a)

$$k_a = 63 \cong 72$$

Thus

$$M_i = k_a \times r = 72 \times 227 = 16344 \text{ bytes for } 1 \leqslant i \leqslant 3$$

Since $N = 24$, then $k_a/N = 72/24 = 3$ lines is output for each look. Thus

$$A_i = 3 \times 227/2 \cong 340 \text{ bytes for } 1 \leqslant i \leqslant 24$$

From Eq. (24), it follows that

$$T3 = 72 \times 4.6 \times 10^{-4} \cong 331.2 \times 10^{-4} \text{ sec}$$

where $T1$ is 4.6×10^{-4} for $\theta = 52°$ in Section III.

From Eq. (23),

$$T4 = 6.4 \times 10^{-6} \times 227 + 24 \times 227 \times 0.8 \times 10^{-6}$$

$$\cong 58.11 \times 10^{-4} \text{ sec}$$

In Case 1 and Case 2, one observes that $T4 < T3$. Hence a 128-point FFT can be used to compute the azimuth correlator for the real-time VOIR-SAR low resolution image mode for $\theta = 25°$ and $\theta = 52°$.

Acknowledgment

References

1. "VOIR-SAR System Design — 1978," Interim Report, Jet Propulsion Laboratory, 1978.

2. W. J. Van de Lindt, "Digital Technique for Generating Synthetic Aperture Radar Images," IBM J. Res. Develop., September 1977.

3. C. Wu, C. F. Leang, B. Barkan, and S. Pang, "An Introduction to the Interim Digital SAR Processor and the Characteristics of the Associated Seasat SAR Imagery," Interim Report, Jet Propulsion Laboratory, Pasadena, California, 1979.

4. K. Tomiyasu, "Tutorial Review of Synthetic-Aperture Radar (SAR) With Applications to Imaging of the Ocean Surface," Proceedings of the IEEE, Vol. 66, No. 5, May 1978.

5. E. O. Brigham, *The Fast Fourier Transform*, Prentice-Hall, Inc., Inglewood Cliffs, New Jersey, 1974.

6. C. Wu, "A Digital System to Produce Imagery From SAR," AIAA Systems Design Driven by Sensors, Pasadena, California, October 18-20, 1976.

Table 1. VOIR-SAR system characteristics

Altitude:	300 ± 25 km
Frequency:	1275 MHz
Antenna:	2.7 X 7.0 m planar array
Minimum radar cross section:	−30 dB at 0 dB SNR (over swath)
Peak output power:	100 W
Spacecraft speed:	6.6 km/s

	Low resolution		High resolution	
	Incident angle		Incident angle	
	25°	52°	25°	52°
Average power (W):	6		15	
Bandwidth (MHz):	0.8		4.75	
Pulse length (μsec):	28		47.5	
System ISLR (dB):	−13.6		−11.0	
Quantization bits:	5		3	
Maximum data rate (Mbps):	3.20		7.20	
Number of looks:	24		8	
Resolution (range & az):				
Line pair (m):	600/600	1150/600	100/100	200/100
Radar (m):	300/300	575/300	50/50	100/50
Pixel (m):	180/180	345/180	30/30	60/30
Swath width (km):	50	40	12	12
Dynamic range (dB):	30	37	17	21
Noise eq. σ_o (best) (dB):	−37	−45	−32	−39
PRFs (Hz):	5 from 1923 to 2180		5 from 2835 to 3165	

RAW DATA

FFT

RANGE
TRANSFER
FUNCTION

FFT^{-1}

RANGE CORRELATOR

CORNER
TURNING

FFT

AZIMUTH
TRANSFER
FUNCTION

FFT^{-1}

AZIMUTH CORRELATOR

$| \quad |^2$

IMAGES
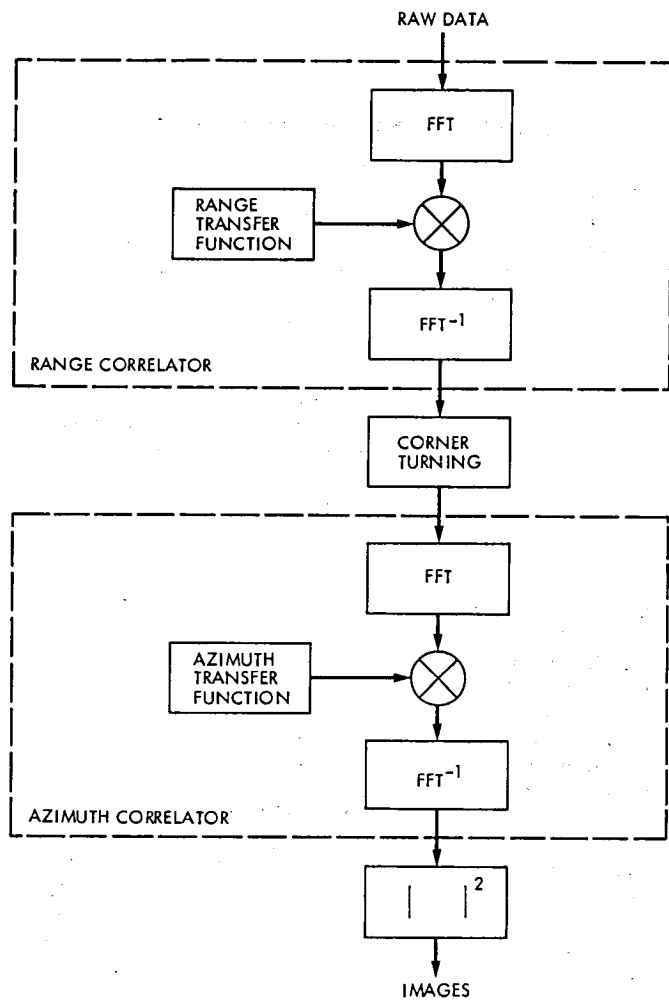
Fig. 1. A block diagram of the FFT-SAR data processing
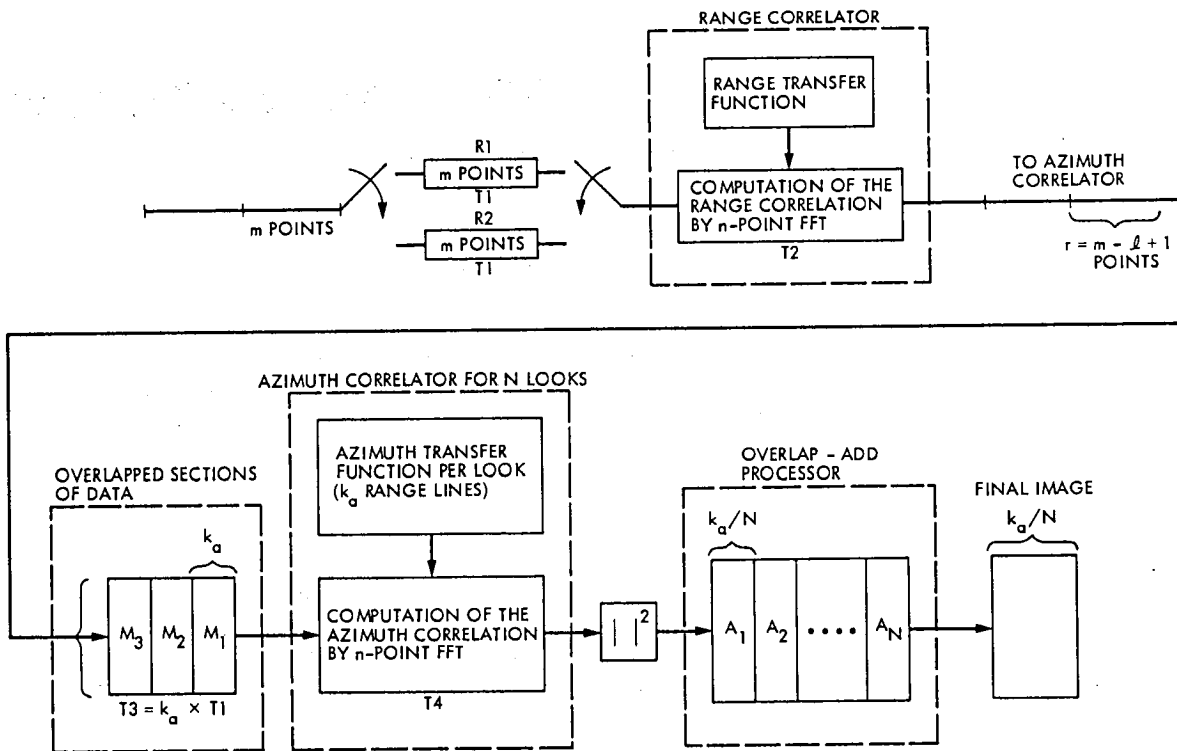
Fig. 2. A flowchart of the range and the azimuth correlator for the real-time low-resolution SAR-VOIR imaging mode by using an FFT method

Feasibility and Cost Study on VOIR SAR Data Transfer via a Bent Pipe Link

Y. H. Park and A. M. Goldman, Jr.
Telecommunications Systems Section

An INTELSAT/DOMSAT double-hop bent pipe link for the VOIR (Venus Orbiting Imaging Radar) SAR (Synthetic Aperture Radar) imaging data transfer from DSS 43 and 63 to JPL is investigated. The cost for the bent pipe transfer is estimated and compared to that for the presently planned tape-record/airfreight-the-tape transfer method. This study is based on the mission plan available in May 1979.

I. Introduction

This article summarizes the result of a study on the relative costs of two methods for the VOIR (Venus Orbiting Imaging Radar) SAR (Synthetic Aperture Radar) data transfer from overseas Deep Space Stations (DSS) to Goldstone or JPL. The present plan is to tape-record the SAR data at DSS 14, 43 and 63 and then to airfreight the tapes to JPL. The other method is to transfer the SAR data from the overseas stations to Goldstone or JPL via a bent pipe link (an INTELSAT/ DOMSAT link) and then to tape-record the data at either Goldstone or JPL.

The bent pipe concept for the overall DSN data transfer has been studied at JPL and a bent pipe system study for the Galileo/IUS (third stage) is also available. However, this study is conducted with emphasis on the comparison of the relative costs for the bent pipe and the presently planned tape-record/ airfreight method of VOIR SAR data transfer.

The results contained in this article are based on the VOIR mission plan available in May, 1979. Throughout the article, the maximum SAR data rate of 7.33 Mbps is assumed instead of 1 Mbps data rate of a new reduced scope mission plan.

One of the original objectives of this study was to examine the possibility of eliminating the digital tape-recording requirement at the overseas stations, since the trend at DSN stations is toward unattended operation. Also, the quality control of the high-capacity digital tape-recorder operation may be improved at a central point, i.e., at JPL or Goldstone. However, the study indicated that the cost of the bent pipe method exceeds that of the tape-record/airfreight method by approximately a factor of 10.

In Section II, the presently planned data transfer method and its cost estimate are discussed. In Section III the characteristics of the INTELSAT/DOMSAT double-hop links and the implementation cost are presented. In Section IV, the two data transfer methods are compared.

II. Planned VOIR SAR Data Transfer

In this section, the presently planned VOIR SAR imaging data transfer method is described and its cost estimate is presented.

A. Planned Strategy

The SAR imaging data is transmitted to DSS 14, 43, or 63. In this study, it is assumed that the SAR data has the maximum data rate of 7.33 Mbps and is convolutionally encoded with a rate 1/2 and constraint 7 code. The SAR data on the X-band suppressed carrier BPSK signal will be demodulated by a Costas loop to be incorporated into Block III or IV DSN receivers. This modification will be part of the Multimegabit Telemetry Demodulator-Detector (MTDD) System.

The noisy SAR data symbol streams will be detected by a Symbol Synchronizer Assembly (SSA) and then decoded by a Maximum Likelihood Convolutional Decoder (MCD). The decoded data will be tape-recorded by the Digital Recording Assembly (DRA). The tapes then will be transported to the JPL mission support area. This procedure is shown in Fig. 1.

B. Cost Estimation

The estimated cost of the presently planned VOIR SAR data transfer is summarized in Table 1.

In this estimate, the items required for both methods of data transfer are excluded since our objective is really to determine the cost differential between the two methods. For example, the cost for tapes, implementation of the MTDD System and the basic DSN operation and maintenance costs are not considered. Thus, the cost estimate shown in Table 1 consists of the tape-recording cost and the delivery cost.

The decoded SAR data will be tape recorded through the DRA. The DRA can be operated at various speeds. Typically, 15 inches per second (ips) will be used here for cost estimation purposes. At a speed of 15 ips, the DRA can record data up to an 8 Mbps rate. A typical tape to be used is 0.5 in. wide and mounted on a 16-in.-diameter reel which contains 12,500 ft of tape. The approximate weight of the tape is 5 lb. The tape can record for approximately three hours at 15 ips.

The DRA has to be upgraded to support future high rate data return requirements such as the SAR data link from the VOIR. The upgrading cost for three DRA's (one each at DSS 14, 43 and 63) is approximately $75,000. The DRA tape recorder head should be replaced after every 3,000 hr of operation at 15 ips. The cost estimate is for one replacement per year at each DSS. Eight hours of DRA operation per day is assumed. The cost includes one new recording head ($6,000) and new reproducing head ($7,000) at each DSS. The DRA maintenance and operations costs are based upon normal operation. Assumptions for these cost estimates are indicated in Table 1.

At DSS 43 and 63, it is assumed that three tapes per day will be recorded. The tapes will be delivered to the nearest international airport and sent by commercial airline airfreight to Los Angeles (LAX). The delivery cost between an overseas DSS and an international airport is included in the item "other manpower" in Table 1.

III. Bent Pipe Data Transfer

The bent pipe link under consideration is a link from the VOIR to either DSS 43 or 63 and then from DSS 43 or 63 via an INTELSAT/DOMSAT double-hop link to Goldstone or JPL. A general bent pipe link description, possible subsystem interfaces in the link and cost estimate are discussed in this section.

A. Bent Pipe Link Description

The VOIR SAR data is transmitted on an X-band downlink carrier with suppressed carrier BPSK modulation. The signal is received by Block III or IV receivers at DSS 43 and 63. Then it is processed by a Symbol Synchronizer Assembly (SSA) and Maximum Likelihood Convolutional Decoder (MCD). The decoded data should be transmitted to either an existing INTELSAT Earth terminal or to a new INTELSAT Earth terminal on the DSS 43 or 63 site. The link from DSS 43 or 63 to an existing INTELSAT Earth terminal may be either a microwave link or a coaxial cable. The data may be QPSK-modulated to reduce BPSK signal bandwidth in half before transmitting it to the INTELSAT spacecraft. The data is usually modulated onto the standard 70 MHz IF carrier. Generally, frequency division multiple-access (FMDA) is used for the access of the INTELSAT transponder.

The INTELSAT IV or IVA spacecraft uplink uses a nominal 6-GHz carrier frequency, and the downlink has a nominal 4-GHz carrier frequency. For INTELSAT V, both 6/4 and 14/11 GHz links will be available. The signal from DSS 43 or 63 via INTELSAT is received in an INTELSAT U.S. gateway Earth terminal. Generally it is downconverted to the 70-MHz IF frequency and transmitted to a nearby DOMSAT Earth terminal via a microwave link or coaxial cable. Collocation for an INTELSAT U.S. gateway Earth terminal and a DOMSAT Earth terminal will be discussed later. The ground communications links at the U.S. gateway stations are similar to those discussed above.

The signal from a DOMSAT may be received at either Goldstone or JPL. A new DOMSAT Earth terminal is required at Goldstone or JPL. The signal received at the DOMSAT Earth terminal at Goldstone may be demodulated, decoded and tape recorded at Goldstone. Another option would be to transmit the signal to JPL via a microwave link and then

process and record it at JPL. The various options for the receiving end point of the bent pipe link will be discussed in Section III F. However, for this study the last option is assumed. The bent pipe route is described in Fig. 2.

B. Interface Between DSS and INTELSAT Earth Terminal

Since the distance from DSS 43 or 63 to the nearest INTELSAT Earth terminal is an important factor for cost estimation, the locations of Earth terminals are discussed here.

The locations of DSS 43 and DSS 63 are listed in Table 2. The existing Pacific INTELSAT Earth terminal closest to DSS 43 is located near Moree, Australia, north of Sydney. The nearest INTELSAT Earth terminal to DSS 63 is located in Buitrago, Spain, about 50 miles north of Madrid. Geodetic latitude and longitude of these INTELSAT Earth terminals are listed in Table 3. The "airline" distance from the DSS 43 to Moree is approximately 368 nmi and that from DSS 63 to Buitrago is approximately 50 nmi.

Figure 3 describes a possible configuration of subsystems at DSS 43 and 63. The VOIR SAR data is received and demodulated by a Block III or IV receiver. For the planned suppressed carrier transmission of SAR data, the Block III/IV receiver is planned to include a Costas loop.

The demodulated signal is fed to a SSA and then to the MCD. One of the advantages of demodulating, detecting and decoding at DSS 43 or 63 is the possibility of retransmitting the data using a QPSK signal format in the INTELSAT and DOMSAT links. Since the VOIR X-band telemetry data will be convolutionally encoded with rate 1/2 code, the data transmission bandwidth in the satellite links can be further reduced to one-fourth using decoding and QPSK modulation for the satellite links. The demodulated data is remodulated onto the standard 70-MHz INTELSAT IF.

If the DSS and the INTELSAT Earth terminal are not collocated, the modulated IF signal (70 MHz) is upconverted to a microwave carrier frequency and transmitted to a receiver located close to an INTELSAT Earth terminal. The received signal is downconverted to the 70 MHz IF frequency which can be easily interfaced with the INTELSAT Earth terminal equipment. Since the decoded data rate varies from a maximum of 7.33 Mbps to less than 4 Mbps for most of the nominal VOIR mission period, many off-the-shelf microwave link components are available for the VOIR SAR data transfer.

Unless new INTELSAT Earth terminals are constructed at the DSS 43 and 63 sites, new microwave links should be installed from DSS 43 to the existing Moree INTELSAT Earth terminal and from DSS 63 to the existing Buitrago INTELSAT

Earth terminal. From DSS 43 to Canberra, a new wideband microwave link would have to be installed by Australian Public Telephone and Telegraph (PTT) authorities. This new microwave link would have to interface with existing television bandwidth microwave links from Canberra to Sydney to Moree. From DSS 63 to Madrid, a new wideband microwave link would have to be installed by Spanish PTT authorities. This would interface with existing television bandwidth microwave links from Madrid to Buitrago. However, it may be less complicated from a regulatory sense as well as more cost-effective to collocate new INTELSAT Earth terminals at DSS 43 and 63 sites. However, the Australian and Spanish authorities would have to agree to this.

C. INTELSAT Space Link

In 1985, two INTELSAT IV-A (F-3 and F-6) will be available in the Pacific region, and four INTELSAT V will be available in the Atlantic region. These INTELSAT's may be utilized for the bent pipe transfer of the VOIR SAR data in 1985. However, some of the "retired" INTELSAT IV and IVA may be reactivated for the period of the VOIR mission.

For the transmission of VOIR SAR data through an INTELSAT link, a QPSK/FDMA mode is desirable. With QPSK/FDMA mode transmission, approximately 9 MHz of the typical 36-MHz bandwidth of a transponder is required.

D. Interface Between INTELSAT and DOMSAT Link

The VOIR data from DSS 43 in Australia can be transferred via a Pacific INTELSAT satellite and can be received at a west coast INTELSAT U.S. gateway Earth terminal such as Jamesburg, California. Even though there is no DOMSAT Earth terminal presently in Jamesburg, the American Satellite Corporation (ASC) may install a collocated Earth terminal there. Thus, collocated INTELSAT and DOMSAT Earth stations at Jamesburg are assumed for the remainder of this article.

The VOIR SAR data from DSS 63 in Spain can be transferred via an Atlantic INTELSAT satellite and received at U.S. gateway Earth terminals at Andover, Maine, or Etam, West Virginia. At these locations, there exist ASC DOMSAT Earth stations which presently access the WESTAR domestic satellite.

The INTELSAT satellite downlink carrier frequency is received at one of the U.S. gateway Earth terminals and then downconverted to a standard 70-MHz IF. The IF signal, after a frequency upconversion, is then transmitted through a very short terrestrial microwave link. At the nearby DOMSAT Earth terminal, the received microwave carrier is again

downconverted to a 70-MHz IF. After another frequency upconversion, the carrier is retransmitted to a DOMSAT satellite. This is illustrated in Fig. 4.

E. DOMSAT Space Link

Currently available domestic satellites are the Western Union WESTAR, the RCA SATCOM and the COMSAT/AT&T/GTE COMSTAR. In 1980, Advanced WESTAR by Western Union and SBS by Satellite Business Systems also will be available. All systems except SBS use the 6/4 GHz C-band; the SBS and a portion of the Advanced WESTAR systems will utilize 14/11 GHz K_u-band.

The bandwidth requirement for a DOMSAT transponder is also approximately 9 MHz, which is a quarter of a 36-MHz transponder when a QPSK/FDMA transmission method is used.

F. Receiving End Point, Goldstone or JPL

The receiving point for the bent pipe depends on where the demodulation, detection and the tape recording of the VOIR SAR data are performed. The different options are as follows:

(1) The received signal at a new Goldstone DOMSAT Earth terminal from DSS 43/63 via the INTELSAT/DOMSAT link is frequency converted and retransmitted to JPL via a terrestrial microwave link. The tape recording is then performed at JPL. The received signal from DSS 14 is also frequency converted and retransmitted via the same terrestrial microwave link and then tape recorded at JPL where signal processing takes place.

(2) This option is the same as (1) above except that another DOMSAT link is used between Goldstone and JPL instead of the terrestrial microwave link.

(3) A new DOMSAT Earth terminal is installed at JPL instead of at Goldstone. The existing RCA SATCOM Earth terminal at JPL might be used if allowed.

(4) A new DOMSAT Earth terminal is installed at Goldstone as an option (1), but tape recording is performed at Goldstone. The tapes are then transported to JPL via automobile for signal processing.

(5) This option is the same as (4) above except that the signal processing facility would be established at Goldstone, removing the need to transport tapes to JPL.

In this report only option (1) will be used as a guideline for cost estimation.

G. Cost Estimation

The cost estimate for the INTELSAT/DOMSAT double-hop bent pipe method is based on the model described in Section III-A. Some of the critical assumptions for the cost estimate are as follows:

(1) Demodulation, detection and decoding are performed at each DSS.

(2) 9 MHz of bandwidth, i.e., a quarter of a 36-MHz satellite transponder, is assumed. This bandwidth is estimated to be necessary for the maximum VOIR SAR data rate of 7.33 Mbps, with a possible convolutional encoding in the INTELSAT/DOMSAT channel with a 7/8 rate and some guard band allowance to protect against intermodulation interference.

(3) The cost estimate for the data transfer from an overseas DSS to an INTELSAT Earth terminal is not included here. As discussed before, there are two options. The first option is to use a terrestrial microwave link from each overseas DSS to the nearest existing INTELSAT Earth terminal. The other option is to install an on-site INTELSAT Earth terminal at each overseas DSS. In either option, the cost may be a significant part of the total bent pipe cost.

(4) A DOMSAT Earth terminal at Goldstone is assumed.

(5) The VOIR SAR data from DSS 14, 43 and 63 will be tape recorded at JPL where signal processing takes place.

(6) A megabit rate terrestrial microwave link from Goldstone to JPL is assumed. The cost estimate for this microwave link is based on a 5-Mbps simplex line.

With the assumptions stated above, the cost estimates for the bent pipe method are summarized in Table 4.

IV. Discussion and Conclusion

This study provides a cost comparison between the planned and bent pipe VOIR SAR data transfer methods. Even though some cost estimates are crude, the cost ratio is at least 5-to-1, with the bent pipe costs being highest. Depending on the TBD costs, the ratio could go up to 10-to-1. Table 5 summarizes the relative costs for the two methods.

Even though the communication satellite link costs have been steadily decreasing in past years, the bent pipe method for the VOIR SAR data transfer does not seem to be cost-effective at the present time. However, it should be noted that the cost of the planned method is expected to increase

slowly in time, while the cost of the bent pipe method will almost surely decrease in the future.

This cost study is based upon a maximum 7.33 Mbps data rate for VOIR. However, it is expected that for most of the time, the data rate could be in the range of 1 Mbps, more or less continuously. Thus, with some ingenious Time-Division-Multiple-Access (TDMA) store-and-forward burst uplink from the DSS to the satellite, the cost could be shared with other NASA missions or with other users. It seems that a bent pipe should be studied in the context of several NASA missions rather than a single mission. Also, any requirements for totally unattended overseas DSS operations and/or real-time data transfer to JPL may reduce the relative cost of the bent pipe. Hence it would appear to be worthwhile to continuously monitor the relative costs of a bent pipe in the future.

Table 1. Cost for recording and tape transfer

	6 mo, $ × 10^3	1 yr, $ × 10^3	Remarks
Digital recording assembly upgrade (DSS 43, 63, 14)	75	75	
Tape recorder head (DSS 43, 63, 14)	Not required	39	1 replacement/DSS
Maintenance (DSS 43, 63, 14)	8	16	5 man hr/week/DSS $20/man hr
Operation (DSS 43, 63, 14)	88	175	8 man hr/day/DSS $20/man hr
Tape delivery			
DSS 43 → LAX			
Airfreight	5	10	
Other manpower	8	17	16 man hr/week $20/man hr
DSS 63 → LAX			
Airfreight	3	5	
Other manpower	8	17	16 man hr/week $20/man hr
DSS 14 → JPL	8	17	16 man hr/week $20/man hr
LAX → JPL	8	17	16 man hr/week $20/man hr
Subtotal	211K	388K	

Table 2. Locations of the 64-meter Deep Space Stations

Station	Location	Latitude, deg	E. Longitude, deg
DSS 14	Goldstone, California	35.426	243.111
DSS 43	Ballima, Australia (near Canberra)	−35.404	148.980
DSS 63	Robledo, Spain (near Madrid)	40.434	355.753

Table 3. Locations of INTELSAT Earth terminals near DSS 43 and DSS 63

INTELSAT Earth terminal		Latitude, deg	E. Longitude, deg
Moree, Australia	North of Sydney	29° 20'	149° 50'
Buitrago	50 miles north of Madrid	41° 0'	356° 20'

Table 4. Cost for VOIR bent pipe data transfer

Transfer link	$/mo × 10^3	Total for 6 mo, $ × 10^3	Total for 1 yr, $ × 10^3	Remarks
DSS 43 – INTELSAT Earth terminal	TBD	TBD	TBD	
DSS 63 – INTELSAT Earth terminal	TBD	TBD	TBD	
INTELSAT Link				
Australia – U.S. Gateway	42	250	500	Estimated costs for 9 MHz B.W.
Spain – U.S. Gateway	42	250	500	
DOMSAT Link				
U.S. Pacific Gateway – Goldstone	31	186	372	For 9 MHz B.W.
U.S. Atlantic Gateway – Goldstone	31	186	372	
Earth terminal at Goldstone				
Installation	15	15	15	Standard B (10-m) terminal
User charge	15	90	180	
M/W Link, Goldstone – JPL				
Installation	•	175	175	Estimated costs for 5 Mbps simplex
User charge	35	210	420	Termination charges $170,000 amortized over
Termination charge	•	153	136	60 months
Total[a]	•	1,515 +TBD[b]	2,670 +TBD[b]	

[a]The total cost does not include the tape-recording cost at JPL.

[b]TBD cost is in the range of $1 million.

Table 5. Cost summary for VOIR SAR data transfer from DSS 14, 43, and 63 to JPL

	6 mo, $ × 10^3	1 yr, $ × 10^3	Remarks
Currently planned tape recording and airfreight data transfer method	211	388	Includes the planned DRA upgrade cost
Possible VOIR SAR data bent pipe transfer method	1,515 +TBD	2,670 +TBD	Utilize INTELSAT/ DOMSAT double-hop links from DSS 43 and 63 to Goldstone Include terrestrial microwave link from Goldstone to JPL TBD costs are significant
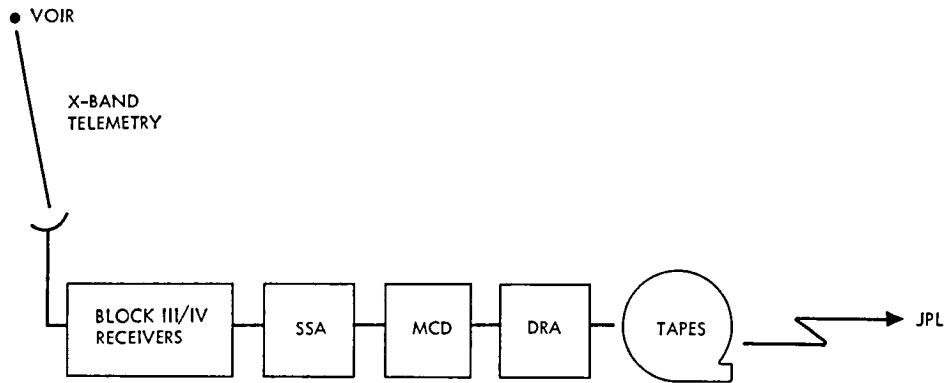
Fig. 1. The planned SAR data transfer strategy

VOIR

X-BAND
TELEMETRY

BLOCK III/IV
RECEIVERS → SSA → MCD → DRA → TAPES → JPL

VOIR

INTELSAT IV
IV-A
V

DOMSAT
(WESTAR
SATCOM
COMSTAR
SBS
ADV. WESTAR)

DSS 43   *MOREE, AUSTRALIA   ** JAMESBURG, CA.   GOLDSTONE   JPL
                                  *** ANDOVER, ME.
DSS 63   *BUITRAGO, SPAIN   *** ETAM, W.V.

* LOCATIONS OF THE EXISTING INTELSAT EARTH TERMINAL
** A COLLOCATED DOMSAT ET IS PLANNED BY THE AMERICAN SATELLITE CORP.
*** INTELSAT ET AND ASC ET ARE COLLOCATED

Fig. 2. Bent pipe route

X-BAND RATE 1/2 CONVOLUTIONALLY
ENCODED SAR DATA FROM VOIR

(1)	(1)	(1)	(2)
BLOCK III OR IV RECEIVER	SSA	MCD	QPSK MODEM

70 MHz IF

TO INTELSAT

(3)

| IF INPUT | UP-CONVERTER & XMTR | | DOWN-CONVERTER & RECEIVER | 70 MHz IF OUTPUT | | INTELSAT ET |

MW LINK (3)

(1) PART OF THE PLANNED MTDD
(2) NEW EQUIPMENT
(3) NEW OR EXISTING EQUIPMENT

Fig. 3. Subsystems at DSS 43/63

FROM
INTELSAT

TO
DOMSAT

| INTELSAT ET | 70 MHz | IF INPUT | MICROWAVE UP-CONVERTER & XMTR | | MICROWAVE DOWN-CONVERTER & RCVR | IF OUTPUT | | DOMSAT ET |

JAMESBURG, CA. (A DOMSAT ET IS PLANNED)
ANDOVER, ME.
OR
ETAM, W.V.

Fig. 4. INTELSAT/DOMSAT Interface

Spatial Acquisition of Optical Sources in the Presence of Intense Interference

V. A. Vilnrotter

Telecommunications Systems Section

The problem of spatially acquiring an optical beacon in the presence of intense optical interference is considered. It is demonstrated that conventional acquisition procedures cannot establish acceptable levels of acquisition probability when competing with strong optical interference, without requiring unreasonable amounts of prime power. As a possible solution, it is shown that a more sophisticated acquisition scheme can virtually eliminate the effects of optical interference, while requiring only a modest increase in system complexity.

I. Introduction

The problem of spatially acquiring an optical source in the presence of optical interference is considered. The spatial acquisition of the uplink beacon by a deep-space vehicle (DSV) is a necessary prerequisite to optical downlink transmission (Ref. 1). Similarly, a near-Earth optical relay receiver must acquire the downlink beam before it can decode the transmitted data, or relay it to the ground for decoding. Prior to spatial acquisition, the angular uncertainty in the location of the beacon tends to be considerable (on the order of 10^{-8} steradians or more at the DSV). Consequently, the illuminated Earth, and possibly the Moon, might be included within the initial uncertainty region, along with the desired optical source. For the case of the relay receiver attempting to locate the DSV, the target planet (Jupiter, Saturn, etc.) is likely to be included in the initial uncertainty field-of-view. These extraneous optical sources interfere with spatial acquisition, and in extreme cases, may even cause the acquisition (and subsequent tracking) of the wrong source. In the following sections we develop a model for the problem of acquiring the desired optical source (henceforth termed the "beacon") in the presence of a single interfering source. We shall demonstrate that while straightforward acquisition schemes invariably fail in the presence of intense interference, more sophisticated procedures can yield vast improvements in acquisition performance.
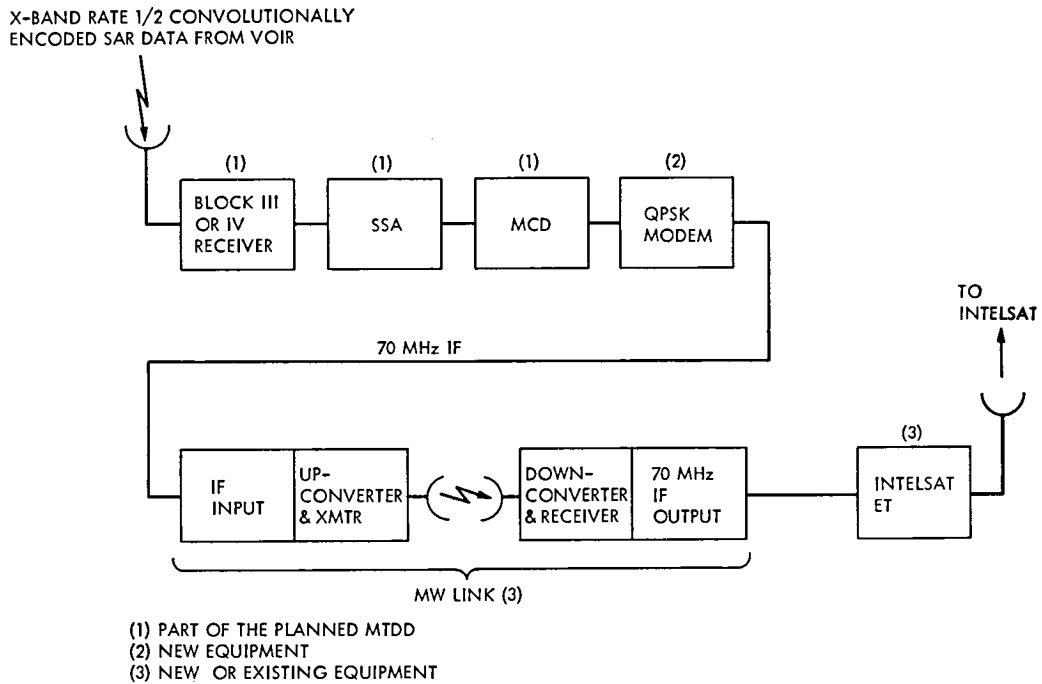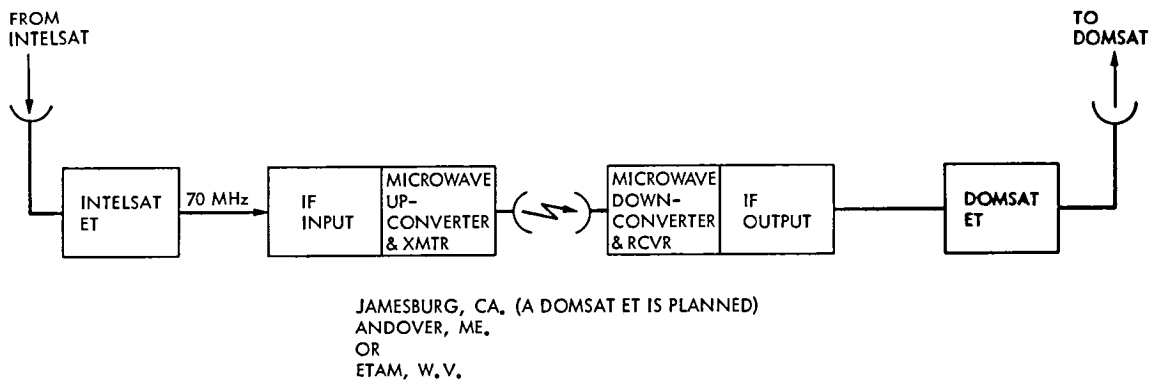
II. The Spatial Acquisition Problem

The problem of acquiring an optical source in the presence of interference can be described by referring to Fig. 1. The angular uncertainty region is assumed to be encompassed by a square solid angle of Ω_u steradians, roughly θ_u degrees on a side. It is desired to resolve the angular position of the optical beacon to within Ω_r steradians. Therefore, we can partition the uncertainty region into $M = \Omega_u/\Omega_r$ resolution cells, each cell θ_r degrees on a side, and search the resulting matrix of resolution cells to locate the beacon source.

The derivation of the acquisition probability is straight-forward when both uniform background radiation and point-source interference are absent. Assuming the count-intensity of the beacon is n_s photoelectrons/second, the average number of photoelectrons generated in T seconds by a photodetector (whose active area corresponds to the dimensions of the appropriate resolution cell) is $K_s = n_s T$, while the average count generated over all other resolution cells is identically zero. Invoking the majority-count decision rule (Ref. 2), correct acquisition occurs if the optical source generates at least one count over the proper resolution cell. Assuming that the counts are Poisson distributed, the acquisition probability for this ideal case, PAC^*, becomes

$$PAC^* = 1 - \exp(-K_s) \qquad (1)$$

This upper bound on the acquisition probability is shown in Fig. 2. Note that an average of at least 2.3 counts is required per observation interval in order to maintain better than 90 percent probability of acquisition, even in the absence of external interference.

Next, we consider the acquisition problem when a single interfering source is included in Ω_u, along with the desired optical source. (The extension to more than one interfering source is straightforward, but computationally tedious.) The interference is assumed to be far enough removed from the desired source (and small enough in angular extent) to excite a different resolution cell, inducing a count-intensity of n_i photoelectrons/second, hence an average observed count of $K_i = n_i T$ photoelectrons over that resolution cell. The resolution cell with the greatest number of observed counts is selected. Correct acquisition takes place if the beacon generates more counts than the interference: that is, if $k_s > k_i$. In case of a tie, the search is repeated (Ref. 2). The probability of correct acquisition, PAC, can therefore be expressed as

$$PAC = \sum_{k_s=1}^{\infty} \frac{K_s^{k_s}}{k_s!} e^{-k_s} \left[\sum_{k_i=0}^{k_s-1} \frac{K_i^{k_i}}{k_i!} e^{-K_i} \right] \qquad (2)$$

$$= \sum_{k_s=1}^{\infty} \frac{K_s^{k_s}}{k_s!} e^{-K_s} \left[1 - \frac{\gamma(k_s, K_i)}{(k_s - 1)!} \right]$$

where

$$\gamma(\alpha, x) \overset{\Delta}{=} \int_0^x e^{-t} t^{\alpha-1} dt; \quad Re\alpha > 0.$$

The exact computation of PAC is hindered by the infinite summation in Eq. (2). However, the truncated acquisition probability, PAC_T, can be computed for any finite summation limit δ, where

$$PAC_T = \sum_{k_s=1}^{\delta} \frac{K_s^{k_s}}{k_s!} e^{-K_s} \left[1 - \frac{\gamma(k_s, K_i)}{(k_s - 1)!} \right] \qquad (3)$$

Defining the truncation error E_T as

$$E_T = \sum_{k_s=\delta+1}^{\infty} \frac{K_s^{k_s}}{k_s!} e^{-K_s} \left[1 - \frac{\gamma(k_s, K_i)}{(k_s - 1)!} \right] \qquad (4)$$

we observe that since $E_T > 0$ for all finite δ,

$$PAC = PAC_T + E_T \geqslant PAC_T \qquad (5)$$

for all δ.

The truncated acquisition probability, PAC_T, therefore lower bounds the actual value of PAC. It is shown in the Appendix that E_T can be made negligibly small by letting $\delta + 1 = \zeta K_s$, $\zeta > 0$, and selecting a sufficiently large value for ζ. Having computed PAC_T under the above constraint, we shall henceforth let $PAC_T \simeq PAC$.

Figure 2 shows the behavior of PAC as a function of K_s for increasing values of the average interference-induced count, K_i. It is apparent that weak interference ($K_i \ll K_s$) has no appreciable effect on the acquisition probability. However, PAC deteriorates rapidly in the presence of strong interference ($K_i \geqslant K_s$). One rather obvious solution to the interference problem is therefore to increase the source power until n_s becomes much greater than n_i, while holding the observation time constant. Unfortunately, this solution may not always be practical, due to the increased power consumption required.

If the beacon and interference count-intensities are comparable, but $n_i < n_s$, then PAC can be improved by increasing the observation interval, as shown in Fig. 3. Here we define α as the ratio of interference-rate to beacon-rate, $\alpha = n_i/n_s$. When $\alpha < 1.0$, PAC shows some improvement with increasing T, although the rate of improvement decreases as α approaches unity. For $\alpha = 1$, the acquisition probability cannot be improved by increasing T, while for $\alpha > 1$, increasing the observation time leads to a catastrophic degradation in acquisition performance. This behavior is clearly illustrated by the curves corresponding to $\alpha = 2$ and $\alpha = 4$ in Fig. 3.

We have shown, therefore, that it becomes difficult to achieve high acquisition probabilities by increasing the source power or the observation time, in the presence of intense interference. Some additional advantage may be gained by a combination of the two techniques, that is, by increasing the source power to drive α below unity, and simultaneously increasing the observation time. In the next section, we shall demonstrate a somewhat different acquisition technique that virtually eliminates the interference problem in acquisition systems, without incurring significant penalties in terms of system complexity.

III. Spatial Acquisition of Pulsed Optical Sources

We have seen that strong optical interference can impede the spatial acquisition of the desired optical source. The difficulty is that with strong interference, the interfering counts k_i can, with high probability, exceed the beacon counts k_s, resulting in false acquisition. We propose to alleviate this problem by reducing the observation time in order to decrease K_i, while keeping K_s the same. This can be accomplished by pulsing the beacon laser and simultaneously transmitting the required timing information to the DSV over a separate RF channel. The requirement to transmit timing information to the DSV should not overburden the RF uplink, since optical acquisition is inherently a relatively short-duration operation.

We now assume that the beacon laser generates a periodic pulse-train, while maintaining constant average power. The received pulse-train can, therefore, be represented as in Fig. 4. The photoelectrons generated at the DSV by the beacon now appear concentrated in narrow, high count-intensity pulses of duration τ'-seconds, at regular T'-second intervals. Defining the pulse-compression factor γ as $\gamma = T'/\tau'$, we observe that if the beacon count-rate is constrained to be γn_s photoelectrons per second, then the average beacon count-rate remains n_s photoelectrons/second, thus maintaining constant average received power as required. As before, the interference count-rate remains n_i photoelectrons/second, uniformly distributed in time. The timing information can be used to define τ-second observation windows around each τ'-second pulse. Note that while the minimum value of τ is τ', this limit can only be achieved with perfect timing. In general, the duration of the observation-window τ would be much greater than τ' in order to mask the effects of timing uncertainties. With little loss in generality, we shall argue that N pulses have to be observed in order to maintain the previously defined average signal count, K_s. Therefore, the average counts due to beacon and interference in the pulsed system become

$$K_s^p = N \gamma n_s \tau' = n_s T \qquad (6a)$$

$$K_i^p = N n_i \tau \qquad (6b)$$

We observe that the reduction in K_i^p over K_i depends directly on the ratio τ/T', which is, in turn, related to the accuracy of the timing information transmitted to the DSV. Defining the observation-compression factor β as $\beta = T'/\tau$, we can express the average interference counts in the pulsed system, K_i^p, in terms of K_i, as $K_i^p = K_i/\beta$. The interference-suppression capability of the pulsed system is, therefore, determined by the system-parameter β. (With present-day Q-switching technology and current DSN capabilities, maximum values of β on the order of a few hundred appear feasible.)

The improved performance of the pulsed system is clearly shown in Fig. 5, which shows the acquisition probability PAC as a function of β at the fixed value $K_s = 5$, for various K_i corresponding to high-intensity interference. (The upper-bound on acquisition probability, $PAC^* = 0.9933$, is also shown for comparison.) Figure 5 should be compared with Fig. 2 (at $K_s = 5$) for a direct measure of the improvement provided by the pulsed system. Without pulsing (that is, $\beta = 1$) the acquisition probability corresponding to $K_s = 5$ and $K_i = 10$ is $PAC = 0.074$, while even modest compression ratios ($\beta > 20$) yield $PAC \gtrsim 0.98$. With improved timing ($\beta > 100$) reasonable acquisition probabilities can be obtained, even in the presence of extremely intense interference, as demonstrated by the curves corresponding to $K_i = 20, 50$ and 100 in Fig. 5. Similar improvements over continuous intensity systems can be demonstrated at other values of K_s as well.

We have seen that in the presence of strong interference, acquisition probabilities can be improved either by increasing the average beacon power, or by pulsing the beacon (with a constant average power constraint) and relying on timing information transmitted in a separate channel to reduce the interfering counts. These techniques tend to increase system cost and complexity; therefore it may become desirable to employ a combination of both techniques in order to improve acquisition performance. Figure 6 shows graphs of constant PAC over the (β, K_s) plane. Each graph represents the locus of points corresponding to a constant acquisition probability in the presence of interference. It is apparent by a direct extension of these results that for any interference level K_i, a continuum of points can be found in the (β, K_s) plane to achieve any desired level of PAC. The two system parameters β and K_s can therefore be traded off on the basis of cost and complexity while maintaining the required level of acquisition performance.

Appendix

The truncation error E_T defined in Eq. (4) can be upper bounded by E_T^u, as shown by the following inequality:

$$E_T = \sum_{k_s = \delta + 1}^{\infty} \frac{K_s^{k_s}}{k_s!} e^{-K_s} \left[1 - \frac{\gamma(k_s, K_i)}{(k_s - 1)!} \right] \quad (7)$$

$$< \sum_{k_s = \delta + 1}^{\infty} \frac{K_s^{k_s}}{k_s!} e^{-k_s} \triangleq E_T^u$$

The upper bound on the truncation error, E_T^u, can in turn be upper bounded by a direct application of the Chernoff bound (Ref. 3). This yields

$$E_T^u \leqslant e^{-\lambda(\delta+1)} e^{K_s(e^\lambda - 1)} \quad (8)$$

Equation (8) holds for any value of $\lambda \geqslant 0$. This inequality can be made exponentially tight by solving for that value of $\lambda = \lambda_0$ that minimizes the right-hand side of Eq. (8). Differentiating with respect to λ, setting the result equal to zero and solving for λ_0 yields

$$\lambda_0 = \ln \left(\frac{\delta + 1}{K_s} \right) \quad (9)$$

Substituting Eq. (9) into (7) and (8) and letting $(\delta + 1) = \zeta K_s$, $\zeta > 0$, we obtain

$$E_T < E_T^u \leqslant \zeta^{-\zeta K_s} e^{K_s(\zeta - 1)} = \left(\frac{e}{\zeta} \right)^{\zeta K_s} e^{-K_s} \quad (10)$$

This shows that for $\zeta > e$, E_T decreases at least exponentially with increasing K_s. In the computation of PAC_T, we have chosen the value $\zeta = 10$. This implies that for any $K_s \geqslant 1$, $E_T < 8.103 \times 10^{-7}$, and can therefore be neglected when compared to the range of acquisition probabilities under consideration.

References

1. Vilnrotter, V. A., and Gagliardi, R. M., *Optical Communication Systems for Deep-Space Applications*, Publication 80-7, Jet Propulsion Laboratory, Pasadena, Calif., Mar. 15, 1980

2. Gagliardi, R. M., and Karp, S., *Optical Communications*, J. Wiley, New York, 1976.

3. Wozencraft, J. M., and Jacobs, I. M., *Principles of Communications Engineering*, J. Wiley, New York, 1965.
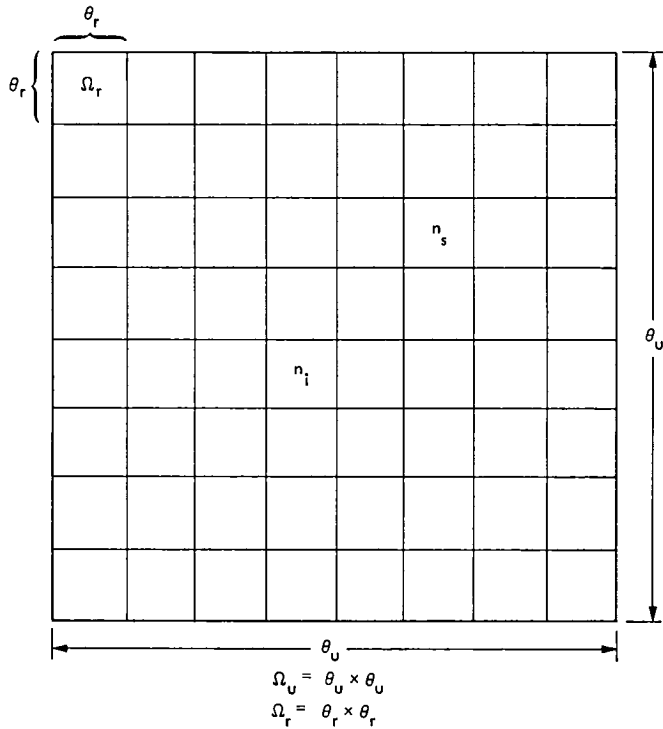
Fig. 1. Spatial resolution matrix

$$\Omega_u = \theta_u \times \theta_u$$
$$\Omega_r = \theta_r \times \theta_r$$

Fig. 2. Acquisition probability as a function of K_s for various K_i

$\alpha = n_i/n_s$

$n_s = 10^3$ PHOTOELECTRONS/SECOND

Fig. 3. Acquisition probability as a function of T for various α

$\gamma = T'/\tau'$
$\beta = T'/\tau$
$T = NT'$
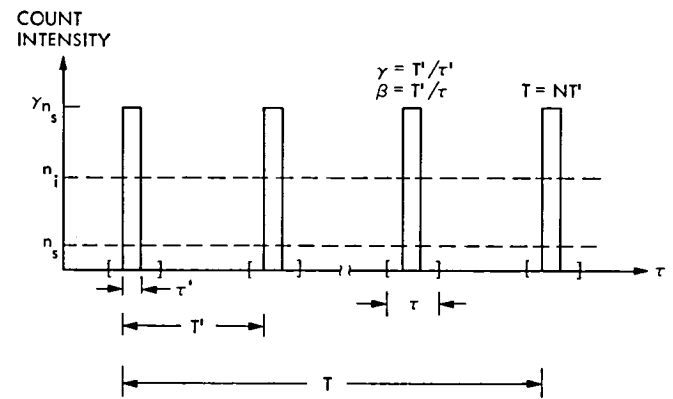
Fig. 4. Temporal distribution of count intensities for a pulsed beacon source
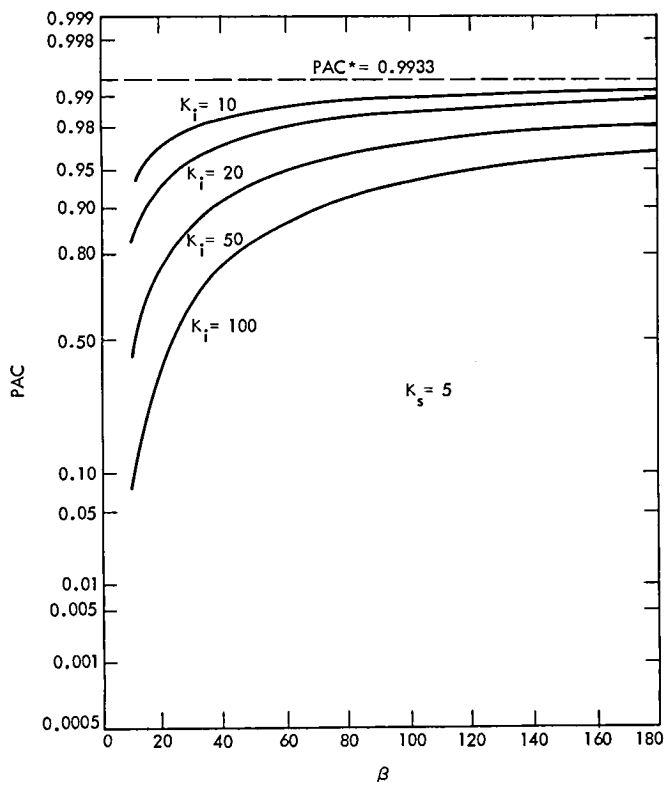
Fig. 5. Acquisition probability as a function of β, $K_s = 5$
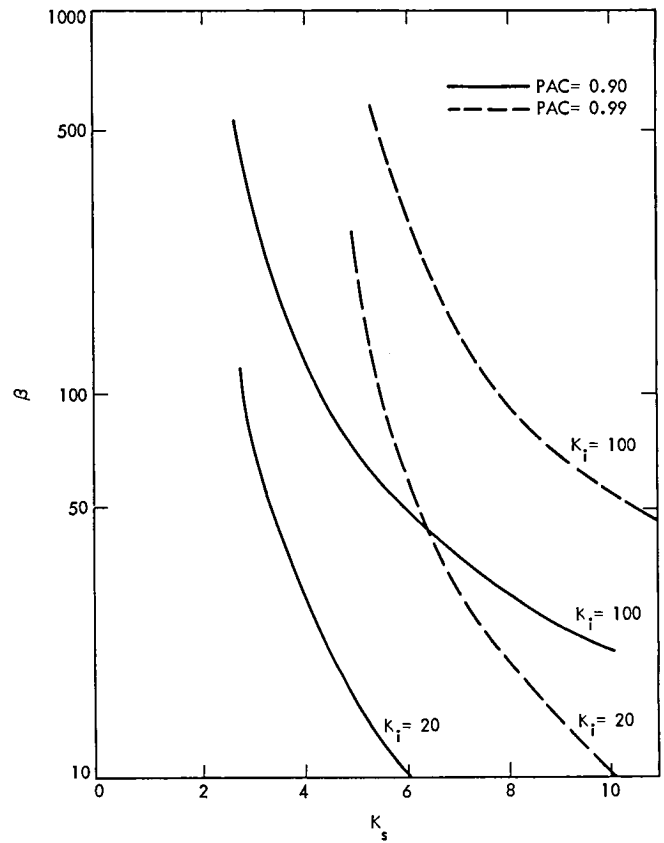
Fig. 6. *PAC* as a function of β and K_s for various K_i

Navigation Network Operational Considerations

E. Hird

Mission Support Operations Division

The development of the philosophy necessary for the initial operations costing of the three candidate NAVNET designs is described. The effect of the need to minimize costs upon the operations and maintenance concepts, the simplification of operations by adopting the VLBI principle as a basis for the operating scenarios, and the estimation of the annual load factor based upon an assumed mission set are detailed.

I. Introduction

The need for accurate deep space navigation has been steadily increasing over the years as the objectives of the flight projects have become more demanding. In recognition of the need for a new form of navigation, the Navigation Network (NAVNET) Project was initiated with the objective of providing an operational navigation system by the mid-1980s. The project was divided into four phases, the first two of which were concerned with the definition of the system. The purpose of Phase A was to examine and evaluate the technologies pertinent to navigation in deep space and it was completed in October 1979. The purpose of Phase B was to explore system concepts that might satisfy future DSN navigation requirements. It began in September 1979 and was due to run through September 1980. However, in February 1980, the Phase B completion date was advanced to 1 May 1980 and the purpose diminished to making a study of three given system configurations. This action was taken to enable an effective interface to be made with the Networks Consolidation Project and to hasten the determination of the need to utilize existing STDN facilities for navigational purposes. The new study task was to develop a preliminary design at the planning level for each of the three given configurations supported by

(1) implementation costs

(2) operations and use costs

(3) an error budget and performance capabilities

(4) operability characteristics and the impact on other network functions

A description of three given configurations is provided in Table 1. In addition, it was required that the study identify all areas where any further development, analysis, or demonstration activity would be needed to satisfy the design requirements. The work described below is concerned principally with the operations and use costs, the operability characteristics, and the impact on other network functions. The narrative represents the thinking that was done, in the limited time available, to develop operational concerns to the point where costs could be credibly estimated for each one of the preliminary designs.

The Planning Configuration, as its name implies, served as a useful vehicle for the incubation and development of ideas from the inception of the NAVNET Project. It was mandated from the beginning of the Project that the principle of Life Cycle Costing would be applied to any system that may be based ultimately on this configuration (or any other). It was intended that the implemented system would be automated for remote control and therefore would need to be highly reliable in operation. The corollary was that operation and maintenance costs would be thus minimized and this idea became a major design constraint. Although this corollary was considered to be a necessary constraint on Configurations 2 and 3 also, it was not thought to be sufficient. It was felt that because the existing DSN might be modified to accommodate other needs in addition to those of the navigation requirements, then any NAVNET design should be consistent (a) with the 1985-era consolidated network, and (b) in system operations.

II. General Operational and Maintenance Concepts

A. Configuration-1 Stations

There were several possible ways in which the general constraint of minimizing operations and maintenance costs could be realized in the preliminary design of the three terminals (stations). The intuitive but unchallenged choice, however, was to limit the options to the one where the terminal equipment could be operated in the unattended mode; that is, with no operator on duty at any of the three site locations. This implied that the essential operator functions would have to be performed remotely. JPL was chosen as the concentration point for the three terminal controls because it was also the location of both the DSN Operations and Communications Centers. The further implication was that no navigation data recording or buffering activities that required operator assistance could be supported at an unattended terminal. Hence, navigation data acquired at any terminal would have to be formatted and transmitted in real time for processing at a central correlator that could be conveniently colocated with the terminal controls. Also, Block II VLBI recording equipment used for radio source calibration purposes would have to be suitably modified to avoid the need for operator attendance. A possible alternative would be to use on-site maintenance personnel to make the necessary tape changes on those few days each year when that activity would be necessary.

The Goldstone anchor station, being a standard DSN station, would be constrained by existing policies in regard to operations costs. Since the anchor station NAVNET activities would not include the acquisition of telemetry data, the implication was that no increase in operations manpower would be needed.

From the very beginning of the NAVNET Project, it was felt that a good guideline for such a dedicated network would be "if we don't get the data today then we will try again tomorrow." This idea loomed large in the selection of a system operational availability factor of 0.95 as a basis for the estimation of the equipment failure rate. It was further understood from the system designer that the "best" angle measurement would be obtained if all three of the terminals were to be operating concurrently. To simplify the calculations, the system was considered to be composed of just the three terminals, each one including eight subsystems, all of them operating simultaneously. The correlator and the connecting data links were assumed to be failure free. On this basis, the subsystem availability factor turned out to be 0.998.

Remembering that a basic constraint was to minimize maintenance personnel costs, the maintenance effort was based upon a staff on-site presence limited to an 8.5 hours per day on 5 days per week. The average response time to an equipment failure was then calculated to be 14.9 hours. Also assuming a mean time to repair (MTTR: the mean time to restore a failed subsystem to a serviceable condition once the repair work had begun) of 1 hour, the subsystem's mean time between failures (MTBF) was estimated to be around 7400 hours. The system designer considered that a subsystem failure rate of one per year would be an acceptable design goal for all of the subsystems excepting the hydrogen maser. Experience with hydrogen masers in the field to date had indicated that these frequency standards were not yet truly operational devices. It was considered that product improvement over the next five years would make station operations possible using redundant hydrogen masers to achieve the necessary level of availability.

From an operations viewpoint, the high estimated value of the subsystem MTBF at the remote terminals implied that:

(1) The corrective maintenance activities to be performed by the local staff would be minimal. Extensive training of the staff in fault location and repair of the complex equipment could not be justified, because the skills acquired would seldom be used and would atrophy through insufficient exercise. Restoral of service following an equipment failure should therefore be supported by the provision of built-in test equipment (BITE) to enable semiskilled personnel to locate and identify the problem to the unit replacement level.

(2) It would not be cost effective to provide local facilities with test and ancillary equipment to permit local repairs to be made to failed replaceable units. So replaceable unit repair should be performed elsewhere

within the DSN and local repairs should be limited to those areas where removal and replacement would be impractical, e.g., structures, cables, and connectors.

Here one may begin to see the dimensions of a design for testability (Ref. 1) problem, a problem for which there was no time to investigate. The analysis had led to where a field test using BITE should be made to determine which equipment item should have to be replaced to restore system serviceability within an average period of one hour. A bench test would be made at a later time to determine which part(s) would have to be replaced within the specific equipment item, the repair turnaround time of which would have to be specified. The bench test might or might not be performed using Automatic Test Equipment (ATE). It would depend upon the result of the tradeoff that would have to be made between the field- and bench-test approaches to achieve the minimum life-cycle cost for sustaining the system availability. An important practical concern would be to ensure that the functional partitioning of the equipment for testing purposes resulted in replaceable electronic equipment items that could be handled by one person and replaceable mechanical equipment items that could be handled by at most two persons, perhaps aided by simple lifting apparatus.

The implied skill limitations of the maintenance staff and the limited test equipment capabilities on site, further implied that limitations should be imposed upon the scope of equipment modifications to be made at the terminals subsequent to the initial implementation. Minor modifications should not require more than two semiskilled persons to complete the installation and checkout in an 8-hour shift. This would mean that modifications would have to be supplied complete, configured, and ready to connect. Major modifications would have to be installed by a special team with necessary equipment sent for the purpose and supported by the local staff.

A special effort would be required in the antenna design to minimize the effect of failure upon system operability. DSN experience indicated that several years might pass before a failure occurred in the antenna mechanical subsystem. However, the subsequent downtime was of the order of days rather than hours. The implication was that the antenna equipment status monitoring should be more automated and that visual inspection capability should be improved to reduce the risk of operational failure.

The cost of equipment maintenance at the Goldstone anchor station would be minimized by utilizing the services already provided at the Complex. Since the station would continue to be a standard DSN station, modifications should be handled in the same way as for other similar DSN stations.

B. Configurations 2 and 3

In these two configurations, the stations would be either existing or upgraded DSN stations within the Consolidated Network, with features depending upon the particular configuration. This implies that there would continue to be a station operator presence. The availability of a station operator would mean that the modifications to the station equipment to do the new navigation activities would require only evolutionary changes to existing operational procedures in contrast to new procedures for the unattended operations required for Configuration 1.

Operator presence would permit local recording of data and so provide relief from the relative inflexibility of the system operational coordination that would be required in Configuration 1, to provide up to three concurrent extra wide-band (~1-MHz) streams of real-time data from different geographical locations to the NOCC. Furthermore, by playing back the recorded data in nonreal time at a lower rate than that at which it was recorded, the reduced data link bandwidth requirement would reduce communications costs.

The operators would be trained to do station-level troubleshooting and to effect a service restoral by replacing a failed unit. This capability would reduce the average maintenance response time from 14.9 hours for Configuration 1 to zero, which in turn would considerably reduce the subsystem MTBF needed to achieve a particular operational availability factor. The reduced equipment-reliability requirement would result in lowered implementation costs.

The Hawaiian terminal, relegated to the role of being a backup for either Goldstone or Canberra in both Configurations 2 and 3, would no longer be considered a candidate for being remotely controlled on the grounds of both cost of implementation and in consistency of operation. The implication was that the terminal should be designed for local operation in a manner similar to that of the standard DSN locations.

It should be further noted that operator attendance, while reducing the average response time to a failure quite dramatically when compared with Configuration 1, would have no effect upon the availability of a hydrogen maser. Hence, redundant hydrogen masers would be needed at each NAVNET location.

In Configuration 3, the addition of an X-band transmitter at each location would create a new risk factor due to the lack of operational experience with the equipment. This risk translated into a need for a human equipment monitor to be on duty at least during each transmitter startup and shutdown

period, until an appropriate level of confidence as to its operational integrity could be established.

The maintenance philosophy for Configurations 2 and 3 had to be approached somewhat differently to that for Configuration 1. It was not the design intent to develop an entirely new station configuration, but rather to make small but significant modifications to an existing DSN station configuration at the subsystem and assembly levels. This implied that any changes in maintenance philosophy would necessarily be small and evolutionary (Ref. 2). It has already been noted that an operator would be available for first line troubleshooting. However, the station operator would be getting direction by voice from the Operations Chief on those occasions when a failure involved loss of data production at the central correlator.

The philosophy of providing modification kits for NAVNET equipment would clearly have to be consistent with that for supporting existing DSN equipment in the Consolidated Network.

The Hawaiian station in both of these configurations was conceived as being built of existing or projected DSN equipment and its maintenance and operation would be based on those existing or projected policies for current DSN Stations.

C. JPL

1. NOCC. From the earliest days of the DSN it was an essential function of the NOCC (or its predecessor) to ensure that the stations had the necessary prior information to make them self-sufficient in conducting specific operations in case communications with JPL were interrupted during the real-time event. The stations were designed to process acquired signals, record the data as a precaution against communication failure, and also transmit that data in real time to JPL where it could be monitored to determine the adequacy of the performance of the single station data acquisition system. The NOCC controller would inform the station operators of any data discrepancy occurrence as observed on a Real-Time Monitor (RTM), and would provide them with system troubleshooting direction to help them discharge the local responsibility for effecting system recovery.

The introduction of the VLBI data type into the DSN for spacecraft navigation would create an important change in the operational philosophy of the NOCC for all three of the configurations to be considered. With VLBI, a multistation data type, a signal would be acquired at two or more geographically separated stations and transmitted over as many different data links to the correlator at JPL. The correlator, a multisignal processor, would produce the observable data.

Hence, the signal processing function would be removed from the stations and relocated at the NOCC. Should observable data fail to be produced when expected, the NOCC personnel would have a more intimate involvement in achieving system recovery for this data type than for any other. NOCC personnel would be responsible for the operation of the data-producing correlator and would therefore be cast as active participants in the total data production process. The NOCC would be an active component in a distributed data production system that could be debugged only by working logically from the observable data generation point towards each signal source. The Operations Chief would have to play a significant role in system troubleshooting. To assist him, it would be necessary to provide voice-communication lines that traversed routes different than the wide-band data links to the stations. This would reduce the probability of concurrent voice and data failure, and so help to improve the system availability. The dimensions of control would include pass continue/abort decisions based upon the presence or absence of correlator "fringe" data, the direction of system level troubleshooting and network rescheduling subsequent to system recovery from a failure. The colocation of the NAVNET operations terminal controls and the NOCC required by Configuration 1 would have implications for further changes in NOCC functional design. The additional control dimensions would include schedule generation, predicts generation, and choice of configuration. It would make a lot of sense to include both the monitor and control functions within the NOCC environmental focus. "Monitor" provides the human stimulus to take action, and "Control" provides the means for implementing a response, so closing a natural loop. The existing DSN hybrid arrangement within the NOCC, whereby system control responses based upon monitor stimuli are exercised for the NOCC Controller vicariously by the station operator could lead to nonoptimal behavioral situations for both of these persons.

2. GCF. A clear need has been established in the foregoing narrative for simplex data links and full duplex voice links by a different route, between each of the NAVNET stations and JPL for all the configurations to be considered. It was assumed that although additional equipment would need to be installed within the GCF, no additional staff would be needed to operate it.

III. Station Operational Scenarios

In the process of conceptualizing the operational scenarios, two constraints upon the system characterization had to be considered. The first of these was that the operational calibration of the implemented system had to be accomplished by techniques and equipment being developed under the DSN VLBI System. The second was that all high-accuracy radio

navigation instrumentation had to use X-band as the primary measurement frequency, with S-band for calibration support or low- to medium-accuracy measurement service. The first of these constraints proved to be a highly significant factor in optimizing the operational scenarios, while the latter retained its latency for future performance upgrades.

A number of different fundamental radio metric data types had been described in the NAVNET Phase A Report (Ref. 3). These were studied and the system designer selected two different VLBI data types for making angle and angle-rate measurements in all three of the configurations to be developed and evaluated. The data types chosen were differenced one-way range (DOR) to satisfy medium accuracy angle measurement needs, and quasar-spacecraft differenced VLBI (ΔVLBI) to meet the higher accuracy needs. These choices gave congruity to the operational activities necessary for making both the spacecraft navigation angle measurements and the system calibrations needed to validate them. Expressed from the operator viewpoint, a change in the level of measurement accuracy for a particular spacecraft would not require any change in the operating technique, but could involve a change in the frequency with which the measurement was being made and also a change in the frequency of performing system calibrations. This uniformity of operation would manifest itself in limiting the need for versatility in operating skills and therefore the amount of effort needed to train operators; also in productivity because the uninterrupted familiarity of operation would eliminate the procedural errors induced by changes in task.

Ranging and range-rate data would be obtained in all three configurations in the conventional two-way mode, with X-band being used in Configuration 3. The ranging and VLBI activities, if scheduled concurrently, would place demands on spacecraft transmitting power that could not be met simultaneously; therefore, an operational constraint would be imposed requiring that these activities be scheduled on an exclusive-OR basis. Both the medium- and high-accuracy range and range rate requirements could be met by the existing DSN S-band capability.

A natural constraint upon the time available for angle measurement activities in all three configurations would be the need to calibrate the system regularly. The system or "platform" would be calibrated by acquiring wideband VLBI data from selected extragalactic radio sources (ERS) to determine station clock rate and clock offset, station location, earth rotation rate, and polar motion. In addition, at less-frequent intervals, these same radio sources would be studied themselves to reevaluate their source characteristics to determine their continued usefulness in system calibration activities.

IV. Network Operations

A. General

The NAVNET stations would have to be provided with a one-way signal emanating from the spacecraft to make angle measurements on it. The spacecraft would have to be in the proper mode and have a reasonably stable oscillator. A wideband RF signal containing several discrete frequencies would be propagated and would be suitable for taking either DOR or ΔVLBI data at the stations. Several of the downlink frequencies would be used in resolving the ambiguity problem to produce the direct angle measurement, while one of the frequencies would be utilized in producing a concurrent angle-rate measurement.

B. Configuration 1

All Configuration 1 station operations are summarized in Table 2. There would be two possible ways of using the stations operationally. The preferred arrangement producing the most useful data from a processing viewpoint would be to schedule all three terminals to acquire either VLBI angle measurement or calibration data concurrently. An alternative arrangement would be to schedule two stations to provide east-west baseline data followed by the most westerly of the pair scheduled with the third station to provide north-south baseline data. Passes not exceeding 30 minutes in duration for each of the two- or three-station arrangements would suffice to meet the medium-accuracy and some lower high-accuracy angle measurements by acquiring DOR-type data. The highest high-accuracy angle measurement requirements would be obtained by acquiring ΔVLBI data during passes not exceeding 60 minutes in duration.

No pre- or postpass ground equipment calibration would be necessary for any of the station VLBI activities.

Range and range-rate data would be needed to support the data acquired during each angle measurement pass and would be provided primarily by the Goldstone anchor station. For the first arrangement, ranging data would be taken either before or after the three-station angle measurement pass period, which would result in the acquisition of less than optimal, low-angle doppler data. The "best" range rate data would be acquired in the second arrangement, between the end of the two-station east-west baseline angle measurement pass and the beginning of the two-station north-south baseline pass. The spacecraft would be at an optimal high angle, approaching the Goldstone meridian crossing, but still not yet in the best position for the north-south baseline pass to begin.

A typical ranging pass would require round-trip light time (RTLT) plus 45 minutes to complete. However, Saturn and

Neptune RTLTs could cause difficulties. Two remedies would be available. Firstly, backup stations at any of the complexes could be used. Secondly, a station could start a ranging signal towards the distant spacecraft, go to another activity, and then come back to the original spacecraft in time to receive the return of the ranging signal. Alternatively, a second station in common view could receive the returning signal. This second method would provide ranging values that are well within the limit of accuracy required in the future, based upon present station timing limitations.

C. Configurations 2 and 3

Station operations for Configurations 2 and 3 are summarized in Table 3. Each complex in Configuration 2 would have a station with existing 1980-era capabilities for the acquisition of angle/angle rate, platform parameters, and ERS calibration data. In Configuration 3, these stations would be additionally provided with X-band ranging and two-way doppler capability to increase the accuracy of these measurements and to provide backup to the prime station at Goldstone.

In both configurations, the Hawaiian terminal would be perceived as a backup for either Goldstone or Canberra. In Configuration 2, it would have an S/X-band listen-only capability as in Configuration 1, but in Configuration 3 it would be provided with the same capabilities as a NAVNET station at a DSN Complex.

In both configurations, angle measurements, platform and ERS calibration would be made by scheduling stations in east-west and north-south pairs because of DSN geographical constraints. The Goldstone NAVNET station would be regarded as prime for ranging and range-rate data acquisition. The range/range-rate schedule for the Goldstone anchor station would be organized on the same basis as for the second tracking arrangement of Configuration 1. The problems associated with very long RTLTs would also be mitigated by using the solutions previously described.

It should be noted that in all three configurations doppler data would continue to be available from the telemetry data acquisition passes made by other DSN stations and would be regarded as "bonus" data.

D. Correlator

The correlator would be remotely operated by NOCC staff. It would be loaded with the tracking schedule to enable an incoming signal to be identified. Typically, the sample signal would arrive on a wide-band data link and the ancillary data, for example antenna pointing angles, would be input from a high-speed line. Configuration 1 stations would provide real-time signals to the correlator, whereas Configuration 2 and 3

stations would record the navigation signal, buffer it, and transmit to the correlator in nonreal time. However, at intervals during each pass, a second or two of near-real time signal would be transmitted from each station via the high-speed data line to be integrated by the correlator to establish the presence or absence of "fringe" data. The hardware correlator design is tolerant of short-term signal interruptions caused by communications line "bumps," for example, and should not therefore be a significant source of pass rescheduling or signal replay. RTM alarms would alert NOCC staff to system problems. Should a data loss be observed at the correlator output, it would be a reasonable practice for the Operations Chief to abandon the remainder of any angle measurement pass, which would be characteristically of short duration, and use the time to assist in returning the system to an operable condition.

V. Network Loading Requirements

The Network loading requirement that was used to estimate the NAVNET station utilization was an assumed one and is shown in Table 4. Only deep-space missions were included in it. A total of seven active spacecraft were distributed such that five would be in a cruise mode throughout the strawman year under consideration, one would be in transition from a cruise mode to an extended planetary flyby mode, and a seventh would be in a planetary orbiter mode for six months of the year. This arrangement created a mix of medium- and high-accuracy angle measurement workload for the conceptual NAVNET.

It was determined that the medium-accuracy requirement for any of the assumed spacecraft would be satisfied by three passes per week, for both angle measurements and for ranging. An angle measurement pass under these conditions would take about 30 minutes to complete, assuming that the VLBI technique would be operational. The time needed for the associated ranging pass would be about RTLT plus 45 minutes. A flyby spacecraft near planetary encounter would require angle measurements to be made at the lower high-accuracy level. Daily angle and ranging passes of 30 minutes and RTLT plus 45 minutes duration, respectively, would suffice. A spacecraft in a planetary orbit mode would require angle measurements to be made at the higher high-accuracy level for which daily angle and ranging passes of 60 minutes and RTLT plus 45 minutes duration respectively would be necessary.

For the NAVNET to remain operationally available, it would be necessary to make regular calibrations of the system. The required calibration workload is included in Table 4 and would depend upon the level of accuracy required in making angle measurements on scheduled spacecraft. Whenever a high-accuracy measurement might have to be made, one

4-hour platform calibration pass per day per station pair would be needed or per station triplet if Configuration 1 were to be used. However, if long periods occurred when all the active spacecraft were in a cruise mode, for example, the resulting overall medium accuracy workload would require just one 4-hour platform calibration pass per station pair or trio per week. ERS characteristics calibrations would have to be made by the NAVNET at approximately 90-day intervals for all those sources that might be used during angle measurement or platform calibration activities. This task could not be done exclusively by a station pair, or trio, during the one- or two-day period needed. It would be scheduled at a time when the angle measurement workload could be minimized with Project concurrence.

VI. Station Workload

The most significant component in the utilization of a NAVNET station proved to be the communications workload. The simple calculations for a station angle measurement workload based upon the assumed mission set are shown in Fig. 1.

It was assumed that five spacecraft were in cruise mode, each one requiring three 30-minute (1/2 hour) passes per week for 52 weeks of the year, resulting in a total of 390 station hours. The flyby and planetary orbiter spacecraft each need the sum of two similar calculations to allow for the medium- and high-accuracy components of their flight profile. These show that the flyby would require 98 station hours and the planetary orbiter 221.

The platform calibration workload on the station was calculated on a worst-case basis. It was assumed that the planetary orbiter and planetary flyby high-accuracy periods of 26 weeks and 10 weeks, respectively, would not overlap. So daily platform measurements would be needed for 36 weeks of the year, and weekly ones for the remaining 16 weeks. The simple calculation based on these needs gave a total of 1072 hours. The radio source characteristics calibrations were assumed to take 24 hours, uninterrupted by the need to make spacecraft angle measurements, four times a year. This activity required a total of 96 station hours.

The total station hours needed to make angle measurements on the seven spacecraft and to make the supporting system calibrations was 1877 for an annual load factor of 1877/8760 = 0.21.

The development of the communications workload for each station is also shown in Fig. 1. The system designer had made a tradeoff between antenna aperture size and the bit acquisition rate to limit the latter to 1 Mbit/s. Signal would be acquired for the duration of an angle measurement pass, but for only half the duration of a platform or source characteristics calibration pass, since it was assumed that the antenna would spend half of the time slewing between radio sources. It was also assumed that radio source characteristics data would be recorded and subsequently mailed to JPL for processing, thereby avoiding the need for communication link transmission time.

In Configuration 1, the 1 Mbit/s communication link would be required for a period equal to the sum of the station angle tracking and platform calibration periods since all signal acquired would have to be transmitted to JPL in real time. This annual link time would be 1781 hours. In Configurations 2 and 3 it was assumed that the acquired signal for both angle measurement and platform calibration would be recorded at the rate of 1 Mbit/s and played back at 230 kbit/s for nonreal time transmission to JPL. Then the annual 230-kbit/s link time would be the sum of the station angle measurement hours plus one half of the platform calibration hours, all extended by the recording rate divided by the playback rate. This would require a total of 5400 hours, an annual load factor of 0.62.

VII. Remarks

The operational philosophy developed in the preceding narrative formed the basis for the M&O Life Cycle Cost development. These costs were defined in two principle categories, communications and personnel. Of the two, communications costs significantly exceeded the personnel costs in all three of the configurations that were studied. However, the communications costs proved to be the softest ones in the whole study for two reasons. Firstly, it turned out to be very difficult to obtain dependable costs in 1980 dollars for a hypothetical use of international satellite data links five years downstream. Secondly, the assumption that international satellite data link costs will remain high in comparison to similar domestic services, will act as a strong driver for advances in communications techniques aimed at dispensing with the need for the continuous full-time connection as is presently indicated.

Other important factors also emerged from the study and are summarized below.

(1) In Configuration 1, the terminals would be operated in an unattended mode from JPL and the system would be subjected to the relative operational inflexibility of a signal having to be returned to JPL in real time. In addition, the Operations organization has had no real experience with remote operations so there would be much to learn about them.

(2) In all the configurations studied, the station operating technique was invariant since the angle measurements and the system calibrations all depended on the VLBI principle. This parsimony of operating technique would offer significant opportunities to narrow down operator skill requirements thus reducing training costs, and for increased productivity because operating errors should be minimized and the range of operating procedures would be reduced.

(3) All configurations required redundant hydrogen masers based upon existing and projected state of the art. This is because a hydrogen maser takes weeks, even months, to recover from a failure, and so would leave the system useless without a backup. The operational problems associated with these devices have yet to be solved.

(4) The role of the NOCC would need to be upgraded to one of system control and monitoring from the present one of station direction and monitoring. VLBI activity would introduce a data type whereby data would be produced at an NOCC-located correlator from signals acquired at, and transmitted to it, from at least two geographically separated stations. Therefore, recovery from system failure would have to begin at the NOCC where the data would be generated. Further system control functions would be conferred on the NOCC if Configuration 1 were to be implemented because the remote operator controls would be colocated with it.

(5) The study has shown that it would be necessary to provide different physical routings between each NAVNET station and the NOCC for the simplex extra-wide-band data link and the full duplex voice link. Failure to do so would foil the system level troubleshooting activity that would be necessary in the event of a data loss at the correlator in the NOCC.

References

1. Writer, Philip L., *Design for Testability*, Code 4050, Naval Electronics Laboratory Center, San Diego, CA 92152.

2. Weinburg, Gerald M., *An Introduction to General Systems Thinking*, John Wiley and Sons, 1975.

3. Document 980-112, *Navigation Network Study, Phase A Study Report*, Jet Propulsion Laboratory, Pasadena, Calif. (JPL internal document.)

Table 1. Configuration description[a]

Configuration 1	Configuration 2	Configuration 3

Planning configuration
Hawaii, Washington State, and
Florida Stations
  25-m antenna
  S/X receive only
  Controlled and operated remotely
  Maintained locally
Goldstone anchor station
  Standard existing capability
	Existing DSN stations
	  S-band up, S- and X-band down
	  Two-way doppler and ranging
	  Wideband VLBI, ΔVLBI
	Hawaii[b]
	  S/X Receive Only
		Existing DSN stations
		  S-band and X-band up (not simultaneously)
		  S-band and X-band down (simultaneously)
		  Two-way ranging (conventional at S-band, wide-band at X-band)
		  Two-way doppler at S- and X-band
		  Wideband VLBI, ΔVLBI
		Hawaii[b]
		  Two-way S/X-band doppler/range

[a]The following features are common to all entries in the table:
  X-band, for highest accuracy
  S-band, for low, medium accuracy and system calibration
  Calibration: wideband VLBI
  Signal processing and correlation at JPL
[b]Backup for North-South Baseline.

Table 2. Configuration 1 station operations[a]

Arrangement No.	Terminal and station usage	Medium-accuracy activity (data type)	High-accuracy activity (data type)	External calibration activity (data type)
1	Florida/Washington State/Hawaii	Angle/angle rate (differenced one-way range)	Angle/angle rate (quasar-spacecraft differenced VLBI)	Platform calibration (wideband VLBI) radio source calibration wideband VLBI)
	Goldstone[b]	Range/range rate (S-band ranging/ doppler)	Range/range rate (S-band ranging/ doppler)	N/A[c]
2	Florida/Washington State Washington State/Hawaii	Angle/angle rate (differenced one-way range)	Angle/angle rate (quasar-spacecraft differenced VLBI)	Platform calibration (wideband VLBI) radio source calibration (wideband VLBI)
	Goldstone[b]	Range/range rate (S-band ranging/ doppler)	Range/range rate (S-band ranging/ doppler)	N/A

[a]Tracking-arrangements, -accuracy, -calibration; data types and terminal usage.

[b]Ranging is not performed concurrently with angle tracking.

[c]N/A = not applicable.

Table 3. Configurations 2 and 3 station operations[a]

Station usage[b]	Medium-accuracy activity (data type)	High-accuracy activity (data type)	External calibration activity (data type)
Madrid/Goldstone	Angle/angle rate (differenced one-way range)	Angle/angle rate (quasar-spacecraft differenced VLBI)	Platform calibration (wideband VLBI)
Goldstone/Canberra			Radio source calibration (wideband VLBI)
Goldstone[c] (Config 2)	Range/range rate (S-band ranging/doppler)	Range/range rate (S-band ranging/doppler)	N/A[d]
Goldstone[c] (Config 3)	Range/range rate (S- or X-band ranging/doppler)	Range/range rate (S- or X-band Ranging/doppler	N/A

[a]Tracking-arrangements (only one arrangement is possible due to DSN geography) -accuracy, -calibration; data types and terminal usage.

[b]Hawaiian station is standby for Goldstone or Canberra.

[c]Ranging is not performed concurrently with angle tracking.

[d]N/A = not applicable.

Table 4. Network loading requirements

	Assumed tracking workload									
	Medium-accuracy workload					High-accuracy workload				
Spacecraft (mode)	Weeks/ year	Angle data		Range data		Weeks/ year	Angle data		Range data	
		Passes/ week	Duration, min.	Passes/ week	Duration, min.		Passes/ week	Duration, min.	Passes/ week	Duration, min.
5 (cruise)	52	3	30	3	RTLT + 45	–	–	–	–	–
1 (flyby)	42	3	30	3	RTLT + 45	10	7	30	7	RTLT + 45
1 (orbiter)	26	3	30	3	RTLT + 45	26	7	60	7	RTLT + 45

Required calibration workload

1. Platform calibration: one 4-h pass/week/station pair if high accuracy not needed
   one 4-h pass/day/station pair if high accuracy needed

2. Source calibration: one 1-day pass/quarter/station pair with minimized tracking load

```
ANGLE-TRACKING WORKLOAD

5 (CRUISE) X 3 X 1/2 X 52                                    =    390

[1 (FLYBY) X 3 X 1/2 X 42] + [1 X 7 X 1/2 X 10]             =     98

[1 (ORBITER) X 3 X 1/2 X 26] + [1 X 7 X 1 X 26]            =    221
                                                                709 h
PLATFORM CALIBRATION WORKLOAD

(7 X 4 X 36) + (1 X 4 X 16)                                 =   1072 h

SOURCE CALIBRATION WORKLOAD

ASSUME THAT THERE IS NO INTERFERENCE WITH ANGLE
TRACKING AND PLATFORM CALIBRATIONS

24 X 4                                                     =     96 h
                                                               1877 h TOTAL
COMMUNICATIONS WORKLOAD

     CONFIGURATION 1

          ASSUME ANGLE IS ACQUIRED AT 1 Mbit/s AND RETURNED IN REAL TIME

          ASSUME PLATFORM CALIBRATION DATA IS ACQUIRED AT 1 Mbit/s
          FOR HALF THE VIEW PERIOD AND IS RETURNED IN REAL TIME

          ASSUME RADIO SOURCE DATA IS RECORDED AND MAILED FOR DATA
          PROCESSING

          THEN 1 Mbit/s COMM TIME = 709 + 1072 = 1781 h TOTAL

     CONFIGURATIONS 2 AND 3

          ASSUME ANGLE DATA IS ACQUIRED AT 1 Mbit/s RECORDED AND
          PLAYED BACK IN NRT AT 230 kbit/s

          ASSUME PLATFORM CALIBRATION DATA IS ACQUIRED AT 1 Mbit/s FOR HALF
          THE VIEW PERIOD, RECORDED AND PLAYED BACK IN NRT AT 230 kbit/s

          ASSUME RADIO SOURCE CALIBRATION DATA IS RECORDED AND
          MAILED FOR DATA PROCESSING

          THEN 230 kbit/s COMM TIME = (709 + 1072 X 1/2) X 1000/230 = 5400 h TOTAL
```

Fig. 1. Angle-tracking station workload

Ground Communication Facility and Network Operations Control Center Reconfiguration

D. S. Bremner and C-K Hung

DSN Data Systems Section

This report addresses the progress in hardware and software changes required for the Network Operations Control Center (NOCC) and the Ground Communications Facility's (GCF's) Central Communications Terminal (CCT) at JPL.

I. Summary

The reconfiguration of the computer facilities in the Central Communications Terminal (CCT) is progressing on schedule. The development configuration was completed in April and the planned summer installations and moves are underway. The new computer programs are being tested in the operational environment. Changeover to the new system is planned for April 1981.

As previously reported (Ref. 1), the Ground Communication Facility and Network Operations Control Center (GCF-NOCC) reconfiguration consists of a set of interrelated hardware and software changes in the Central Communications Terminal (CCT). When completed, this reconfiguration will require fewer computers, fewer programs and will provide an improved operational capability. It will also reduce operator workload and provide the base for a two-operator CCT.

New software programs are required for the Error Correction and Switching (ECS) Assembly and the Data Records Generation (DRG) Assembly. Revised programs are needed for the Central Communications Monitor (CCM) and the Network Communications Equipment (NCE). The computers themselves require additional memory and peripherals. Several switches are being implemented to permit flexible use of the magnetic tape units and full interconnection to the external high speed and wideband data communications circuits.

II. Hardware Status

Two additional MODCOMP minicomputers have been temporarily installed in the CCT and connected to the GCF and Mission Control and Computing Center (MCCC). These computers are being used for the development and test of the ECS and DRG programs and will be used for MCCC interface testing. These new computers are also connected to the backup CCM and NCE computers, permitting subsystem testing to be done in a realistic environment.

The rearrangement of the CCT floor plan commenced in early June and will continue through early August. During this summer period the equipment layout will be substantially changed to accommodate efficient operations and centralized control. The new CCT monitor and control console will then be installed with the switching capability needed to monitor either the old or new arrangements. A new 3-channel wideband capability will be installed and used during the fall for

MCCC and other interface testing. Additional computer peripherals will be installed at this time also.

III. Software Status

As of mid-June, all computer programs were nearing completion and were starting subsystem-level testing. During these tests the programs process operational data (from tape or in parallel with the regular computers) and intercommunicate in their normal fashion. All major functions have been validated, including gap detection, automatic recall and data merging to form IDR's.

Combined subsystems testing will continue through mid-September, followed by acceptance test completion in early October and transfer to DSN Operations on 1 November 1980. November and December are allocated to operations for operator training purposes. Final MCCC tests occur in January, followed by Project testing in February and March. The cut-over to the new system is planned for April 1981.

Reference

1. McClure, J. P., "GCF-NOCC Reconfiguration," in *The Deep Space Network Progress Report 42-55*, pp. 86-89, Jet Propulsion Laboratory, Pasadena, California, Feb. 1980.

Power Line Anomalies as They Affect the Operation of a DSN Station — Overview

T. L. Potter

Goldstone Operations Section

The problem of providing a sufficiently stable and reliable power source for the equipment in a DSN station appears to be getting more serious. The potential for the occurrence of damaging commercial power variations is increasing, while the need for a more precise power source seems to be greater. Local generation of electrical power helps the situation but is made difficult due to increasing fuel costs and decreasing availability of fuel. Frequently, user-created voltage distortions are blamed on the supplier of the power. Increased study and understanding of the underlying factors are needed.

I. Introduction

Within each station of the Deep Space Network (DSN) is a substantial array of data collection and processing equipment ranging from precision timing sources to minicomputers and digital recorders. Each station is powered with highly reliable engine-driven diesel generators. The Goldstone Complex also has a source of commercial power which is used for all but the critical periods of mission support. The electrical energy being drawn from the power circuits within a DSN station has long been considered a fundamental and never changing resource. Variations in this power were frequently considered as non-existent or extremely rare. During those periods when the highest order of quality and reliability was needed it was simply a matter of scheduling the stations to be powered by generators and at that time a "best" situation would exist.

The designers and operators of the early DSN power systems took great pride in the fact that their equipment seldom failed or was unavailable. Indeed the first DSN stations enjoyed a very high order of reliability on locally generated power. Even the first exposure to commercially generated electricity was relatively free of problems. However, recent years have brought about a changing situation which appears to indicate the following trends:

(1) The overall reliability of commercial power is decreasing, raising the specter of complete outages at unknown times for unknown lengths of times. The highest probability of these outages will occur during the summer months when the chances of system overload due to air conditioning, etc., are the greatest.

(2) The current generation of DSN station equipments seems to display an increased sensitivity to power line anomalies. Digital computers with low-level digital logic are prime targets of power line "spikes."

(3) The generation of power line noise within the stations is increasing. Switching power supplies and electric servo drives are suspect, as are the starting and stopping of large electric motors.

(6) *Waveform Distortions.* Changes in the normal shape of the power line waveforms that do not affect the average voltage amplitude and are independent of frequency variations, sags, surges, and transients.

II. Power Anomalies and Definitions

It is felt that certain types of problems being experienced within the DSN are created by relatively obscure and heretofore unrealized factors. Computer halts that occur at the stations many times are associated with power disturbances. Also transmitter "kickoffs" have been traced to sags in line voltage. The following set of definitions is descriptive of the types of anomalies experienced:

(1) *Sags and Surges.* Rapid changes in the amplitude of the ac line voltage, persisting for a fraction of a second, and frequently caused by the application or removal of large electrical loads from the system.

(2) *Transient Impulses.* Deviations from the ideal ac voltage with a very short duration compared with the length of one cycle. The initial impulse may either increase or decrease the instantaneous amplitude of the voltage waveform. Lightning is a primary cause of these disturbances; certain types of machinery also generate impulses of this nature.

(3) *Long-Term Voltage Fluctuations.* Slow variations in the voltage level, measured over a substantial time period (usually 10 seconds or more). Brownouts are an example of this type of disturbance. Both overvoltage and undervoltage conditions are to be guarded against and represent real hazards to equipment in a DSN station.

(4) *Line Interruption.* Cases where the line voltage drops to zero. This is generally considered to be an absence of line voltage for a period ranging from seconds to minutes or even longer. It should be understood that dropouts as short as one cycle (16 msec) are common on even the best commercial power sources. Most of these interruptions are caused by switching at the powerhouse or automatic fault clearing on the high-voltage transmission lines.

(5) *Frequency Variations.* Normally considered as a change in frequency of the power line waveform and averaged over hundreds if not thousands of cycles. Rapid variations of this parameter are not expected due to the high intertia of the rotating machinery used to generate the power. Massive application or removal of electrical load from a system would cause a change in this parameter.

III. Measurements and Observations

At the Goldstone Stations of the Deep Space Network a variety of measurements, observations and recordings are employed to help insure the presence and continuance of a uniform and stable primary power source. The type of equipment being powered at a Deep Space Station falls generally into the following broad catagories:

(1) Low noise radio frequency amplifying and detection systems.

(2) Ultrastable frequency and timing sources.

(3) Microwave data transmission and reception equipment.

(4) Minicomputers, floppy and fixed discs, tape drives and data transmission modems.

(5) Voice communications.

(6) Motor driven hydraulic pumps (10 to 200 hp).

(7) DX refrigeration (1 to 75 ton).

(8) Resistance heating (1 to 50 kW).

(9) Incandescent and flourescent lighting.

Most, if not all, of the above-mentioned equipments are required during the day-to-day operation of a station. A power outage or instability in the voltage would be a matter of concern and could easily result in a direct loss of primary data from one or more of the various NASA spacecraft operating in deep space. At the Goldstone stations the power parameters are monitored and recorded as per Tables 1 and 2. Table 3 presents a preliminary result of the data collected during the past 12 months with regard to actual loss of information from the stations. In addition, it should be noted that the anomalies tabulated are only those which actually impacted station performance.

IV. Conclusion

It can be seen that the trend is toward an increase in station interruptions due to commercial power anomalies. Whether these anomalies are becoming more frequent or greater in magnitude is yet to be determined. Also, an increase in station equipment sensitivity would explain, at least in part, the effects

111

being seen. A continued collection of data is planned. This data will help to answer the following questions:

(1) Is the absolute number of commercial power anomalies increasing?

(2) Are these anomalies becoming more severe as time goes on?

(3) Are certain pieces of equipment within a DSS more susceptible to power anomalies?

(4) To what extent are self-generated problems clouding the data?

(5) Could special measures be taken within the station to minimize these effects?

As the need becomes confirmed, appropriate engineering recommendations will be made and further reports will be made with the latest findings.

Bibliography

Clarkson, G. A., "Protecting Electronic Gear from Unexpected Energy Surges," *Telephony*, March 5, 1979.

Dranetz, A. I., and Dietmann, M., "Tracking Down and Identifying Power Line Aberrations," Dranetz Engineering Laboratories, Inc., 2385 S. Clinton Ave., South Plainfield, N.J.

Fuhrman, D., "Incoming Inspection for AC Power," Dranetz Engineering Laboratories, Inc., 2385 S. Clinton Ave., South Plainfield, N.J.

Fuhrman, D., "Power Monitoring — It Can Help Cure Your Repair/Replacement Problems," Dranetz Engineering Laboratories Inc., 2385 S. Clinton Ave., South Plainfield, N.J.

Fuhrman, D., and Fix, E., "Input-Output Disturbance Analysis — A New Technique for Power-Supply Performance Evaluation," Dranetz Engineering Laboratories Inc., 2385 S. Clinton Ave., South Plainfield, N.J.

General Electric Company, *Electric Utility Systems and Practices*, chapters 1, 2, and 13.

General Electric Company, *Transient Voltage Suppression Manual*, second edition.

Table 1. Goldstone power monitoring capability

	DSS 11		DSS 12		DSS 14	
	G-1	G-3	G-24	G-26	G-80	G-81
Strip chart recordings						
Voltage, V		X	X			X
Current, A		X	X			X
Power, W		X	X			X
Power, factor, %		X	X			X
Frequency		X	X			X
Panel indicators						
Voltage, V		X	X			X
Current, A		X	X			X
Power, W		X	X			X
Power factor, %		X	X			X
Frequency		X	X			X
Power analysis						
Average voltage	X		X[a]	X	X	
Sags	X		X[a]	X	X	
Surges	X		X[a]	X	X	
Impulses	X		X[a]	X	X	
Frequency	X		X[a]	X	X	

[a]Continuous monitoring and analysis of commercial power provided.

Table 2. Building location key

Pioneer Station generator bldg. G-3

Pioneer Station control bldg. G-1

Echo Station generator bldg. G-24

Echo Station control bldg.. . . . . .G-26

Mars Station generator bldg.. . . . . .G-81

Mars Station control bldg. G-80

Table 3. Data interruptions due to commercial power anomalies

1979/80	DSS 11	DSS 12	DSS 14
May	–	1	1
Jun	1	–	1
Jul	1	1	2
Aug	3	1	3
Sep	1	–	1
Oct	–	1	2
Nov	1	1	1
Dec	1	1	1
Jan	–	1	–
Feb	6	4	5
Mar	3	4	1
Apr	2	2	NA

NA: not applicable; station down for modifications.

Voyager-Jupiter Radio Science Data Papers

G. S. Levy

TDA Technology Development

G. E. Wood

Tracking Systems and Applications Section

The reduction and interpretation of the radio science data from the Voyager 1 and 2 encounters of the planet Jupiter and its satellites has resulted in the preparation of several papers for publication in the special Voyager-Jupiter issue of the Journal of Geophysical Research. *The radio science and tracking systems of the Deep Space Network provide the data which makes this research possible. This article lists submitted papers by title, with their authors and with abstracts of their contents.*

The Atmosphere of Jupiter: An Analysis of the Voyager Radio Occultation Measurements

G. F. Lindal, G. E. Wood, G. S. Levy, J. D. Anderson, D. N. Sweetnam, H. B. Holtz, B. J. Buckles, D. P. Holmes, P. E. Doms, Jet Propulsion Laboratory. V. R. Eshleman, G. L. Tyler, Stanford University. T. A. Croft, SRI International.

Coherently related S- (2.3 GHz) and X-band (8.4 GHz) signals transmitted from Voyagers 1 and 2 have been used to probe the Jovian atmosphere during occultations of the spacecraft by Jupiter. The observations have yielded profiles in height of the gas refractivity, molecular number density, pressure, temperature, and microwave absorption in the troposphere and stratosphere of Jupiter at altitudes ranging from 0° to about 70° south. The data cover a pressure range from 1000 to 1 mbar over a height interval of 160 km. At the

100 mbar level, the temperature was 165 ± 7 K and the temperature lapse rate was equal to the adiabatic lapse rate. The ammonia vapor abundance in this region of the atmosphere was about 0.015%, in approximate agreement with the value derived from cosmic abundance considerations. The tropopause, which was detected near the 140 mbar level, had a temperature of 100 K. Above the tropopause, the temperature increased with increasing altitude, reaching 160 ± 20 K in the 10 to 1 mbar region of the stratosphere. Significant horizontal density variations were detected in the stratosphere, which may imply a non-uniform temperature and aerosol distribution across the Jovian disk. The zenoid or gravity equipotential surface which best fits the 100 mbar isobaric surface has an equatorial radius of 71,541 ± 4 km and a polar radius of 66,896 ± 4 km. The data in this report was obtained from the narrowband open loop recordings (5 and 15 KHz at S- and X-band, respectively). A programmed local oscillator was used to keep the spacecraft signals within the chosen bandwidth.

Dispersive Doppler Measurement of the Electron Content of the Torus of Io

G. S. Levy, D. W. Green, H. N. Royden, G. E. Wood, Jet Propulsion Laboratory. G. L. Tyler, Center for Radar Astronomy, Stanford University.

As Voyager 1 made its swing-by of Io, it passed through the satellite's plasma torus. The phase of the coherent 13-cm and 3.6-cm wavelength signals transmitted from the spacecraft was accelerated by the propagation medium, which resulted in the observation of a dispersive doppler signature at the NASA/Jet Propulsion Laboratory Deep Space Network stations.

Ray path integration through three different models of the electron distribution of the torus of Io (Warwick, et al. (1979), Birmingham, et al. (1980), and Bagenal, et al. (1980)) have been performed. The results of the integrations are compared to the dispersive doppler data.

Radio Occultation of Jupiter's Ring: Bounds on Optical Depth and Particle Size

G. L. Tyler, E. A. Marouf, Stanford University. G. E. Wood, Jet Propulsion Laboratory.

The Jovian ring is not detectable in the radio occultation data, setting the bounds on its optical thickness of 2×10^{-4} and 5×10^{-4} at 13 and 3.6 cm wavelengths, respectively. Comparison of the results at the radio, infrared, and optical wavelengths suggests a population density that either falls more rapidly than the inverse square of the linear size or is sharply bounded in maximum particle size. A fragmentation power law of power index between -3 and -4 leads to a minimum size estimate of 1-2 μm.

A Search for the Radio Occultation Flash at Jupiter

J. M. Martin, G. L. Tyler, V. R. Eshleman, Stanford University. G. E. Wood, G. F. Lindal, Jet Propulsion Laboratory.

The "evolute flash," a focusing effect caused by the curvature of a planet's limb, was sought in the data from the Voyager 1 Jupiter encounter using a modified matched filter technique. The flash signal frequency structure is double-branched, here approximated by two quadratic functions, while the intensity structure is highly peaked in part due to the Voyager 1 geometry. The search for this signal was carried out over a 6.4 s period; the signal parameters were varied to span the uncertainties introduced by errors in the orbit determination and the shape of Jupiter. Several peaks of the order of 8σ above the mean are present in the filter output. However, these peaks were separated in time by up to 3.3 seconds, the multiplicity of which indicates the signal was not detected. A lower bound on the absorption along a ray with periapsis near 4.3 bar is 24 dB. Employing a locally isothermal atmospheric model, it is estimated that the flash will be visible if the distance behind the planet where the spacecraft trajectory crosses the evolute is approximately 20 Jupiter radii at a ray periapsis pressure of between 1 and 2 bar.

The signal search was made through the use of open loop pre-detection recordings of the spacecraft signal recorded by the Deep Space Network.

End of Document